Ph.D. dissertation

Spreading of macromolecules at the air/water interface

Andrea Tummino

Academic supervisor: Dr. Imre Varga

ILL supervisor: Dr. Richard A. Campbell

Institut Laue-Langevin
Large Scale Structure Group
FIGARO

Eötvös Loránd Unviversity
HNL laboratoires
Institute of Chemistry

CHEMISTRY DOCTORATE SCHOOL

Head of Doctoral School: Prof. Dr. György Inzelt

ANALYTICAL CHEMISTRY, COLLOID-AND ENVIRONMENTAL CHEMISTRY, ELECTROCHEMISTRY PROGRAM

Program Leader: Prof. Dr. Gyula Záray

Budapest, 2018

Table of Contents

Overview

The goal of this Ph.D. thesis is to provide insight into the delivery of macromolecules at the air/water interface by exploiting non-equilibrium effects. Such interactions occur both in the bulk of the solution, as well as at its interface with air. It is demonstrated that macromolecular films at the air/water interface exhibit a marked non-equilibrium nature, which can be exploited to form highly stable films with an enhanced surface excess, beyond the monolayer coverage, in a process referred to as surface loading. For this purpose, a systematic investigation of the sample history, by comparing films formed with different methodologies, i.e. by spreading or by adsorption from bulk solutions, has been carried out. First, the state of the art literature about the bulk and surface properties of oppositely-charged polyelectrolyte/surfactant (P/S) mixtures as well as on the non-equilibrium aspects of protein spread films are described (chapter 1). This is followed by the description of the materials, the experimental protocols for sample preparation and characterization techniques (chapter 2). The next part of the thesis is dedicated to the experimental results and their discussion (chapter 3). Lastly, the conclusions and future outlooks of this project are given in the final chapter (chapter 4).

In an introductory experimental part of the thesis (chapter 3.1), the discussion is focused on the mechanism of formation, the stability, the morphology and durability of films of defatted human serum albumin (DF-HSA) spread from droplets of concentrated aqueous solutions, following their contact with the interface of a standard phosphate buffer (SPB) solution. The surface properties of these films are compared to those of adsorbed layers from the bulk of pre-diluted protein solutions with equivalent final bulk concentrations, revealing the non-equilibrium nature of spread films of protein. The investigation was carried out by means of ellipsometry, neutron reflectometry (NR), Brewster angle microscopy (BAM) and surface tensiometry. It is shown that the dominant contribution to the surface loading mechanism is the Marangoni spreading of protein from the bulk of the droplets rather than the direct transfer of material from their surface films. The films can be spread on a dilute subphase if the concentration of the spreading solution is sufficiently high; otherwise, dissolution of the protein occurs, and only a textured adsorbed layer slowly forms. The morphology of the spread protein films comprises an extended network with regions of less textured material or gaps. Furthermore, mechanical cycling of the surface area of the spread films anneals the network into a more stable morphology that approaches constant compressibility and has higher durability.

In the main part of the thesis, the possibility of forming surface loaded films from self-assembled aggregates composed of oppositely-charged polyelectrolytes and surfactants, by exploiting the same Marangoni flow mechanism, is demonstrated and thoroughly characterized. In this case, the polyelectrolyte itself is not surface active; it is the prior formation of liquid crystalline aggregates in P/S mixtures that allows their exploitation in the formation of spread films. The fast dissociation of the aggregates upon contact with pure water in combination with the high entropic gain due to the counter-ion release upon the binding of surfactant molecules to the polyelectrolyte chains and the following dilution of the same counter-ions, after spreading into a much larger volume of subphase (mixing entropy), allow one to attain trapped films in which more than one-third of the total polyelectrolyte has been confined to the interface. The main part of the investigation is focused on P/S mixtures composed of poly(sodium styrene sulfonate)/dodecyltrimethylammonium bromide (NaPSS/DTAB), at a fixed bulk polyelectrolyte concentration (100 ppm) while varying the bulk surfactant concentration (from 0.43 to 25 mM) to generate aggregates with different charge/structure in the spreading aliquots. In a first experiment, films spread from neutral NaPSS/DTAB aggregate dispersions are the focus (chapter 3.2), as previous studies indicated that uncharged aggregates may be good candidates for the preparation of spread, surface loaded P/S films. The characterization of the spread films was carried out using ellipsometry both under static and dynamic conditions, while NR was used *in situ* during compression/expansion cycles of the interface in surface pressure vs. area experiments. The films are shown to be stable over time and impervious to mechanical perturbations during consecutive compression/expansion cycles of the interface.

This work was then extended to an investigation of the effects of the charge/structure of P/S aggregates (chapter 3.3) on the surface loading mechanism as well as on the properties of P/S spread films at the air/water interface. A thorough investigation of the effects of the sample history on the film properties and stoichiometry has also been carried out. It is demonstrated that the presence of compact and highly charged aggregates embedded in the monolayer triggers the formation of extended structures, either by consecutive additions of P/S mixtures onto an aqueous subphase or by compressing the interface, allowing the surface coverage to exceed that of a monolayer, as was confirmed by the surface excess derived from NR data analysis. The visualization of the extended structures in the real space was attained by BAM, which showed that the morphologies of the extended structures are different in the spread and the compressed cases. These structures ultimately act as reservoirs of surface active material.

Such structures were previously observed for concentrated P/S mixtures, i.e. at the surface of P/S mixtures with similar concentrations to that of the spread aliquots, but this was the first time that the formation of these reservoirs has been observed for very dilute systems. Moreover, it is the first time that their formation and morphology have been controlled by varying the nature of the components at the interface and by handling the samples differently. An analogy of the controlled formation of extended structures in fluid monolayers is made to the reservoir dynamics in lung surfactant (albeit noting the important differences between the systems), and it is discussed how this link could open up the possibility of controlling such film dynamics in related systems through the rational design of self-assembled particles in the future. All of the films made from aggregates over the whole range of P/S compositions investigated exhibit a one-to-one surface stoichiometry and this observation supports a theoretical assumption made two decades ago that was not experimentally confirmed, until now.

This work was then extended to an investigation of NaPSS/DTAB films spread on a subphase with elevated ionic strength (chapter 3.4). It is also shown that the bulk ionic strength is a crucial parameter to tune the equilibrium vs. non-equilibrium nature of P/S films, as well as their stoichiometry, and to control the formation of the extended structures, thus affecting the mechanical properties of the interface. In particular, it has been observed that the addition of an inert salt, like NaCl, promotes the thermodynamic equilibrium between the bulk and the surface of P/S spread films, and suppresses the non-equilibrium characteristics already investigated.

In the final part of the results and discussion chapter (chapter 3.5), preliminary investigations on the effects of the molecular architecture of the polyelectrolyte backbone, as well as its charge density, on the physical properties of the resulting spread films are discussed. For this purpose, the results on NaPSS/DTAB spread films are compared with two other systems: poly(diallyldimethylammonium chloride)/sodium dodecyl sulfate (Pdadmac/SDS) and poly(ethyleneimine)/SDS (PEI/SDS). Pdadmac is a strong linear polyelectrolyte, like NaPSS, while PEI is a hyperbranched polyelectrolyte whose charge density is pH-dependent (i.e. highly ionized at low pH, while partially ionized at high pH). The comparison indicates that, at low ionic strength, spread films from P/S aggregate dispersions are generally not in equilibrium with the bulk of the system. However, it was also observed that the surface mechanical features are strongly influenced by the molecular architecture, while the pH

might also be employed to tune the formation of extended P/S structures at the air/water interface.

In the near future, it is anticipated that this project will evolve in three directions. The first is to see if these new findings can be generalized also to other oppositely-charged macroions/surfactant systems, such as nanoparticle/surfactant mixtures, as both systems are widely used in soft condensed matter and could have applications in different technological fields ranging from sensing to nanomedicine. The second is the extension to biocompatible P/S systems for the rational design of novel pharmaceutical formulations. The bridge of the behavior of spread films in synthetic systems to lung surfactant mimics is the third possible extension of this project.

This work has been carried out in the laboratories of the "*Partnership for Soft Condensed Matter"* (PSCM) at the Institut Laue-Langevin (ILL, Grenoble, France) and in the laboratories of HNL in the Institute of Chemistry, ELTE University (Budapest, Hungary). All NR experiments reported in this thesis have been performed on the "*Fluid Interface Grazing Angle ReflectOmeter"* (FIGARO) at the ILL.

This work has been funded by the Ph.D. studentship program of the ILL.

Chapter 1: Scientific Background

Over the last century, the relation between bulk and surface properties of aqueous solutions of macromolecules has attracted growing attention in colloid science.[1,2] Many previous studies have focused on polyelectrolyte solutions and their mixtures with oppositely-charged surfactants. The increasing interest has many sources of motivation. The first is to develop a clearer understanding of the structure and the formation mechanism of macromolecular layers at fluid interfaces. The second concerns the widespread applications of these materials in everyday products,[3,4] water treatment,[5] biomedical device coating,[6] and biocompatible materials.[7] Moreover, since many biologically-relevant macromolecules are either polyelectrolytes (e.g., proteins, nucleic acids…) or surfactants (e.g., lipids), there is scope to extend the knowledge of the behavior of synthetic P/S systems to fields including the delivery of functional molecules (e.g., DNA,[8] protein/peptides[9] and drugs[10]) and even the fabrication of organic photovoltaic devices.[11] In addition, a better understanding of the properties of P/S mixtures could lead to industrial applications with reduced environmental impact and better cost-effectiveness.

In the following paragraphs, a brief overview of polyelectrolytes, proteins and surfactants in solution, as well as their mixtures, is given. Particular attention is paid to the relation between bulk and surface properties of oppositely-charged P/S mixtures, in order to understand the non-equilibrium aspects of these systems and how they determine the resulting physical properties.

1.1 Polyelectrolytes

Polyelectrolytes are macromolecules whose repeating units (or a part of them) carry an ionizable functional group (amine, carboxylate, sulfonic…) or an ionic couple (a salt). Polyelectrolytes dissociate in aqueous solutions to polycations or polyanions, depending on the sign of the charge of the functional group, and their respective counterions. The functional group can either be part of the main chain or be attached to the side chains. Polyelectrolytes are describes as either *strong* or *weak*, depending on their tendency to dissociate to free charges or hydrolyze in aqueous solution. In addition, polyelectrolytes can be either *acids* or *bases*. In this case, their degree of ionization can be pH-dependent.

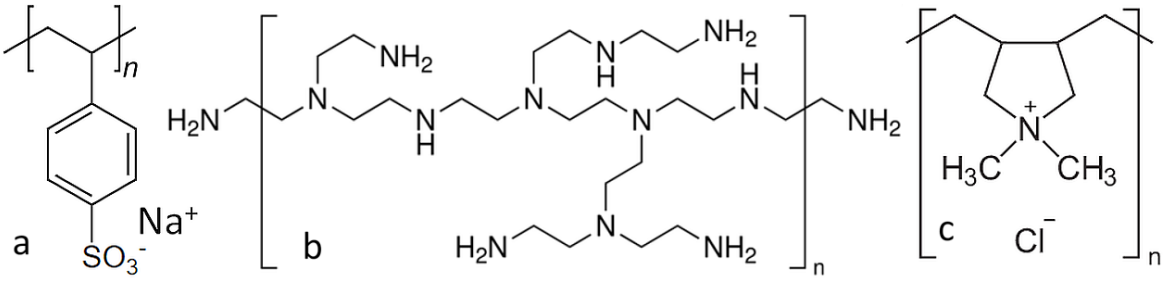

Figure 1 - Structural formula of three synthetic polyelectrolytes: a) poly(sodium styrene sulfonate), NaPSS; b) branched poly(ethyleneimine), PEI; c) Poly(diallyldimethylammonium chloride), Pdadmac.

Another classification can be made according to their origins. *Synthetic* polyelectrolytes are produced via organic synthesis and are not present in nature. *Natural* polyelectrolytes (or biopolyelectrolytes) are produced by nature. Nucleic acids (DNA, RNA) and proteins are biopolyelectrolytes, for instance. *Artificial* polyelectrolytes are produced by chemical modification of natural ones. Three examples of synthetic polyelectrolyte (used in this thesis) are shown in figure 1.

Theoretical and experimental studies on polyelectrolyte solutions date back to the middle of the twentieth century[12-14]. Since then, a lot of attention has been paid to the rheological and dynamic properties of polyelectrolyte solutions in order to understand their structure/property relations, as well as to find a unified theory to explain the behavior of polyelectrolytes and uncharged polymers. Despite these efforts, some aspects of the behavior of polyelectrolyte solutions represent a mystery in colloid science.[15-17] This is in contrast to the more well-established picture for uncharged polymers, for which the Flory-Huggins theory (FH) is in excellent accordance with the experimental data. A difficulty of applying FH theory to polyelectrolyte solutions arises from the fact that in this theory, only the short-range monomer-monomer and monomer-solvent interactions are taken into account. However, in polyelectrolyte solutions, the coulombic forces lead to strong long-range interactions, thus affecting the structure of the macromolecular coil. Over the last fifty years, several models inspired by FH theory, combined with the Kuhn's statistics, have been developed to take into account the electrostatic contribution.[12,16,18-21]

The presence of charges on the polymer chain causes swelling of the polymeric coil. The dimensions of the coil, as well as the properties of polyelectrolyte solutions, depend on several parameters, such as the concentration of chains,[20,23], their molecular weight,[24,25] the degree of ionization[26,27], the chain stiffness,[28] the ionic strength[29] and the valence of the counterions.[30,31]

Polyelectrolytes, in particular polyanions, interact strongly with metal ions and the phase behavior of their solutions is deeply affected by the presence of an added salt, i.e. the ionic strength is a critical variable for controlling the phase behavior. In the absence of added salt and in dilute conditions, the coils are swollen.[18] This is because the distribution and the concentration of counterions are different inside the coils compared to the surrounding medium. In particular, the counterion concentration is larger inside and nearby the coil, i.e. close to the charged segments. This generates a difference in osmotic pressure between the inside of the macromolecules and the solvent, which in turn causes the coil to swell (left side of figure 2).

As the ionic strength is increased, the concentration of counter-ions becomes larger in the bulk solution. This favors the shrinkage of the coil for two reasons: 1) the decreased difference in counterion concentration reduces the osmotic pressure and 2) as the counterion density increases, charge screening becomes more effective and, consequently, the electrostatic repulsion between polyelectrolyte segments decreases (right side of figure 2). When the ionic strength is further increased, the coils collapse and overlap with each other leading to phase separation.

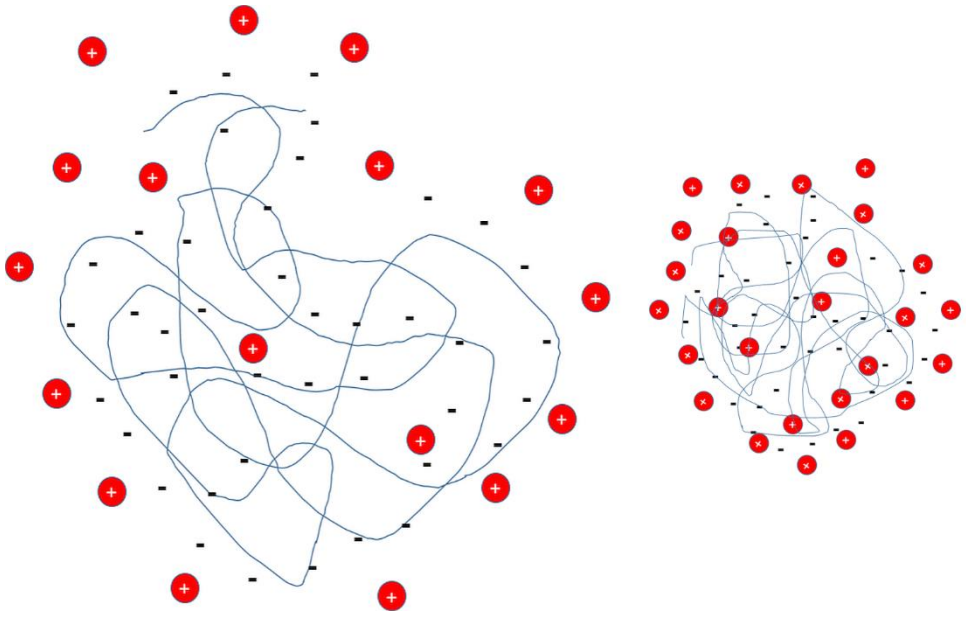

Figure 2 – Schematic representation of a polyelectrolyte coil at low ionic strength (left) and at high ionic strength (right). The polyelectrolyte is sketched in blue, while the counterions are drawn as red circles.

The behavior of polyelectrolytes at fluid interfaces, particularly the air/water and the oil/water interface, has also attracted considerable attention. For a molecule to be both water-soluble and have the ability to adsorb spontaneously at fluid interface, it must have both hydrophilic and hydrophobic parts. In other words, it has to be amphiphilic. This requirement

is satisfied in the case of copolymers[32] in which one of the two monomers is an electrolyte, grafted polyelectrolytes[33], globular proteins[34-36] and nucleic acids[37]. However, this situation is not always the case when dealing with synthetic polyelectrolytes. In fact, the amphiphilic character of a polyelectrolyte depends on its charge density, its degree of ionization, the ratio between charged and uncharged monomers (as for copolyelectrolytes) and the presence of grafted hydrophobic groups. In addition, one has to consider if the hydrophobic and hydrophilic parts of the molecule can separate into two different domains, allowing their spontaneous adsorption at the air/water interface. For macromolecules, due to steric constraints, such separation is not always achieved.[38]

1.2 Spread films of proteins

Proteins are weak polyelectrolytes, whose charge and structure depend on the pH and the ionic strength of their solution. They are composed of alpha-amino acids, which are small organic compounds bearing both a carboxylic and an amine functional group on an alpha-carbon atom, i.e. the two functional groups are linked by a methine group. To some extent, proteins can be seen as natural random copolyelectrolytes. Their structure can be rationalized into three (or four) different levels. The *primary* structure is simply the ordered list of the amino acids that compose the protein. The *secondary* structure refers to the presence of regular and repeated patterns, typically alpha-helices and beta-sheets. The *tertiary* structure is what the protein looks like in the real space. For proteins composed of more than one peptide chain (or for protein complexes), a *fourth order* describes how the subunits are held together.

At the air/water interface, globular proteins have attracted lots of attention over the last fifty years, because they can form stable layers on spreading, in spite of their high solubility in aqueous media. Globular proteins exhibit quite high conformational flexibility, which allows them to rearrange in order to perform a given task. As they are flexible amphiphilic molecules, it means that they can separate their hydrophilic and hydrophobic domains, which results in their surface activity.[39] However, any structural rearrangement can take place only if the secondary and tertiary structures of the protein change, i.e. by denaturation of the protein upon contact with the surface. This process could be caused by the interaction of the protein molecules with the interface itself, as it is a completely different thermodynamic environment to the bulk solution,[40] or by the electrostatic and steric forces acting laterally in the protein layer, or both.[41] For this reason, the formation of protein films at the air/water interface has been described in the context of the stability of the secondary and tertiary structures. Most of the work has been focused on the preparation of protein films from

solutions of globular proteins, either by adsorption from the bulk or by spreading. Particular attention has been given to human serum albumin (HSA), a ubiquitous protein in the human body, and bovine serum albumin (BSA). These two proteins are very similar. BSA and HSA are both globular proteins with a molecular weight of roughly 66 kDa. Their amino acid sequences are different for less than 25%.[41,42] Several authors have reported that these similarities are also reflected on the physical properties of BSA and HSA, both in the bulk and at the interface of their solutions.[43,44] In this thesis, the focus of attention is the defatted form of human serum albumin, whose native structure in aqueous solution is approximately heart-shaped[45].

The possibility of trapping proteins at the air/water interface by exploiting non-equilibrium effects has been known for almost a century. Since then, significant attention has been given to the mechanism of film formation, as well as the film stability in the context of the folding of protein tertiary structure at the air/water interface, which is still a debated topic. [46-50] It has been shown that a substantial decrease in surface tension is achieved when spreading protein films from concentrated droplets[51] or from hydrated crystals[52] upon contact with the air/water interface. Film formation is initiated by Marangoni spreading due to the low surface tension of the hydrated crystals or of the protein solutions used for spreading. This general phenomenon was described by Carlo Marangoni almost 150 years ago. Marangoni spreading occurs spontaneously as a result of a surface tension gradient when a solution of amphiphilic material comes into contact with a liquid subphase. It is a bidimensional, radial flow originating from the contact point between the pending droplets of solutions with different surface tension than the subphase. The direction of the flow depends on the sign of the surface tension gradient. When the spread droplet has lower surface tension than the subphase, material is spread from the droplet to the interface upon contact. The reverse case has also been reported.[53] From a thermodynamic perspective, the equilibrium conditions require the chemical potential of the molecules in the bulk solution and the chemical potential of the molecules at the interface to be equal. For insoluble or poorly soluble materials the bulk is rapidly saturated. This approach is widely used to form self-assembled Langmuir films of lipids.[54-56] These surfactants are usually spread from an organic solvent. The solvent, typically chloroform or dichloroethylene, needs to fulfill two requirements: 1) it must have a surface tension lower than water; 2) it must be a good solvent for the molecular system to spread. It is worth pointing out at this stage that all the experiments described in this thesis

are free of organic solvents, which may have certain advantages in case the technology is scaled up in the future.

Spread protein films can be prepared by contacting small aliquots of protein aqueous solution, drop by drop, with the air/water interface. For relatively soluble molecules, like globular proteins, one may expect that the material in the film would dissolve until the thermodynamic equilibrium is reached. However, kinetically-trapped metastable films can be persistent for long period: equilibration is inaccessible on experimentally accessible time scales, as an activation barrier, resulting from the interactions in the monolayer, prevents dissolution. Moreover, it has been demonstrated that protein films prepared in such a way, have enhanced surface excess with respect to monolayers formed by bulk adsorption from solutions at equivalent final bulk concentration. [57] In addition, these films have been shown to be impervious to subphase dilution[58] and to contain approximately the 70% of the material in the spreading aliquot.[50]

However, a clear picture regarding the mechanism of film formation, as well as quantitative information about film stability and morphology, was still missing. Furthermore, the question of whether proteins undergo denaturation when they are in contact with the air/water interface is still an important topic of debate. Generally, the difference in surface tension observed between spread films and adsorbed layers of protein are interpreted in terms of the microscopic parameters of the proteins, such as the conformations that flexible proteins can adopt[60] or to thermodynamic variables (chemical potential).[61] Less is known about the influence of the sample history on the morphology and the density of protein molecules at the air/water interface. The aim of the preliminary investigation (chapter 3.1) on the properties of spread films and adsorbed layers of DF-HSA is to provide some new insight on this old problem, but from a different perspective. In particular, it will be shown that both the mechanical properties as well as the surface excess of DF-HSA films are dramatically affected by the sample handling, which results in different morphologies of spread protein films compared to those formed by adsorption from bulk solutions with an equivalent final bulk concentration. This investigation was carried out both under static conditions, inside a glass Petri dish, and dynamic conditions, during surface pressure vs. area experiments over five consecutive cycles, by the means of ellipsometry, NR, BAM and surface tensiometry (Wilhelmy method).

1.3 Surfactants

Surfactants are small amphiphilic molecules that reduce the surface tension of water. They are a class of organic compounds whose structure can be rationalized as follows: a polar head group, bonded to one or more hydrophobic carbon chains. The nature of the polar head group can be zwitterionic, ionic or non-ionic. This structure allows them to adsorb spontaneously at the interface between a hydrophobic fluid phase (such as oil or air) and water. It is also thanks to their structure that the detergent properties of surfactants can be explained. Another useful feature of surfactants is their ability to form self-assembled supramolecular aggregates with well-defined internal structure in solution, whose shapes and formation depend on the surfactant concentration. The simplest geometry that the aggregates can adopt is the sphere, micelles for single-chain surfactants and vesicles for double-chained surfactants, in figure 3. Micelle formation occurs at a specific bulk concentration of the surfactant, known as the *critical micelle concentration,* cmc (discussed later). Surfactants find applications in many fields in colloid science. Detailed descriptions of their properties, applications and the fundamentals of surfactant solutions can be found in several textbooks.[62-64.]

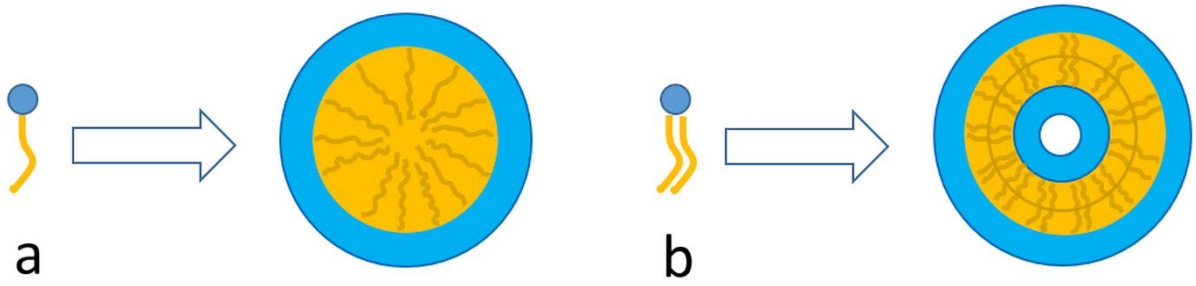

Figure 3 – Schematic representation of single chain surfactants and micelles (a) and double chained surfactants and vesicles (b).

Spherical micelles and vesicles are not the only kinds of self-assembled supramolecular structures that surfactants can form. The formation of micelles with different shapes, their dimensions, and their structures depend on the bulk concentration and the molecular architecture of the surfactants. Transitions from spherical to rod-like micelles, disc-like micelles, or hexagonal and lamellar phases are observed. Some examples of the different supramolecular aggregates are shown in figure 4.

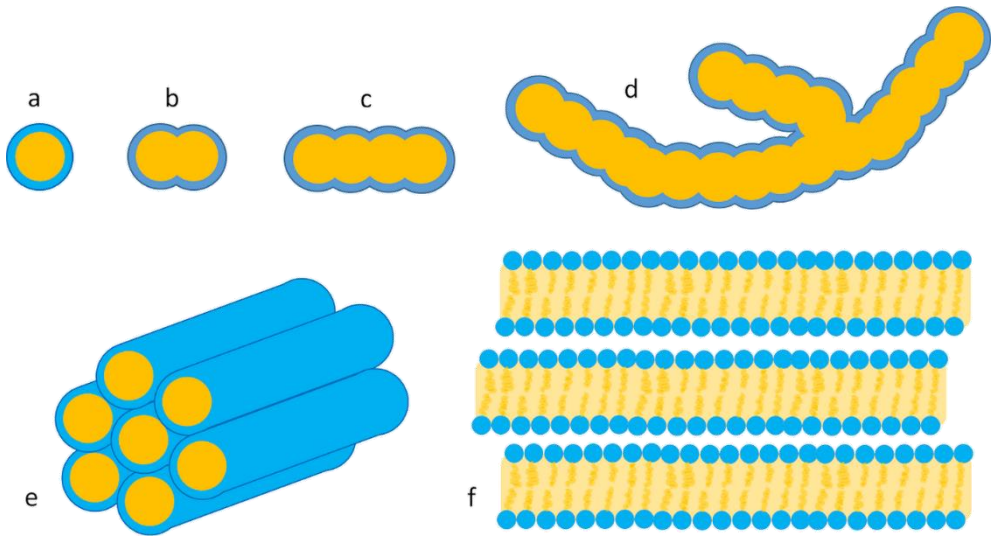

Figure 4 – Transition from spherical micelles (a) to elongated (b) and worm-like (c-d), up to hexagonal (e) lamellar phases (f) in highly concentrated surfactant solutions.

With reference to figure 4, it is important to bear in mind that aggregates of the kinds b to f are formed only at very high concentrations of surfactant. In most cases, for dilute surfactant solutions, individual surfactant molecules and micelles are both present in solution. The mechanism and thermodynamics of micellization have been investigated for almost one century and are currently well-understood, mostly thanks to the pioneering work of Tanford[65,66] and Israelachvili, Mitchel and Ninham.[67] Tanford was the first who described the hydrophobic effect (discussed later). Israelachvili, Mitchel and Ninham introduced the concept of the *molecular packing parameter* (mpp), often also referred to as the *critical packing parameter*, which dictates the shape of the primary formed micelles for a given surfactant. The *mpp* is defined as: the ratio of the volume of the chain over the effective area of the head group multiplied by the chain length ($A_e \times l_0$):

$$mpp = V_0/A_e \times l_0 \qquad (1)$$

where (V_0) is volume of the carbon chain, l_0 is its length, and A_e is the effective area of the head group. It depends on on the repulsion term between head groups (α), and it derives from the theory of Tanford.[65,66] For neutral surfactants (zwitterioninc and non-ionic) α is constant, while it depends on the charge density of the head group, the Debye length and the thickness of the electric double layer for ionic surfactants. According to this variable, one can predict the shape, the aggregation number and consequently also the sizes and the masses of micelles in solution. Typical values of the *mpp* are listed in table 1, together with the corresponding shapes.

Table 1 – typical values of molecular packing parameter for supramolecular surfactant aggregates with different shapes.

Molecular packing parameter	**Shape**
0 < mpp < 1/3	Spherical micelles
1/3 <mpp < 1/2	Rod-like micelles
1/2 <mpp < 1	Bilayer vesicles (lipids)

The bulk and surface properties of surfactant solutions are governed by thermodynamics, where the free surfactant molecules in solution, the micelles and the surfactant molecules at the any interface are in equilibrium. In the bulk, at very low concentrations of surfactant, micelle formation is thermodynamically unfavorable. Because of their structure, the free surfactant molecules are asymmetrically solvated. The hydrophilic heads are hydrated. The tails are surrounded by water molecules, which organize themselves into so-called ice-like structures. The term ice-like does not mean that the water molecules freeze around the hydrophobic tail. In fact, these structures are very dynamic and with a persistence time that is approximately comparable to that of molecular vibrations (a few picoseconds). However, the hydrogen bond network is strongly affected by the presence of a non-polar molecule. In these ice-like structures, water molecules point towards one another in such a way that the number of hydrogen bond network is maximized, which in turn decreases the overall entropy of the system as the degrees of freedom of bulk water molecules are reduced. As the surfactant concentration is increased, the chemical potential is increased: the more crowded environment promotes the contact between hydrophobic chains, thus releasing water molecules from the ice-like structures, and significantly increasing the overall entropy of the whole surfactant solution. This phenomenon is known as the hydrophobic effect, and it represents the driving force for surfactant association in solution and adsorption at interfaces. The increase in surfactant chemical potential continues until the cmc is reached, where micelles form. From this point on, the chemical potential remains almost constant, i.e. the addition of more surfactant molecules does not strongly affect the chemical potential.

Micelle formation involves several equilibria, from dimers up to micelles. If the surfactant molecules are denoted with the letter N and the micelles with M, the following chemical expression can be used to conceptualize them:

$$N + N \leftrightarrows N_2 + N \leftrightarrows N_3 + N \leftrightarrows \cdots \leftrightarrows N_{mic-1} + N \leftrightarrows M \qquad (2)$$

Each one of the above equilibria is described by individual equilibrium constants, K_n with $n = [2; +\infty[$. To a first approximation, it can be assumed that only one of the K_n values is dominant, i.e. only one of the n associative steps is important for micelle formation to occur. This model is known as the closed association model and according to the model, the equilibrium of micelle formation can be treated as:

$$nN \leftrightharpoons M \tag{3}$$

Thus, the equilibrium constant becomes:

$$K = \frac{[M]}{[N]^n} = \frac{C_{mic}}{{C_{free}}^n} \tag{4}$$

Where n is the aggregation number. The total surfactant concentration is:

$$C_{tot} = nC_{mic} + C_{free} \tag{5}$$

It follows that the variation of Gibbs free energy is:

$$\Delta G_{mic} = -RT\ logK = nRT \log C_{free} - RT\ log\ C_{mic}$$

C_{free} increases until the cmc is reached. At the cmc it, remains approximately constant (C_0). The variation of C_{mic} can be written as:

$$\frac{dC_{mic}}{dC_T} = \frac{K^{1/n}}{nK^{1/n} + \frac{1}{n}{C_{mic}}^{(1-n)/n}} \tag{6}$$

Plots of $\frac{dC_{mic}}{dC_T}$ are reported in figure 5 for $K = 1$ and $n = 2, 3, 30, +\infty$, showing that as the aggregation number increases, micelle formation approaches a first-order phase transition.

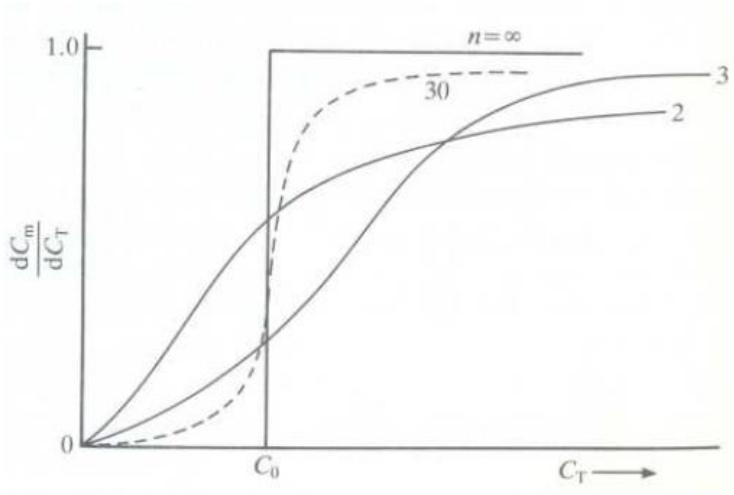

Figure 5 – Derivative of the micelle concentration, C_m, with respect to the total surfactant concentration, C_t, for $n = 2, 3, 30, +\infty$ and K=1. The ideal, but unrealistic, case for n=+∞, looks like a first-order phase transition. Image reproduced from ref. 62.

Although this model is simple, it is physically unreasonable as it does not take into account different micelle shapes and sizes and it cannot explain the variation of aggregation number. In order to solve these issues, a more complicated model, which considers all the equilibria taking place in solution, needs to be employed. Such model is known as the multiple equilibrium model, in which the overall association constant is the infinite product of the *n* equilibria in Eq. 2: $K_{mic} = \prod k_n$.

The hydrophobic effect also explains the reason why surfactant molecules adsorb spontaneously at any interfaces. At the air/water interface, the surfactant molecules keep the polar heads submerged in the aqueous subphase. The release of water molecules from the ice-like structure causes the apolar chain to become exposed to the air where they can interact with each other without perturbing the hydrogen bond network of the water phase. The Gibbs adsorption isotherm can be used to describe both the surface tension (γ) and the surface excess (Γ) of the surfactant molecules at the interface from their bulk chemical potential. For non-ionic surfactant:

$$-d\gamma = \Gamma d\mu \tag{7}$$

where μ is the chemical potential of the surfactant. Though combination of this expression with the definition of bulk chemical potential, equation (7) can be re-written in the form:

$$\Gamma = -\frac{1}{fRT}\frac{\delta\mu}{\delta lnC} \tag{8}$$

where f is the activity coefficient and C is the total bulk surfactant concentration. Thus, if the surfactant concentration is increased, the surface tension will decrease while the surface excess will increase. Plots of the surface tension vs. the total surfactant concentration (figure 6) show that the surface tension decreases as the surfactant bulk chemical potential is increased. This means that a further increase in the surfactant bulk concentration causes more and more molecules to be adsorbed at the interface, until the cmc is reached. At the cmc, the chemical potential of the free surfactant remains almost constant. The addition of extra surfactant causes the micelle to change in size and number, while the surface tension remains approximately constant.

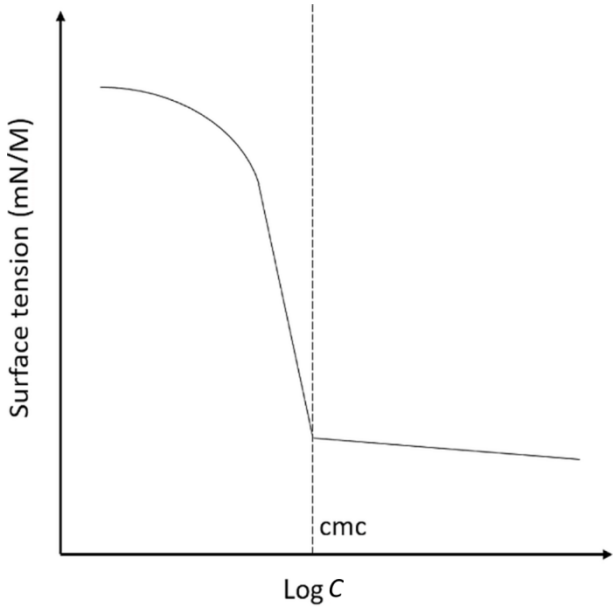

Figure 6 – Variation of the surface tension of water/surfactant systems with respect to the total bulk surfactant concentration. The critical micelle concentration (cmc) is marked by a vertical dashed line.

1.4 Oppositely-charged polyelectrolyte/surfactant (P/S) mixtures

1.4.1 Bulk phase behavior

Investigations of the bulk interactions in oppositely-charged P/S systems, in terms of surfactant binding to the macromolecule backbone, followed on from those of the weakly interacting uncharged polymer/ionic surfactant systems.[68] In the case of uncharged polymer/surfactant mixtures, it has been demonstrated that the binding of surfactant molecules to the polymer chain can be treated as a cooperative process. This means that the binding occurs only after the concentration of surfactant reaches a given threshold. This concentration is known as *critical aggregation concentration* (cac), which is below the cmc,[156,157] and it indicates the onset of surfactant binding.[1,68] After this point, the amount of bound surfactant increases sharply,[69] until the cmc is reached. These polymer/surfactant complexes have a peculiar structure, in which micelle-like surfactant aggregates are wrapped together by individual polymer chains. For this reason, this model structure was referred to as "pearl necklace".[70] The structure of these complexes, as well as the binding itself, depend on the molecular weight of the polymer, as it has been demonstrated by Mészáros and co-workers.[69] For a given concentration of polymer segments, the long chains (high molecular weights) can bridge together several micelle-like surfactant aggregates. Short polymer chains can interact with single micelle-like structures. As the chains get shorter, the binding become less efficient and, consequently, the cac of the system increases. However, if the chains are too short, the binding of surfactant molecules can also not take place and the cac reaches the cmc. For the intermediate molecular weights, when the surfactant concentration is increased, the bound amount reaches a pseudo-plateau, as the chains become saturated. At the cmc, the amount of bound surfactant increases abruptly, as preformed micelles in solution start binding to the polymer chains at this point. Typical shapes of binding isotherms are reported in figure 7 together with a schematic representation of the structure of polymer/surfactant complexes in relation to the molecular weight of the polymer.

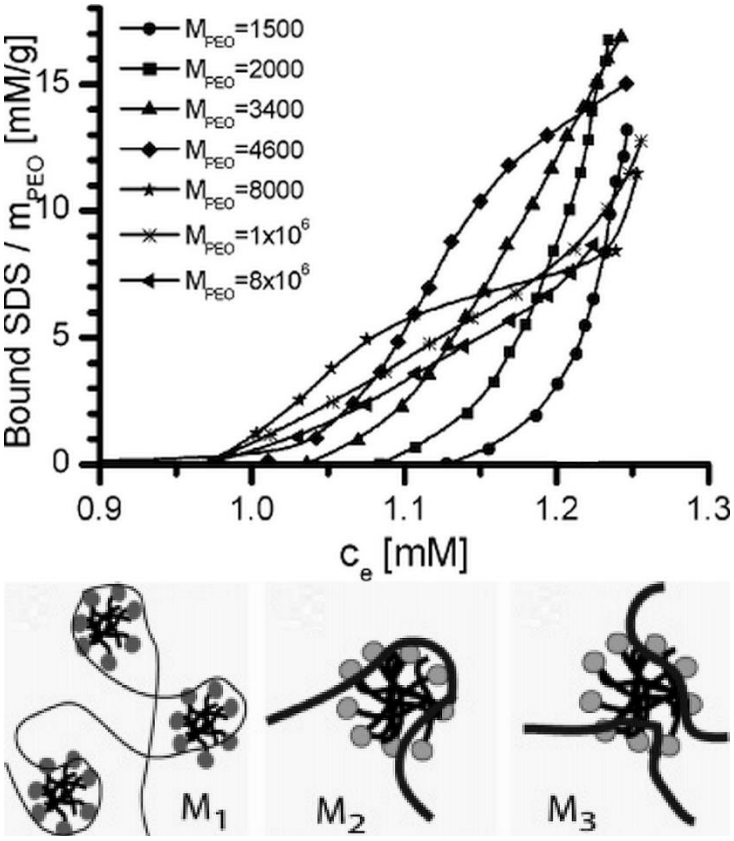

Figure 7 – (top) Plots showing the effects of the polymer molecular weight on the binding isotherms of polymer/surfactant mixtures with respect to the equilibrium concentration of the free surfactant in solution (C_e) in polyethylene oxide/sodium dodecyl sulfate (PEO/SDS) mixtures; (bottom) Schematic representation of the structure of PEO/SDS complexes for different polymer molecular weight $M_1>M_2>M_3$. The images are taken from ref. 69.

The bound amount, B, can be calculated by the following expression:[71,72]

$$B = c - c_{free}/c_{pol} \tag{9}$$

where c is the total bulk concentration of surfactant, c_{free} is the equilibrium free surfactant concentration and c_{pol} is the concentration of the polymer repeat units.

The general physical picture for uncharged polymer/surfactant mixtures described above is still valid also in the case of oppositely-charged P/S mixtures. However, some important differences should be pointed out. The association of an uncharged polymer with an ionic surfactant is driven mostly by weak forces (Van der Waals, London) and by hydrophobic interactions. In the case of oppositely-charged polyelectrolytes and surfactants an additional strong coulombic attraction has to be taken into account. The increased strength of the interaction is reflected on the physical properties of these systems. For instance, the cac values of oppositely-charged P/S mixtures are generally orders of magnitude lower than in the case of uncharged polymer/surfactant mixtures. Moreover, the bulk phase behavior of oppositely-charged P/S mixtures has marked non-equilibrium features and it varies strongly

with the composition. If the concentration of polyelectrolyte is kept constant, at low surfactant concentration the mixtures are equilibrium one-phase systems containing swollen *complexes*, formed by micelle-like supramolecular surfactant aggregates wrapped by single polyelectrolyte chains. These complexes are in equilibrium with the free surfactant molecules in solution. Aggregation of the complexes themselves is prevented since they have high charge density provided by the excess of polyelectrolyte segments. Besides, swollen *aggregates* with high surface charge, provided by the polyelectrolyte excess, can be formed due to concentration gradients present during mixing. These aggregates can persist in solution even for months in a kinetically-trapped state.[22,73,74]

As charge neutrality is approached, the diminishing charge on the complexes reduces the electrostatic repulsion between complexes, which in turn leads to their compaction. The complexes lose colloidal stability and P/S aggregates involving many polyelectrolyte chains are formed.[75,76] Over time, precipitation (sedimentation or creaming) occurs, and the system evolves to an equilibrium two-phase state (associative phase separation).[77,78]

At higher bulk surfactant concentrations, the free surfactant molecules in solution adsorb onto the surface of the compact aggregates, thus providing electrostatic stability and suppressing further aggregation.[73,74,79] In this region, P/S mixtures are electrostatically stabilized non-equilibrium colloid dispersions.

Furthermore, steady state bulk properties can be affected by the sample history, e.g. changing the mixing order or the mixing protocol. To this end, Mészáros *et al.*, have thoroughly characterized the bulk phase behavior of oppositely-charged P/S mixtures composed of hyperbranched PEI and SDS by the means of several instrumental techniques.[79] They have shown that the mixing order has a strong effect on the sizes and the structures of PEI/SDS aggregates. Some differences in the sample were detectable even by the naked eye: a turbid dispersion was obtained when the surfactant solution was added to the polyelectrolyte solution under continuous stirring, while a transparent dispersion was formed in the reverse case. In another study conducted on the same P/S system, Mezei and co-workers investigated the effects of different mixing protocols on the bulk properties of these mixtures.[22] They found that both the coagulation rate as well as the size, and possibly the structure, of both complexes and aggregates, were different from one experimental pathway to another.

Another parameter that has a strong influence on the bulk phase behavior of P/S mixtures is the ionic strength. It has been shown that with increasing ionic strength, the stability of P/S

mixtures can decrease continuously until a critical coagulation concentration is reached.[80] The phase separation region then extends to higher bulk surfactant concentrations as a result of the charge screening of the aggregates.[80,81] In addition, it was shown in work on mixtures of NaPSS and hexadecyltrimethylammonium bromide (CTAB) that associative phase separation is suppressed when the ionic strength is sufficiently high.[81] Therefore, the addition of inert electrolytes to aqueous P/S mixtures can be used effectively to tune the equilibrium versus non-equilibrium nature of these systems.

1.4.2 Surface properties

It has been almost fifty years since Goddard and co-workers compared the surface tension behavior of oppositely-charged P/S mixtures to that of weakly interacting polymer/surfactant mixtures. They found that the addition of a small amount of polyelectrolyte to a dilute surfactant solution caused a substantially larger decrease in the surface tension than for the case of neutral polymers.[82,83] A few years later, the lowering of the surface tension of dilute P/S mixtures was attributed to the synergistic adsorption of neutral P/S layers, in equilibrium with their bulk.[84] From that moment on, a lot of efforts have been put to finding a general description relating the bulk properties and phase behavior of P/S mixtures to their interfacial properties and structures with respect to the polyelectrolyte nature[85-87]. Although it has been well established that the non-equilibrium features of P/S systems play a crucial role with regards to their properties, their interfacial behavior has until recently been treated in terms of equilibrium adsorption of the complexes.[88-90] However, over the last decade, there has been progress made on the influence of non-equilibrium effects at the air/water interface. For example, it has been systematically demonstrated that depletion of material at the interface can occur as a result of slow bulk aggregation,[91] while enhancement can result from the interaction of P/S aggregates at the interface.[92] Indeed, it has been outlined recently how many steady-state interfacial properties reported in the literature in fact must have been far from equilibrium.[93] Furthermore, the addition of an inert electrolyte can be used to convert kinetically-trapped steady states to the equilibrium states.[94] More and more studies are emerging where data interpretations are set in the context of a non-equilibrium physical framework.[95,96] A significant contribution to the field of non-equilibrium phenomena of P/S mixtures has been made by Campbell, Varga and co-workers. In particular, they have demonstrated that the previously accepted classification, indicated by Thomas and Penfold, of P/S systems into type 1 and type 2 according to their surface properties, [90] is redundant. In that classification, type 1 P/S mixtures were reported to exhibit a plateau in the surface

tension isotherm, like NaPSS/DTAB films, [97,98] while type 2 P/S mixtures were characterized by the presence of a surface tension peak in the turbid concentration range, such as for Pdadmac/SDS mixtures.[99,100] However, it has since been shown that these differences in surface tension behavior can be rationalized by slow precipitation in the bulk, and that the original experimental data in the former case could not have been at equilibrium after all, as originally assumed.[93] Indeed, when surface tension measurements are performed on the freshly mixed P/S systems, both types exhibit a plateau in surface tension, and when precipitation has fully occurred the surface tension peak is produced in both types of systems. The same authors also showed that it is possible to predict the surface tension isotherm, i.e. the existence or the absence of a surface tension peak, as well as its magnitude, if one considers the surface of a fully precipitated P/S mixture as a depleted surfactant solution.[101] It is worth underlining that some of the most relevant data recorded in the investigation of the surface properties of P/S mixtures have been made by the means of NR measurements, and the same techniques still plays a major role in this field nowadays.[102-104]

Significant attention has been paid over the years to the mechanism of P/S film formation. The possibility of forming compressible,[105] gel-like[106] and heterogeneous[107] molecular films out of equilibrium has been well established. Films have also been produced by spreading P/S complexes from an organic solvent onto the air/water interface.[108] Recently, work has focused on film formation through the interaction of P/S aggregates from the bulk dispersions to the air/water interface. Two main steps of interfacial layer formation were resolved for refined PEI/SDS aggregates: their adsorption followed by their dissociation and spreading.[109] It was also discovered that on the continually-expanding surface of an overflowing cylinder, the majority of the material at the interface can originate from the dissociation of aggregates and the spreading of material, as opposed to complex adsorption.[110] Furthermore, it was shown that highly charged aggregates of poly(amidoimine) dendrimers and SDS remained embedded intact at the air/water interface, while those with a lower charge were not detected.[111] The interfacial dissociation of P/S aggregates triggered by particle-particle interactions to spread material at the air/water interface has also been reported.[112]

From these studies, it can be inferred that the properties of P/S mixtures at fluid interfaces are determined by the interaction and, in some cases, the dissociation of P/S aggregates. Moreover, the charge/structure of the aggregates may be used to switch on and off the delivery of surface active material by Marangoni spreading.[111]

The relationship between the bulk and surface properties of aqueous P/S mixtures has, however, been established only in moderate concentration regimes. To date, there has been no evidence that non-equilibrium effects persist in P/S mixtures in very dilute conditions and several questions remain open. In particular, since the surface properties are governed by the interaction of pre-formed P/S aggregates in the bulk mixtures, is it possible to exploit the direct interaction of these aggregates with the surface of a pure aqueous subphase to form stable P/S films out-of-equilibrium conditions, both in terms of surface excess and surface mechanical features? Is the interaction dependent on the charge/structure of the aggregates or does it depend on the total amount of material available? Can the nature of P/S spread films be tuned by varying the ionic strength of the subphase?

In order to answer these questions, the main part of this thesis is focused on the mechanism of film formation of trapped P/S films by exploiting the Marangoni spreading and the fast dissociation of aggregates as they contact a pure air/water interface. To demonstrate their non-equilibrium nature, a systematic investigation of the sample history is given by comparing the results of spread films formed from P/S aqueous mixtures, containing aggregates with different charge/structure, to adsorption layers formed by diffusion-driven bulk adsorption of P/S complexes from solutions with equivalent final bulk compositions. The investigation was carried out by the means of ellipsometry, NR, BAM and surface tensiometry, both at the static air/water interface (constant surface area) and under dynamic conditions. It is thanks to this combination of surface sensitive techniques that a depth of information about the trapped nature of P/S spread films is revealed.

Finally, the effects of the polyelectrolyte architecture as well as its charge density are investigated by comparing the results obtained for spread films from NaPSS/DTAB aggregate dispersions to two other systems: hyperbranched PEI/SDS and Pdadmac/SDS mixtures. The former polyelectrolyte not only has a different molecular architecture, compared to the linear backbones of both NaPSS and Pdadmac, but PEI is also a weak poly(base), thus its charge density is pH-dependent. This investigation was also carried out under both static and dynamic conditions.

Chapter 2: Experimental methods

2.1 Materials and methods

2.1.1 Materials

All the polyelectrolytes used in the experiments described in this thesis are hydrogenous. 17-kDa NaPSS (analytical standard; Sigma-Aldrich), 750-kDa hyperbranched PEI solution (50% in water, Sigma-Aldrich), 100–200-kDa Pdadmac (Sigma-Aldrich), D_2O (99.9 % d-atoms; Sigma-Aldrich), NaCl (99.999 %; Fluka Analytical), ethanol (≥ 99.8 %; Honeywell), and chain-deuterated DTAB and SDS (d_{25}-DTAB and d_{25}-SDS; 98.7 % d-atoms; CDN Isotopes) were used as received. Hydrogenous DF-HSA lyophilized powder was purchased from Sigma-Aldrich, stored at -20°C and used as received in 50 mM SPB at pH 7.2. The DF-HSA stock solution was stored below 4°C to minimize protein aggregation. Acetone (> 99.5 %; Fisher Chemicals) was distilled once. Hydrogenous SDS (h-SDS), hydrogenous DTAB (h-DTAB) were purchased from Sigma Aldrich and recrystallized twice, respectively, in ethanol and 4:1 acetone ethanol mixture, followed by drying under vacuum first at room temperature and then at 50°C. Purified H_2O (18.2 Mohm.cm) was generated using a Milli-Q machine.

2.1.2 Sample preparation

DF-HSA films

Two different protocols were used to produce protein films at the air/water interface: adsorbed from pre-diluted DF-HSA solutions and surface loaded onto the air/SPB interface. The first samples were prepared according to a rigorous methodology to remove any trapped material at the interface which will perturb the equilibrium of the sample.[113] The protein was dissolved in SPB, then: (1) liquid was transferred to the trough by pipetting from the bulk of the solution, and (2) the surface of the liquid in the trough was cleaned by aspiration for 3 s.

Surface loaded films were prepared by the drop-wise spreading of aliquots of concentrated (0.1 mg/ml) DF-HSA solution onto a dilute aqueous subphase of SPB. A number of droplets were dispensed from a glass pipette held at an angle of 45°, gently touching the center of the surface and avoiding their falling from a height. Ellipsometry and surface tensiometry measurements were performed in a Langmuir trough made of Teflon (5 cm × 20 cm, Biolin scientific) equipped with moving barriers. Brewster angle microscopy (BAM) measurements were performed in a Petri dish made of glass with 7 cm diameter.

P/S films

Stock solutions of the individual components were made in purified H_2O or ACMW (air contrast matched water; 8.1 % v/v D_2O in purified H_2O; zero scattering length density). 2000-ppm polyelectrolyte stock solutions involved overnight stirring to ensure full dissolution of the powder and they were diluted 10-fold to prepare 200-ppm polyelectrolyte solutions. 50-mM DTAB, cm-DTAB (contrast matched DTAB; 4.4 % v/v d_{25}DTAB in DTAB; zero scattering length density) or d_{25}-DTAB and SDS stock solutions were diluted to the required concentration for a given measurement prior to use. None of the stock solutions contained added NaCl.

P/S mixtures were produced by rapidly mixing of equal volumes (up to 300 μL) of a 200-ppm polyelectrolyte stock solution and a surfactant solution at a bulk concentration of double the final required value, under continuous stirring for three seconds. This method was used to minimize concentration gradients during mixing that enhance the production of kinetically-trapped aggregates.[73,74] Each P/S mixture was used within 1 minute of their preparation in order to limit aggregate growth prior to their use. After, the P/S mixtures were dispensed according to surface loading protocol described for DF-HSA films. For the ellipsometry and BAM experiments at the static air/water interface, 100 μL of P/S mixtures were dispensed onto 25 mL of aqueous subphase contained in a 7-cm diameter Petri dish made of glass. For the stepwise addition experiments, five 100-μL aliquots were dispensed onto 25 mL of pure water at 5-min intervals. For the NR experiments, the spread aliquots were scaled by volume up to 500 μL and dispensed onto 125 mL of subphase in a Langmuir trough (Nima, Coventry, UK; surface area of 283 × 100 mm^2). The BAM experiments at the dynamic air/water interface were performed in a larger Langmuir trough (Nima, Coventry, UK; surface area of 900 × 100 mm^2) and the spreading aliquot was scaled by volume to 1800 μL. The aqueous subphase comprised purified H_2O or 0.1 M NaCl in purified H_2O for the laboratory-based experiments and ACMW or 0.1 M NaCl in ACMW for the NR experiments.

Adsorbed layers were prepared from pre-diluted solutions of the two components prior to their mixing. This approach was used to ensure that the samples remained in the equilibrium one-phase region, i.e. in absence of aggregates, during the whole experiment. Each pre-diluted P/S solution was prepared in order to match the total final bulk concentration of a spread P/S systems so that only the sample history was varied. Specifically, each stock solution was pre-diluted with 12.5 mL of an aqueous subphase prior to their mixing. Finally,

the total liquid volume was then poured into a 7-cm diameter Petri dish, and the surface of the liquid was cleaned by aspiration to remove any trapped material.

In order to emphasize the role of the polyelectrolyte, the same experiments were performed in absence of polyelectrolyte, i.e. by replacing the polyelectrolyte stock solutions with pure water. These control experiments showed that the same surface excesses were achieved with the two protocols; see later in figure 23. It is reasonable to infer that any differences in the surface excess of the spread films and adsorbed layers for the P/A mixtures therefore derive from the spreading of material due to the dissociation of aggregates.

All the measurements were carried out at room temperature, 23 ± 1 °C.

2.2 Characterization techniques

In the following chapter, the six primary instrumental techniques (2 bulk techniques and 4 surface-sensitive techniques) used for the characterization of the samples are described.

2.2.1 Turbidimetry

The turbidity (τ) or optical density (O. D.) of a dispersion is defined as the logarithm of the ratio between the intensity of the light beam passing through a reference cell (I_0) and the intensity of the transmitted from the sample cell (I_t):

$$O.D. = log\, {}^{I_0}/_{I_t} \tag{10}$$

The intensity of the transmitted beam must decrease due to light scattering and not because of absorption of radiation (valence electron transitions). For this reason, it is needed to perform O. D. measurements away from any adsorption band of the components of a dispersion.

The turbidity of NaPSS/DTAB solutions was measured using a Perkin-Elmer Lambda 2 UV-Vis Spectrophotometer with a semi-micro quartz cell of 1-cm path length. The optical density of samples was determined at 400 nm ($O.D._{400}$). Measurements were carried out both at 5 min (fresh) and 1 month after mixing. Since neither the polyelectrolyte nor the surfactant has an adsorption band above 350 nm, increasing $O.D._{400}$ values indicate the presence of aggregates suspended in the samples, while a reduction in the values with time is symptomatic of precipitation. The turbidities of Pdadmac/SDS and PEI/SDS mixtures were obtained from the literature.[91-93]

2.2.2 Electrophoretic mobility

The electrophoretic mobility, μ_e, is defined as the velocity of a dispersed particle (v) under the influence of an electric field (E).

$$\mu_e = {}^{v}/_{E} \tag{11}$$

For any particles, the electrophoretic mobility depends on its surface potential (ζ-potential) as well as the viscosity of the dispersant.

$$\mu_e = \frac{\varepsilon\zeta}{\eta} \tag{12}$$

where $\varepsilon = \varepsilon_0\varepsilon_m$, is the product of the electric permittivity of vacuum (ε_0) and the permittivity of the dispersant (ε_m), ζ is the ζ-potential of the particle and η is the viscosity of the medium. The electrophoretic mobility can be either positive or negative, according to the sign of ζ.

The electrophoretic mobility of the complexes in freshly-mixed NaPSS/DTAB solutions was measured to characterize the sign of their charge and determine the point of charge neutrality. A Malvern Zetasizer NanoZ instrument was used on the basis of the M3-PALS technique. In this technique, a combination of laser Doppler velocimetry and phase analysis light scattering is used to determine the particle velocity. The standard error in the values of the electrophoretic mobility was around 10 %.

2.2.3 Surface tensiometry

Surface tension (γ) is a force exerted on the unit length of the perimeter (l) of a surface (A) which is opposed to any increase of a liquid surface (δA). The surface tension of a pure liquid phase coincides with its surface free energy.[114] Surface tension arises from the excess of energy of the molecules at an interface compared to the bulk. The shape of droplets, the capillary forces and the capillary waves, the contact angle of a drop of liquid with a solid subphase (or with another immiscible liquid) as well as cohesive wetting, spreading, adsorption and depletion of material are all determined by changes in surface tension.

Measurements of surface tension can either be “force measurements”, in which the pull exerted by the liquid meniscus on a ring[115] or on a plate[116] (Wilhelmy method) is measured, or they can be “shape-based”, in which the shape of a sessile drop or a bubble is related to the surface tension of a liquid.[115] The use of light-diffraction from the capillary waves of liquid interfaces has also been reported.[117,118] In this thesis work, however, only the Wilhelmy method is used, in which the exerted force of a liquid wetted plate is measured. A schematic representation of a wetted plate is given in figure 8. The plate is connected to a very sensitive balance.

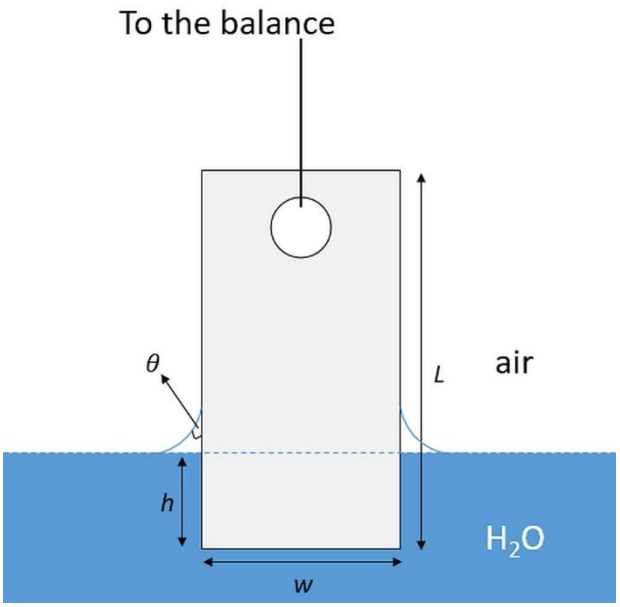

Figure 8 – Schematic representation of a Wilhelmy plate at the air/water interface. *h* and *w* are the wetted height and width of the plate, respectively. *L* is the total length of the plate. θ is the contact angle (exaggerated for visual reasons).

The total force acting on the plate is:

$$F = \rho_{plate} wLtg - \rho_{H_2O} hwtg + 2(w + t)\gamma_{H_2O} \cos\theta \quad (13)$$

ρ_{plate} and ρ_{H_2O} are the densities of the plate and water respectively, g is the gravitational acceleration, h is the height of the liquid measured from the liquid surface to the bottom of the plate. w, L and t are the width, the length and the thickness of the plate. θ is the contact angle. The first term of Eq. 13 is the weight of the plate. If a plate made of filter paper is used, then the plate needs to be completely wet. The second term is the Archimedes pull, the third is the force exerted by the liquid meniscus on the plate.

The instrument measures a surface pressure (π_{film}), which has the same units of measurements of surface tension and it is related to the surface tension by the following equation:

$$\gamma_{solution} = \gamma_{H_2O} - \pi_{film} \quad (14)$$

The surface pressure is measured at constant immersion, so that the Archimedes pull as well as the gravitational contribution will remain constant over the whole experiment, allowing us to reduce Eq. 13 into the form:

$$F = 2(w + t)\gamma_{H_2O} \cos\theta \quad (15)$$

Moreover, since the plates are hydrophilic (usually they are made of filter paper or hydrophilic platinum) the contact angle is (close to) zero and equation (15) becomes finally:

$$\gamma_{H_2O} = \frac{F}{2(w+t)} \quad (16)$$

which is typically presented in units of mN/m.

Surface pressure and surface tension data can be recorded at constant temperature (isotherms). Isotherms can be of different types: they can be *dynamic*, when measured at constant bulk composition as a function of time (adsorption, desorption and, more generally, any processes occurring at an interface); *static*, when the bulk concentration is varied (a useful tool for the determination of the cmc of surfactants); *compression*, when the variation of the surface pressure is caused by the compression of the interface; *cyclic* (or surface pressure vs. area isotherms) when performed during consecutive compression/expansion cycles of the air/liquid interface. When following the surface pressure behavior with respect to the compression of the an insoluble monolayer, it is possible to access molecular parameters such as the area occupied by each single molecule (area per molecule), the phase transition in a monolayer (from gas-like phase to condensed phases) until the collapse of the monolayer, where the surface tension remains constant. The value at which the collapse of the monolayer is observed defines the compressibility of the monolayer: $\beta \propto -\frac{1}{A}\frac{d\gamma}{dA}$ (A is the area at which the collapse is observed). Lastly, *surface elasticity measurements* are performed by perturbing the interface with an oscillatory mechanical stress, often through moving barriers. In this latter case, the surface complex modulus is attained: [46,107,119,120]

$$\varepsilon = \varepsilon' + i\varepsilon'' = -\frac{d\gamma}{dlnA_t} \quad (17)$$

where ε' and ε'' are respectively the elastic and the dissipative modulus of the interface and A_t is the total surface.

In this thesis, the investigation of the surface tension behavior has been carried out with respect to the total area of a Langmuir trough, during consecutive compression/expansion cycles of the interface. The surface pressure was monitored through the Wilhelmy method, with a plate made of filter paper.

Three different instruments with the same experimental setup have been used. The NR experiments and the BAM experiments have been performed on two Langmuir troughs, both produced by Nima (Coventry U.K.), with surface area 283 × 100 mm^2 and 900 × 100 mm^2 respectively. The surface pressure measurements combined with ellipsometry were performed on a smaller trough (surface area 180 × 50 mm^2) produced by Biolin scientific.

2.2.4 Ellipsometry

In ellipsometry, the change in polarization of polarized light upon reflection from an interface between two media of different refractive indices is used to investigate the thickness and the

dielectric properties of films present at the interface. It is a versatile and powerful tool with applications ranging from the characterization of electronic devices to the study of organic thin films. A schematic representation of an ellipsometry measurement is given in figure 9.

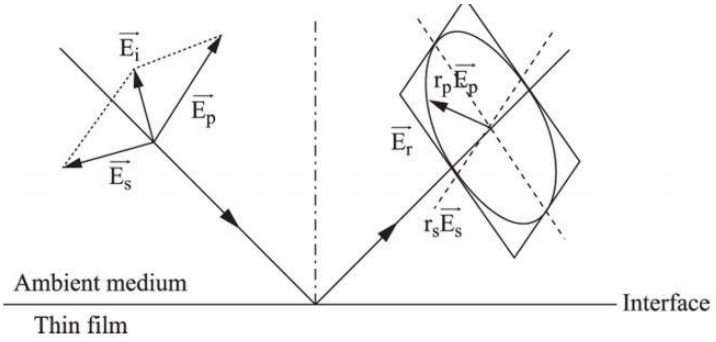

Figure 9 – Representation of the change of polarization of a light beam upon reflection. Images taken from ref. x158

The change in polarization is defined by the ellipticity, ρ, which is the ratio of the reflection coefficients for s and p-polarized light, r_s and r_p:

$$\rho = \frac{r_p}{r_s} = tan\Psi e^{i\Delta} \tag{18}$$

The ellipsometric angles Ψ and Δ are respectively the change in amplitude of the electric field of the light beam and the phase shift upon reflection. These angles vary upon reflection from any bare interface, if any layers are present. Their contributions can be evaluated using an optical matrix method applied to stratified layers between ambient and bulk media. Both Ψ and Δ depend on the dielectric properties of all materials (i.e. refractive indices and dielectric functions), the wavelength of the light, the angle of incidence and the thickness of the layer. This is strictly valid for the reflection of light at non-transparent interfaces. For transparent and non-adsorbing surfaces (as the air/water interface) in the thin film limit, the variation of Ψ is low, [121] while Δ is much more sensitive to the presence of material at the interface and its abundance.

The ellipticity of a layer present on a transparent interface (like the air/water interface) can be calculated by the following relation:[122]

$$\rho = \frac{\pi}{\lambda}\frac{\sqrt{1+\varepsilon_{H_2O}}}{1+\varepsilon_{H_2O}}\eta \tag{19}$$

where ε_{H_2O} is the dielectric function of water for a given wavelength, λ, of the incoming radiation and η is the ellipsometric thickness, which should be noted as an optical thickness rather than an actual structural variable. For a transparent monolayer at the air/water interface, η becomes:[113,122-124]

$$\eta = \int_0^z \frac{[\varepsilon(z)-1][\varepsilon(z)-\varepsilon_{H_2O}]}{\varepsilon(z)}dz \tag{20}$$

η depends also on the phase shift of the layer, the bulk properties of the subphase and on the angle of incidence. The last two parameters are incorporated in a function, $g(\theta)$.[125]

$$g(\theta) = \frac{4\pi\sqrt{\varepsilon_{air}\times}\varepsilon_{H_2O}\times\cos\theta\sin^2\theta}{(\varepsilon_{H_2O}-\varepsilon_{air})\times(\varepsilon_{H_2O}+\varepsilon_{air})cos^2\theta-\varepsilon_{air}}. \quad (21)$$

$$\eta = \Delta_{film}\lambda/g(\theta) \quad (22)$$

The difference in phase shift, $d\Delta$ ($d\Delta = \Delta_{film} - \Delta_{H_2O}$), is a known parameter since both Δ_{film} and Δ_{H_2O}. Are directly measured during a typical dynamic ellipsometry experiment. Finally, a relation between the ellipsometric thickness and surface excess can be derived using Fejiter's equation.[121,125,126]

$$\Gamma = \frac{\sqrt{\varepsilon_{film}-\varepsilon_{H_2O}}}{dn/dc}\eta \quad (23)$$

Where ε_{film} is the dielectric function of the interfacial film, ε_{H_2O} is that of water, and dn/dc is the refractive index (n) increment. The combination of Eq. 22 and Eq. 23 gives:

$$\Gamma = \frac{\sqrt{\varepsilon_{film}-\varepsilon_{H_2O}}}{dn/dc}\times\frac{\Delta_{film}\times\lambda}{g(\theta)} \quad (24)$$

However, the relation between Γ and Δ_{film} is model-dependent. In particular, two limiting models can be identified: 1) constant layer density and varying thickness (oil-like behavior); 2) constant layer thickness and varying density or coverage (particle-like behavior).[127] In the first model, the surface excess is linearly proportional to Δ_{film} and by incorporating all the constant terms appearing in Eq. 24 :

$$\Gamma = A\times\Delta_{film} \quad (25)$$

In the second model, ε_{film} varies with the coverage, and the relation between the surface excess and the phase shift becomes quadratic:

$$\Gamma = B\times\Delta_{film} + C\times{\Delta_{film}}^2 \quad (26)$$

The parameters B and C can be derived from an empirical fit to a simulation of Eq. 24. It should be pointed out that this way of deriving the surface excess has some drawbacks. In detail, the technique is accurate only for single-component organic films whose dielectric function in the direction normal to the interface, therefore the refractive index, is isotropic. For ionic surfactant or mixtures of organic components, this is not always the case and the calculation of the dielectric properties of the interfacial films is not trivial, as any optical inhomogeneity decreases the accuracy of the technique.[128,129]. For this reason, it is preferred to calibrate the ellipsometric data by the means of other techniques, such as NR.[102]

The instrument used for all the ellipsometry experiment in this thesis is a Beaglehole Picometer Light ellipsometer, with a wavelength of λ = 632.8 nm, an angle of incidence of θ = 50°, and a data acquisition rate of 0.2 Hz. The angle of incidence was kept below the Brewster angle of pure water (53.1°) because of operational reasons related to the alignment and sample manipulation.

2.2.5 Brewster angle microscopy

BAM can be thought as an application of ellipsometry for imaging the lateral inhomogeneity of films present on a transparent interface. The detector is a CCD camera which records simply the intensity of the reflected beam over a given area (usually around 1mm^2). The technique is sensitive to any micron-sized optical inhomogeneity present in the plane of the interface. However, by taking some precaution, even a homogenous film can be detected. The mathematical expression for θ_B is:

$$\theta_B = \tan^{-1}\frac{n_2}{n_1} \tag{27}$$

where n_1 and n_2 are the refractive indices of the ambient and the substrate, respectively. The Brewster angle (θ_B) is also called the polarization angle, because at θ_B only the s-polarized component of light is reflected from a perfectly flat interface, while the p-component is fully transmitted. If the refractive index of the pure interface is modified, for example when a film of material is present, some of the p-polarized light can be reflected as well.

Operationally, there are two ways of performing a BAM experiment. The first method consists of recording a background for the pure interface by using both p and s-components of light at a fixed low intensity. This is done by setting both the polarizer and the analyzer angles at relatively high values (away from p-polarization) and adjusting the amplification of the signal until the counts in the region of interest (ROI) are kept low enough, but still higher than the instrumental background (dark currents and the brightness of the environment). After, an image of the surface is taken and set as background. The second step is the correction of the focal distance, sketched in figure 10. The light-grey rectangle is the camera at the bottom of which the CCD sensor is located, and the green lines represent the path of the light. Due to the high collimation of the light, as a laser is used, only a very small portion of the interface (small black solid line on the interface in figure 10) will actually be at the correct focal distance (indicated by a dashed line). The remaining positions toward the edge of the image will be out of focus (red lines). Correction of the focal distance means finding the focal spot and setting it as the correct distance. When the auto-focusing is on, the lens of

the camera moves toward and away from the surface while the image is recorded continually so that a larger portion of the laser spot will be correctly focused. Air bubbles or dust particles on the surface are used, generally, to find the correct focal distance, if there are not specific lateral features at the start of an experiment. It is a good procedure to perform this step before recording the background.

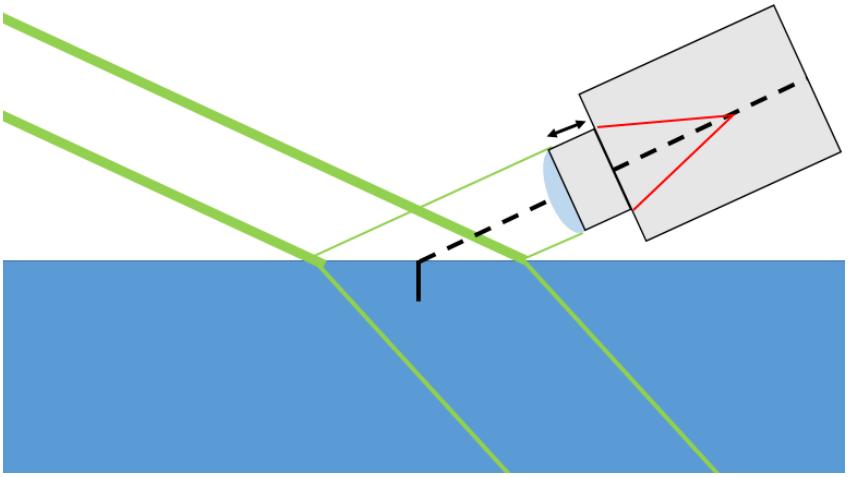

Figure 10 – Schematic representation of BAM. The green lines describe the optical path of light. The dashed line indicates the correct focal distance while the small solid line at the interface represents the area of the surface with the correct focus. The red lines are used to display examples of wrong focal distances. The black double-arrow indicates the direction in which the lens moves.

In a third step, the analyzer angle is minimized, to get close to the p-polarization, and the amplification of the signal is increased until the counts in the ROI match those of the background. Then, an image of the sample is taken and the previously recorded background is subtracted. However, this procedure is not always possible at the air/water interface, because of the highly dynamic nature of some surface films. This represents a strong limitation to background subtraction when BAM is performed at the air/solution interface. One way to overcome this issue is to disable automatic focus correction, but in this way only a small portion of the image is correctly displayed. This procedure was used in the preliminary study on the properties of DF-HSA films at the air/SPB interface (chapter 3.1) as well as for NaPSS/DTAB films spread from neutral aggregates (chapter 3.2). Moreover, an active anti-vibration system is required. Vibrations of the interfaces destabilize the intensity of the signal making it oscillate rapidly. Consequently, if automatic focus correction is enabled, brighter and darker rectangular bands (flickering) will be displayed, overlapped with the image of interest. The flickering is caused by the different rates of acquisition of the image (the movement of the lens) and the frequency of the oscillation of the signal.

The second method to perform BAM experiments consists of setting to zero both the polarizer and analyzer angles so that only p-polarized light will be used. In this way, a bare

interface will always be invisible (black image), regardless of the amplification of the signal. No background subtraction is needed. This aspect gives the technique the advantage of becoming sensitive also to optically homogenous layer, which will appear as a grey image. This approach was used to investigate the lateral features of NaPSS/DTAB films spread from aggregates with different charge/structure (chapter 3.3). In addition, if the signal amplification is kept constant, an increase in the intensity is a symptom of higher density of material at the interface. A drawback is represented by the fact that the intensity is, generally, lower and has decreased contrast compared with the first approach.

The measurements in this thesis were made using a Nanofilm EP3 machine equipped with an Nd:YAG laser and a 10× objective at the Brewster angle for the air/water interface of 53.1°.

2.2.6 Neutron reflectometry

As NR is the primary experimental technique used in this thesis, its description is more detailed than those described previously. Before, a brief and general introduction to neutron scattering is given in the next paragraph.

Interaction of neutrons with matter

The scattering of neutrons, light and X-rays follows the same mathematical description, although with different refractive indices, n. The difference arises from the potential of interaction between the probe particle and matter. Neutrons interact with nuclei and this interaction depends on the density of scatterers (the nuclei of a sample) as well as their scattering power, which is expressed by the nuclear scattering length, b. This latter quantity appears in the expression of the potential of interaction of neutrons with matter, known as the Fermi pseudo-potential. From the quantitative point of view, the Schrödinger equation must be used to resolve the energetics of a scattering process: [130]

$$-\frac{\hbar^2}{2m_n}\nabla^2(\Psi) + V(\Psi) = E(\Psi) \quad (28)$$

The quantum operator $-\frac{\hbar^2}{2m_n}\nabla^2$ defines the kinetic energy of the neutron (free particle), $\hbar^2$is the Dirac constant and m_n is the neutron mass. V is the Fermi pseudo-potential.[131.]

$$V = \frac{2\pi\hbar^2}{m_n}\rho_b \quad (29)$$

ρ_b is the scattering length density (SLD) and it is equal to:

$$\rho_b = \sum_i b_i\, n_i \quad (30)$$

n_i is number density of scatterers, i.e. the number of nuclei per unit volume, and b_i is the scattering lengths of each nucleus in the sample. The latter quantity has been measured for most of the elements. As for X-ray scattering techniques, the scattered intensity is proportional to ρ for a single scatterer. If two (or more) different scatterers are present in the sample, the intensity of each component with respect to the others (atoms, particles, surrounding medium…) is proportional to the difference in scattering length density, $\Delta\rho$ (contrast), between the components. For X-rays the scattering length density is proportional to the electronic density, which ultimately varies with *Z*, the atomic number. Neutron scattering lengths are aperiodic along the table of elements. Moreover, since isotopes of the same element have different nuclear structure (different mass number), a neutron interacts differently with each of them. The main advantage of NR compared to X-ray reflectometry (XRR) comes from this peculiarity: one can enhance the contrast by substituting an isotope

with another (isotopic contrast variation). In addition, while the electronic density is always positive, the nuclear scattering lengths of neutrons can also assume negative values, like for the nucleus of protium, the most abundant isotope of hydrogen. Some examples of nuclear scattering length values for the most common elements in soft organic matter are shown in figure 11, divided by 10^{-6}. The unit of measurement is $Å^{-2}$.

Protium	Deuterium	Carbon	Nitrogen	Oxygen	Phosphorus	Sulphur
-3.74	6.67	6.65	9.36	5.81	5.13	2.85

Figure 11 – Nuclear scattering lengths of some of the most common nuclei in soft organic matter. The values are divided by 10^{-6} $Å^{-2}$.

Thanks to this feature, it becomes also possible to match the SLD of a species to that of its chemical environment, making the species invisible to neutrons. The SLD of a sample composed of i species can be written as:

$$\rho_{sample} = \sum_i \rho_i \varphi_i \quad (31)$$

where φ is the volume fraction that satisfies the condition:

$$1 = \sum_i \varphi_i \quad (32)$$

A species is said to be contrast matched when its SLD equals the one of the chemical environment or another species. Thus, to prepare a contrasted matched species one needs simply to solve equations 31 and 32 simultaneously. This procedure represents another advantage of neutron scattering over X-ray scattering techniques in soft condensed matter, structural biology and biophysics, since organic compounds are abundant in hydrogen atoms, as the SLDs of protium and deuterium are not only different but also opposite in sign. Thus, for example, CH_2 groups are almost invisible to neutrons, while their deuterated analogues, CD_2, are strong scatterers. Moreover, the wavelengths of neutrons used in scattering experiments (thermal neutrons, up to a few decimals of nanometers) are comparable with the dimensions in soft matter systems. This means that, when neutrons are scattered, the interference between scattered waves occurs, and the resulting diffraction patterns allow one to resolve the structural details of a given system. This aspect combined with the possibility of performing isotopic contrast variation of the samples results in the resolution and localization of the structure individual components in complex matrices, and by measuring more than one contrast it is possible to attain a detailed picture of the structure of the whole sample, as well as its composition.

Specular reflection of neutrons from flat surfaces

Among the neutron scattering techniques, NR is one of the oldest. NR was first demonstrated and used by Enrico Fermi and Walter Zinn almost 80 years ago, who exploited the total external reflection of neutrons from bare interfaces to accurately determine the scattering power, i.e. the nuclear scattering lengths (consequently the SLDs), of samples. Total external reflection occurs below a given angle, known as critical angle θ_c, which is characteristic of all materials and is directly proportional to the square-root of difference in SLD between the two media as well as the neutron wavelength.

$$\theta_c = \sqrt{\Delta\rho\lambda^2/\pi} \tag{33}$$

Indeed, NR has been successfully used for the characterization of the structure and the composition of different materials, ranging from metal layers,[132] to magnetic films[133]; from semiconductors[131] to soft organic interfaces[102,103,127] and atmospheric chemistry[134].

When a neutron (wave) travels through an interface between two media with different refractive indices, it can get transmitted, reflected or adsorbed. A sketch of transmission and reflection is given in figure 12. The refractive index, n, for neutrons depends on their wavelength, as well as the nuclear scattering power of the interface: [59]

$$n = 1 - \frac{\lambda^2}{\pi}\rho \tag{34}$$

As the values of refractive indices for the short neutron wavelengths are very close to 1, it is more convenient to discuss in terms of SLDs.

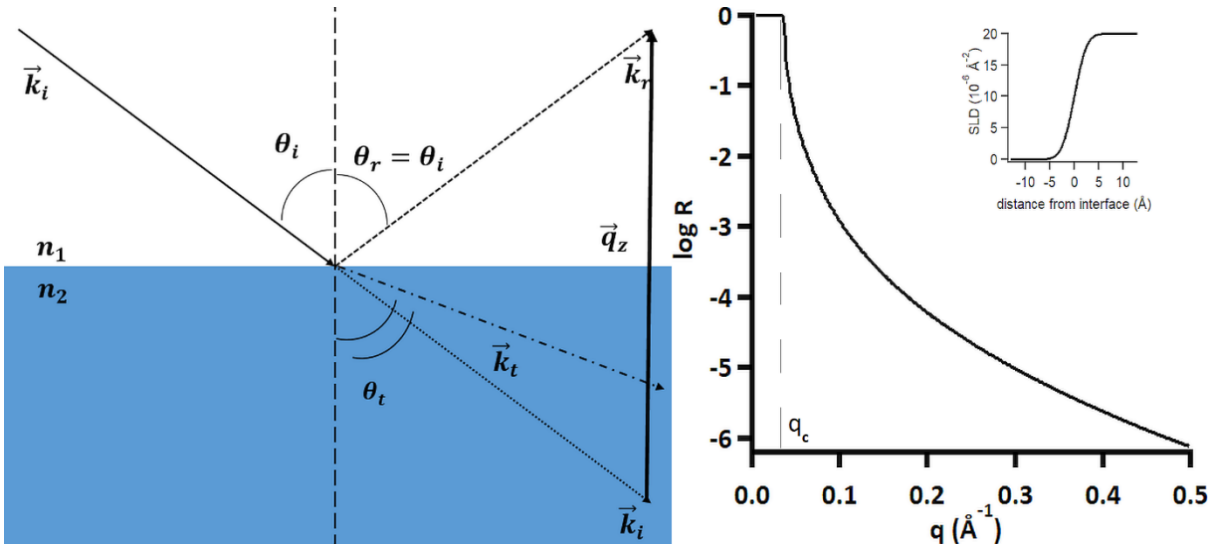

Figure 12 - left: schematic representation of reflection and transmission. The directions of propagations of the wave packets (neutrons) in the two media with different refractive indices are represented by a continuous arrow before reflection, a dot-dashed arrow for the transmitted (refracted) and a dashed arrow for the specularly reflected beam; right: simulation of a fictitious bare interface between a medium with high SLD and air. The q_c is marked by a vertical dashed line. A fixed roughnes value of 4 Å was used.

The reflectivity (R) is defined as the ratio between the intensity of the reflected beam (I_r) over that of the direct beam (I_0), $R = I_r/I_0$. The values of R depend on the difference in SLD between the two media, $\Delta\rho$, as well as the angle of incidence, θ, of the incoming neutron beam. The component of the wave vector, k, which defines the direction and the energy of a travelling wave packet, along the direction normal to the interface (z-direction) is defined, as:

$$k = \frac{2\pi}{\lambda}\sin\theta \tag{35}$$

NR is an elastic technique, which means that only the direction of the waves is changed upon the interaction with the surface and not the energy of the particles. Thus, the moduli of the incident and the reflected wave vectors are the same and the "momentum transfer" across the interface (q), which is the difference between these two wave vectors (see figure 12), is defined from Bragg's law.

$$q = \left|\vec{k}_i - \vec{k}_r\right| = 2k\sin\theta = \frac{4\pi}{\lambda}\sin\theta \tag{36}$$

A neutron reflectivity measurement is, typically, performed by varying both the angle of incidence and the reflection angle by the same amount. Therefore, also q is varied. If a monochromatic beam is used, varying the angle of incidence is the only way to scan the accessible reciprocal space. The reflectivity profiles are generally plotted as R (or $logR$) vs. q. As an alternative, one can plot the reflectivity as Rq^4 vs. q in order to eliminate the Fresnel components and emphasize structural features at high-q values, which carry information about the internal structure of the investigated layer. The monochromatic option is always used in XRR, since all photons travel at constant speed (the speed of light, *c*) regardless of their wavelength. The instrumental resolution on q (dq/q), in this case, is equal to the uncertainty on the angle of incidence ($d\theta/\theta$), due to the divergence of the beam, assuming that the uncertainty on λ ($d\lambda/\lambda$) is much smaller and may be neglected. In order to minimize $d\theta$ a good collimation system as well as a slow scan of θ are required. Because neutrons have mass, their speed depends on their wavelength, which can be calculated by using the de Broglie equation. This means that neutrons with different wavelengths will be detected in different times, and this allows one to perform *time-of-flight* (TOF) measurements by exploiting a pulsed (or chopped) polychromatic (or white) beam. In this case, the pulses are created by spinning discs with small opening, called choppers. Due to the low brilliance of most of the actual neutron sources, the TOF option is preferred in NR because it allows the possibility of acquiring data from multiple wavelengths at once. Thus, in TOF-mode only a small number of angles are required to scan the accessible reciprocal space before the signals

reaches the background value. In the leading instruments, the number of angles required for acquiring a full profile can be as low as 2. This represents the biggest advantage of TOF-NR over monochromatic NR because it reduces the time required to acquire a full-q reflectivity profile, thus allowing one to perform kinetics study at surfaces. However, the instrumental resolution is lower than the monochromatic option.

The neutrons scattered from the sample are collected, usually, by 2D-detectors. In these detectors, one of the two dimensions is position-sensitive (position of the reflected neutron beam) while the other is the wavelength-dimension. An advantage of using such detectors derives from the fact that, in this way, also the scattering out of the specular position (off-specular scattering) is detected. The off-specular scattering at the air/water interface is mostly due to incoherent scattering. However, it may contain information about any structure present in the plane of the subphase and, in some cases, can bring useful insights for the analysis of the specular reflectivity. The 2D-scattering patterns collected (raw data) are then reduced in the more useful $logR$ vs. q form by data reduction software. During data reduction, the background can be subtracted, using the off-specular scattering on one or both sides of the specular reflection on the 2D detector. In principle, NR data are self-normalized, since a ratio of intensities is in absolute units. In practice, one has to take into account that different instrumental setup are used to record the direct and reflected beams. Specifically, an oscillating slit is used to reduce the intensity of the neutrons on the detector during the direct beam measurements to avoid is over-saturation. It is needed therefore to normalize all the data collected at a given angle of incidence using a reference system (such as air/D_2O) below the critical angle, where $R = 1$.

A reflectivity profile for a bare interface is reported in figure 12 as $logR$ vs. q and it can be described as follow. Below a critical q value, q_c, total external reflection occurs, thus log R is equal to zero.

The critical q-value, q_c is characteristic of all materials and an expression for it can be found by combining Eq. 33 and Eq. 36.

$$q_c = \sqrt{16\pi\Delta\rho} \tag{37}$$

Above q_c, the reflectivity falls off rapidly:

$$R(q) = \frac{16\pi}{q^4} \times \left| \int_0^z \frac{d\rho(z)}{dz} e^{iq(z)}\, dz \right|^2 \tag{38}$$

For a bare interface, this is reduced to $R(q) = \frac{16\pi}{q^4}\Delta\rho^2$ as in figure 12. Equation 38 is an important result which tells that the reflectivity coincides with the square of the Fourier

transform of the scattering length density profile along the z-direction. The reflectivity profiles of a homogenous layer deposited onto a flat surface can exhibit local minima and maxima (Kiessig fringes), which arise from the interference between the reflection of the air/monolayer interface and that of the monolayer/subphase interface. The position of the local minima is characteristic of the thickness (d) of the layer as it is proportional to $^{2\pi}/_{d}$. An example is sketched in figure 13.

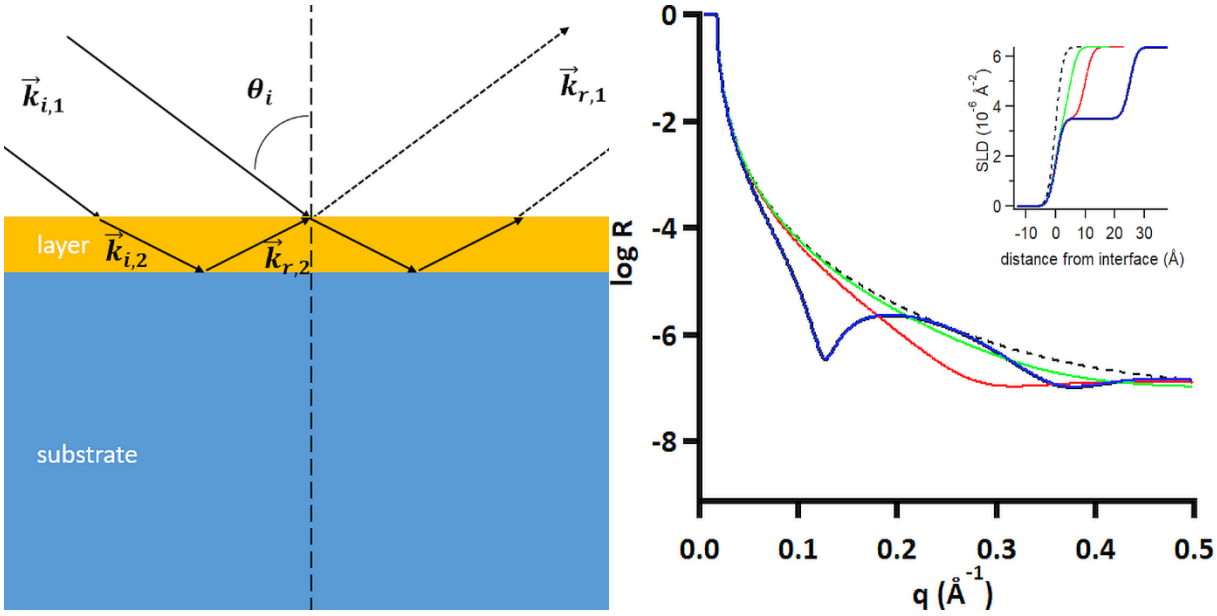

Figure 13 – Left: schematic representation of neutron reflection from a monolayer present on a substrate. k_i and k_r stand for the wave vectors of the incident and reflected wave packet, respectively. The subscripts 1 and 2 indicates on which medium (or at which interface) the neutrons are reflected. Right: simulated reflectivity profiles for the bare air/D_2O interface (dashed line), and 5 Å (green line), 10 Å (red line) and 20 Å layers at same interface. The small inset contains the corresponding SLD profiles. A constant roughness of 4 Å was applied to all the curves.

For N layers, the description gets further complicated since the reflection and the transmission (with refraction) of neutrons will occur at every interface. A recursive approach is then used to calculate the reflectivity of the j-th interface (Parratt formalism):

$$X_j = \frac{R_j}{T_j} = e^{(-2ik_{z,j})} \frac{r_{j,j+1} + X_{j+1} e^{(2ik_{z,j+1} z_j)}}{1 + r_{j,j+1} X_{j+1} e^{(2ik_{z,j+1} z_j)}} \tag{39}$$

where $r_{j,j+1} = \frac{k_{z,j} - k_{z,j+1}}{k_{z,j} + k_{z,j+1}}$ are the Fresnel reflectivity coefficient between the interface j and j+1. The iteration starts with $T_1 = 1$ (the direct beam) and $R_{N+1} = 0$ (no reflection from below the substrate). Alternatively, the Abele's optical matrix method can be used to analyze the reflectivity profile. The description, so far, is strictly valid for perfectly flat interfaces. The effect of roughness (σ) on R, to some extent, can be taken into account. It turns out that the reflectivity is decreased of a factor $e^{\sigma^2 q^2}$. However, such approximation is valid only for

Gaussian distribution of $\sigma(z)$. Generally, the effect of roughness is damping off the reflectivity curves.

Modeling of data

Specular NR is widely used for the characterization of the structure and the composition of thin films at fluid interfaces.[104] The experimental NR data are fitted to the reflectivity of a stratified layer model of the interface. Each layer is defined by three parameters: the layer thickness (d), its scattering length density (ρ) and the layer roughness (σ). Above and below the top-layer there are the two infinite media with known scattering length density, i.e. air and water in this thesis. The reflectivity model is then calculated by the means of the optical matrix method or the Parratt formalism. In reflectometry, the information about the phase is lost, so different models can produce the same reflectivity profile.[135] A way to overcome this issue is to fit the reflectivity profiles of several isotopic contrast to the same model. This procedure is known as global fit of the data. Additional accuracy is achieved by the use of structural and/or stoichiometric molecular constraints.[136] Once an approximated model is applied, the surface excess can be calculated by the following relation:

$$\Gamma = \frac{1}{N_A \times A_m} = \frac{\rho \times d}{N_A \sum_i b_i} \tag{40}$$

where N_A is the Avogadro's number and A_m is the molecular area.

The air/water interface and the low-q approach

All the NR experiments reported in this thesis work have been performed at the air/ACMW air contrast matched water (8.1 % v. D_2O in H_2O, $\rho = 0\ Å^{-2}$), which is transparent to neutrons. Thus, any reflection from the interface occurs only if material is present. For a single layer at the air/ACMW interface, the reflectivity can be written as:[122]

$$R(q) = \frac{16\pi}{q^4} {\rho_{layer}}^2 \sin^2\left(\frac{qd}{2}\right) \tag{41}$$

from Eq. 41, it is evident that the reflectivity of a monolayer depends on the scattering power of the layer (ρ_{layer}) and its thickness (d). Calculations of the surface excess of single-component monolayers are very straightforward and one needs to solve Eq. 40 for just one contrast using data at low-q. This way of calculating the surface excess from low-q reflectivity data is a novel approach that is gaining more and more visibility, thanks to its fast application to deuterated monolayers or more generally to good scattering systems. It has been proved that, for such system a few seconds of acquisition time (up to one minute) is enough to resolve the scattering of a single species at the air/ACMW interface.[104,134,137] This features allows TOF-NR to be one of the most accurate and reliable technique to study the

evolution of a process on the liquid surface. This is done by the means of kinetic scans, equally spaced in time (time slab). Adsorption, desorption, the interaction of target molecules with a model monolayer and also chemical reactions can be followed *in situ* while varying the experimental conditions.

For multi-component systems, like a P/S mixtures, the approach is slightly more complicated by the fact that, in this case, more contrasts need to be collected. The rule is one contrast for each interfacial component in mixed systems. This situation is illustrated in figure 14, where simulated reflectivity profiles of deuterated (red and blue) and hydrogenous (green dashed and light-blue) monolayers. Each set of curves has been constrained to have the same surface excess since they are contrast-variation of the same sample, but they have different density and thickness. The SLD and the layer thicknesses were varied within the same contrast, but their fitted product was kept the same. The corresponding scattering length density profiles are reported in the small inset with matching colors. The reflectivity of the bare interface (dashed line) corresponds to the background and has been set to 10^{-5}.

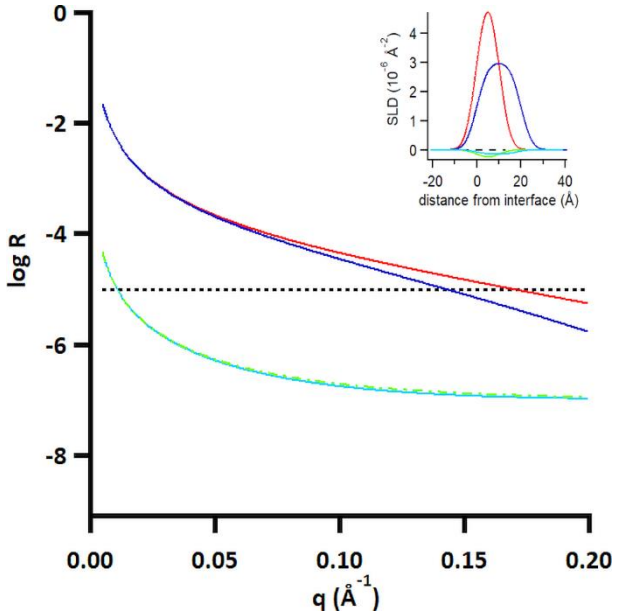

Figure 14 – Simulated reflectivity profiles of deuterated (red and blue) and hydrogenous monolayers (lightblue and green dashed lines) of layers with different thickness and SLD, but the same surface excess. The small inset contains the corresponding SLD profiles, desplayed with matching colors.

For the simulation in figure 14, the q-range has been reduced from that of figure 12 and figure 13 because even the reflectivity of even a deuterated monolayer above 0.3 $Å^{-1}$ falls rapidly below the background, even for top performing instruments.

For the two simulations of deuterated material with different density, the reflectivity profiles start to diverge above 0.05 $Å^{-1}$. The effect of the layer thickness starts becoming significant above this value, while it is not detectable for hydrogenous material, as these simulated

curves are well below the background in this q-range. The scattering excess, defined as the amount of material with respect to its SLD (with respect to the background) is equivalent for each set of contrasts at low-q values, below 0.05 $Å^{-1}$. In this region, the reflectivity is insensitive to the structural features of the chosen model. Thus, fitting of the layer thickness while keeping the SLD constant or vice versa, will produce the same surface excess. This means that only the fitted product $\rho \times d$ determines the surface excess that can be accurately calculated by applying Eq. 40 to different contrasts and solve the resulting system of equations. From these considerations it follows that the product $\rho \times d$ for a single-layer model containing i-species can be written as:

$$(\rho \times d)_i = N_A \cdot \sum_i \Gamma_i \cdot b_i \quad (42)$$

Note that Eq. 42 reduces to Eq. 40 when the sample is composed of a single species. Most of the work in this thesis was focused on P/S mixtures composed of NaPSS and DTAB. Since the hydrogenous surfactant have a negative SLD, it is possible to contrast match the surfactant to both air and ACMW. In this contrast (h-NaPSS + cm-DTAB), the contribution to the specular reflectivity derives only from NaPSS, which can be subtracted to the second contrast (h-NaPSS + d-DTAB on ACMW) by solving simultaneously Eq. 42 written as:[102]

$$(\rho \times d)_1 = N_A \cdot \Gamma_{h-NaPSS} \cdot b_{h-NaPSS} \quad (43)$$

$$(\rho \times d)_2 = N_A \cdot \Gamma_{h-NaPSS} \cdot b_{h-NaPSS} + N_A \cdot \Gamma_{d-DTAB} \cdot b_{d-DTAB} \quad (44)$$

Nevertheless, there are quite some limitations to the applicability of the new low-q approach either to deuterated or to hydrogenous material and, more generally, to weakly scattering systems. In particular, the strongest limitation comes from the background treatment.[104,134,138] First, the background, which derives from the incoherent scattering of hydrogen atoms of the ACMW subphase, has to be as low as possible in order for NR measurements to be sensitive to the scattering excess ($\rho \times d$) of material at the interface. As it is clear from figure 14, the higher the instrumental background the lower will be the minimum scattering excess with respect to the bare interface. Moreover, the signal of weakly scattering systems, like hydrogenous monolayers at the air/ACMW interface, becomes comparable with the background level. Thus, subtraction of the background from these data will lead to the introduction of a systematic positive error (overestimation) of the surface excess.[138]. These limitations impose to the experimentalist the need for a correct estimation of the level of the instrumental background. In this thesis work, a lot of efforts has been put to the improvement of a previously developed methodology for the data analysis of deuterated single-component monolayer[134,138] and its extension to multi-component organic layers containing hydrogen

atoms at the air/water interface. In detail, consecutive measurements of the reflectivity of the bare air/ACMW interface with different acquisition times have been recorded during all the experiments. In a second step, the evaluation of the background was performed as follow: 1) approximate fitting of the background. This gave a first estimation of the instrumental background; 2) fitting of the thickness of a fictitious one-layer model of fixed SLD, thickness and roughness, while adjusting the background to the lowest value for which the fitted thickness of the fictitious layer was zero (i.e. no material is at the interface); 3) note the value of the background used that satisfies the zero-surface excess requirement; 4) repeat the operation for each scan of the bare interface that has been recorded, and 5) calculate the average value. This way of proceeding gives a fair estimation of the background value necessary that leads to a minimal fitted surface excess of the bare interface, while conserving the sensitivity of the subsequent measurement when material is present at the interface.

However, the reflectivity of a monolayer depends also on the accessible lowest q-range for a given reflectometer. For instance, if the lowest accessible q-value is 0.03 $Å^{-1}$ and its background is 10^{-5}, then the reflectivity of hydrogenous material in figure 14 cannot be measured, since its signal will be below the background. To date, the only instrument in the world which satisfies the requirement to resolve the scattering excess of weakly scattering system is FIGARO, shown in figure 15.

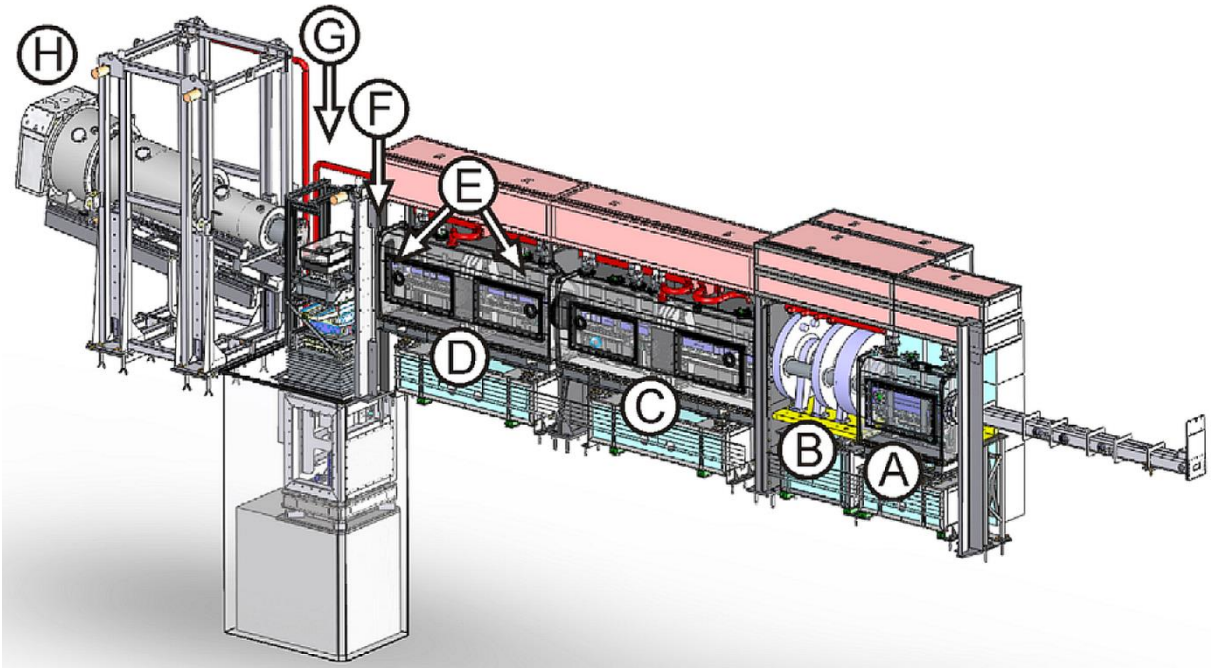

Figure 15 – The FIGARO reflectometer at the ILL with its main components: A) frame overlap mirrors; B) choppers; C) deflected mirrors; D) collimation guide and E) collimation slits; F) beam attenuator; G) sample area; H) 2D detector. Image is taken from ref. 137.

The advantages of FIGARO for kinetic or dynamic measurements at the air/water interface using the low-q approach are multiple. First, the high stability of the ILL reactor source ensures a constant neutron flux to the sample area. Second, the instrument has a low natural incident angle (0.62°), in combination with the possibility of relaxing the resolution in q by using a chopper configuration that produces large neutron pulses. A detailed description of the instrument can be found in refs. 104 and 137. The development of the new low-q data analysis approach would have not been possible without FIGARO. In turn, this technical advance has changed drastically the way the FIGARO instrument at the ILL is being used and it has optimized the time required for NR experiments, which is important given its high associated costs (ca. 20kEUR/day). Many of the scientists interested in interactions at the air/water interface are now structuring their beam time proposals to include a structural element (i.e. full q-range measurements in multiple isotopic contrasts) also with the low-q composition analysis method (i.e. low q-range measurements in 2 specific isotopic contrasts). The latter method has been described thoroughly in a recent review.[104] Published examples in the last year or so include the interaction of antimicrobial peptides with model lipid membranes,[139,140] and interactions of an anaesthetic drug with phospholipid monolayers.[141] Unpublished examples of experiments that have taken place already include P/S interactions of relevance to foam film stability studies, interactions of surfactant monolayers with hexane vapor, and the interactions of fluorinated biomarkers at interfaces mediated by fluorinated gas. These examples include research groups from a range of EU countries.

Chapter 3: Results and discussions

3.1 Preliminary study: surface-loaded films of DF-HSA

In a preliminary study on spread films of macromolecules at the air/water interface, the attention is focused on the surface active defatted protein, DF-HSA. The surface excess, the durability and the morphology of DF-HSA films have been investigated as a function of the sample history, i.e. by comparing the results of films prepared by spreading concentrated aliquots of protein solutions on pure aqueous buffers (surface loading) with those of layers formed by equilibrium bulk adsorption from solutions with equivalent final bulk concentrations, according to the two protocols described in chapter 2.1.2.

The reasons motivating the study of this particular system were twofold. On the one hand, the properties of DF-HSA spread films, and more generally of globular proteins at the air/water interface, have been well investigated over the last decades. Films made of DF-HSA were therefore excellent candidates to practice on, in order to learn about the experimental procedures (sample preparation, surface cleaning and instrumental techniques) that would need to be applied systematically later for the cases of spread films from P/S aggregates dispersions (see chapters 3.1–3.5). On the other hand, this preliminary investigation offered an opportunity to shed more light on an old problem in the field of protein films at the air/water interface, i.e. the effects of the sample handling on the resulting physical properties of kinetically-trapped protein films. The investigation was primarily carried out by conventional laboratory techniques, such as ellipsometry, BAM and surface tensiometry, both at the static air/water interface and under dynamic conditions during consecutive compression/expansion cycles of the interface.

Ellipsometry is a fast and versatile tool to obtain information about the kinetics of film formation. However, it is often preferred to validate the ellipsometry data analysis with a reference from another technique, such as NR. Data for the pre-diluted DF-HSA solutions from ellipsometry and NR are reported in figure 16 with respect to the total bulk concentration of the protein. The layer thickness was obtained from independent XRR measurements.[127] The NR data were modeled only at low-q in ACMW. Ellipsometry, NR and XRR measurements were performed after allowing the surface to equilibrate for 30 minutes. Ellipsometry data were modeled according to a particle-like model, for which the relationship between the surface excess and the phase shift of the layer (Δ_{film}) is quadratic. The relation between the surface excess and the optic phase shift was calculated to be:

$$\Gamma = 0.632\Delta_{film} - 0.0440{\Delta_{film}}^2$$

These results and direct measurements of the surface excess measured by NR are both shown in figure 16. It can be noted that, at low concentration of protein, below 0.01 mg/cm^3, the surface excess values measured by NR are quite scattered. These variations can be attributed to residual kinetically-trapped material at the interface transferred during the sample handling, in spite of cleaning of the surface of the liquid in the trough by aspiration. However, the two sets of data are in good general agreement. Therefore, the evaluation of the surface excess was performed using only ellipsometry for the following experiments.

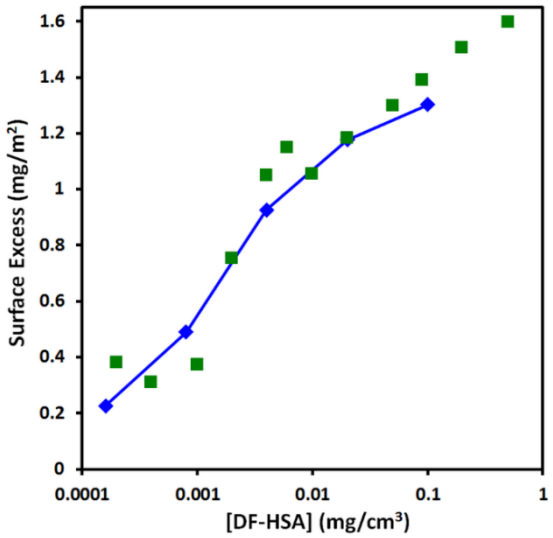

Figure 16- Surface excess of pre-dilutes DF-HSA solutions in standard phosphate buffer (SPB) measured using NR (green squares) and ellipsometry (blue diamonds); the NR measurements were carried out in ACMW (8.1% v/v D_2O in H_2O); line joining the data is a guide to the eye.

Next, it is demonstrated that it is possible to enhance the surface excess at the air/water interface by using the surface loading approach. 1–5 droplets of relatively concentrated protein solution were spread onto the bare air/water surface in comparison with adsorption of protein from the bulk solution. It must be pointed out at this stage that the data presented for the two methods applied have the same final bulk concentrations and that only the pathway for preparing the films was changed. These results are shown in figure 17.

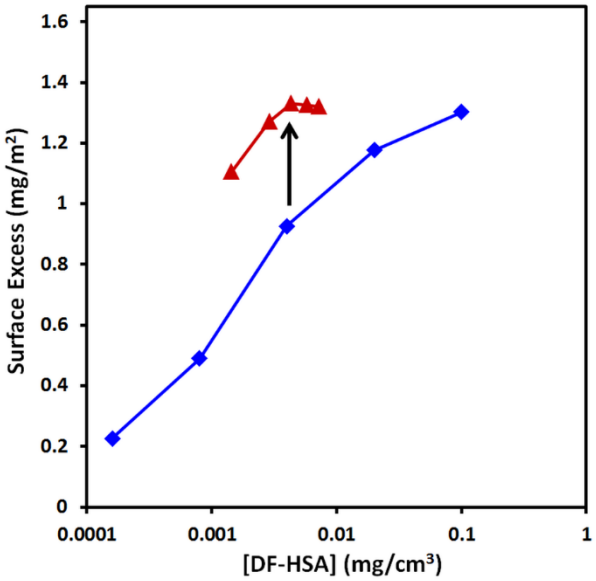

Figure 17 - Surface excess of aspirated DF-HSA solutions pre-diluted in SPB (blue diamonds) and of surface loaded films formed by 1–5 droplets of 1 mg/cm^3 DF-HSA solution on SPB (red triangles) measured using ellipsometry. Lines joining the data are guides to the eye.

It is evident that the surface excess is boosted when the surface loading protocol is adopted. Indeed, the excess of material in comparison to the case of bulk adsorption is trapped out-of-equilibrium conditions and this can be attributed to the lateral interactions between protein molecules in the interfacial layer.[41] Two mechanisms of film formation may be identified. The first involves the direct transfer of material from the surface of the droplets to the air/water interface. However, the total surface area of the droplets, approximated to spheres, falls roughly in the range of 0.6–3 cm^2, corresponding to only 2–10% of the total surface of the trough. This mechanism alone cannot explain quantitatively the amount of extra protein measured at the interface, which exceeds the surface excess of the adsorbed protein films by up to +70%. Thus, the prevalent contribution to film formation is the Marangoni spreading of protein from the bulk of the droplets. These kinetically-trapped protein films remain at the air/water interface over extended time-scales, underlying the non-equilibrium nature of spread protein films.

The effect of the protein concentration on the surface excess of films prepared according to the surface loaded approach was then investigated. Films were prepared at a fixed final bulk concentration either by spreading 1 droplet of 0.1 mg/ml DF-HSA solution or 10 droplets of 0.01 mg/ml. The surface excess was derived from dynamic ellipsometry measurements over half a day, shown in figure 18. Again, it is important to bear in mind that these samples have identical final concentrations of DF-HAS, so the differences in the data can be attributed only

to the experimental pathway, highlighting the relevance of non-equilibrium effects on the properties of DF-HSA spread films.

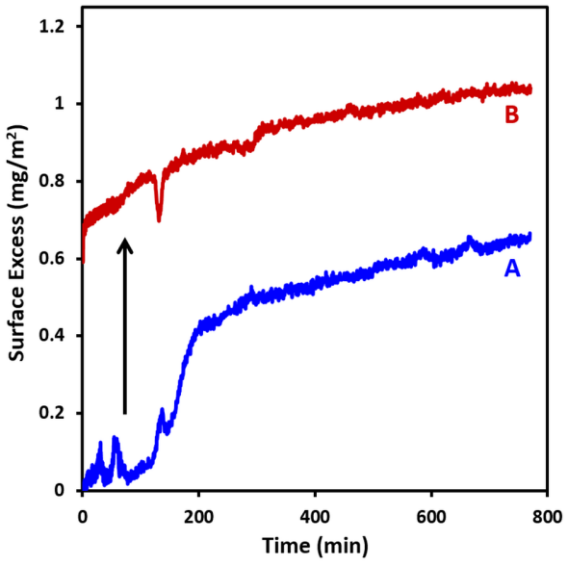

Figure 18- Time-resolved surface excess of (A; blue) 10 droplets of 0.01 mg/cm^3 and (B; red) 1 droplet of 0.1 mg/cm^3 DF-HSA solution spread on SPB measured using ellipsometry.

The comparison shows that the initial surface excess of the film spread from the more concentrated protein solution exceeds that of the lowest concentration by more than one order of magnitude. This information is very important as it shows that the Marangoni spreading of DF-HSA is suppressed if the concentration of protein in the spreading aliquot is not high enough, i.e. if the surface tension of the aliquot is not sufficiently low.[142] Thus, the protein simply dissolves in the bulk, where it becomes available for adsorption.

Other important features of figure 18 are the temporal fluctuations of the surface excess measured by ellipsometry. In general, these are more pronounced at low coverage, as confirmed with measurements on adsorbed DF-HSA layers.[127]These fluctuations can be attributed to lateral inhomogeneity in the surface layer.[143,144] In order to see if it is possible to resolve lateral inhomogeneity present in both spread films and adsorbed layers of DF-HSA, BAM images of four different systems were acquired, shown in figure 19. The images were recorded at a surface age of 5 minutes. The concentrations of the protein solutions correspond to those of curves a and b in figure 18. BAM images revealed that the lateral inhomogeneity in the case of films formed by spreading 10 droplets of a dilute DF-HSA solution (figure 19A) extend over hundreds of micrometers in a loose state with gaps of less material. In the case of samples spread from 1 droplet of the more concentrated DF-HSA solution (figure 19B), for which the surface excess is roughly one order of magnitude higher, protein islands are more densely packed, but still, gaps or regions with less material are visible.

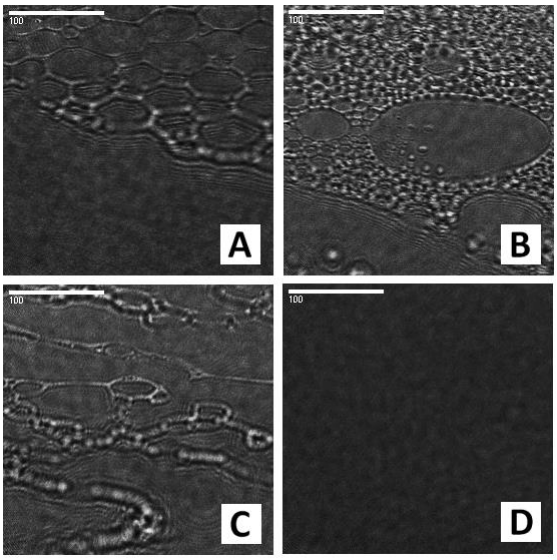

Figure 19 - BAM images of spread films from (A) 10 droplets of 0.01 mg/cm^3 and (B) 1 droplet of 0.1 mg/cm^3 DF-HSA solution on SPB, and adsorbed layers of (C) 0.00080 mg/cm^3, and (D) 0.020 mg/cm^3 DF-HSA in SPB; scale bar is 100 micrometers. The corresponding surface pressures are 1, 1, 1 and 4 mN/m, respectively.

The presence of lateral inhomogeneity was also proven in the case of a layer formed by bulk adsorption from solutions with equivalent final bulk concentrations, in panel c and panel d of figure 19. In detail, A and C, as well as B and D, have, respectively, the same concentrations. These data show that a textured morphology is also attained for the low bulk concentration of DF-HSA (figure 19 C). On the contrary, a homogenous layer is formed when adsorption occurs at higher concentration (figure 19 D). These data reveal some interesting features. In particular, they show that the morphologies of spread films and adsorbed layers at low DF-HSA concentration (A and C) are very similar, indicating that similar films are formed. This is another piece of evidence that the Marangoni flow is suppressed at this low bulk concentration, thus both films are formed by adsorption from the respective bulk solutions. On the contrary, spread films and adsorbed layers are completely different at the highest concentration investigated, which indicates that the non-equilibrium nature of the spread films dictates the morphology of the trapped layer as well, and not only the surface excess of the protein.

Lastly, the comparison between adsorbed layers and spread films of DF-HSA has been carried out under dynamic conditions during 5 consecutive compression/expansion cycles of the air/water interface in a surface pressure vs. area experiment. The data are shown in figure 20 A. The red curves refer to surface loaded DF-HSA films prepared by spreading 10 droplets 0.1 mg/ml, while the blue curves correspond to layers formed by bulk adsorption from solutions with equivalent final bulk concentrations. The data are shaded from light to dark over the consecutive cycles and the large difference can be attributed to the different

experimental methodologies used. In particular, the surface pressure vs. area isotherms of adsorbed layers of DF-HSA (a, blue curves) start at a value that is close to 0 mN/m and it remains almost constant over the whole first cycle. Adsorption is limited by diffusion[127]and, at this low concentration of protein, it takes much more time before enough material is present at the interface to decrease significantly the surface tension of the solution. Over the next cycles, the surface pressure increases steeply at high compression of the interface, which is consistent with slow bulk adsorption. It is worth noting that the expansion curves have exactly the same behavior as during the compression, which indicates that adsorption of protein from the bulk solution occurs on longer time scales than the cycle period and that the protein films are in a fluid phase.

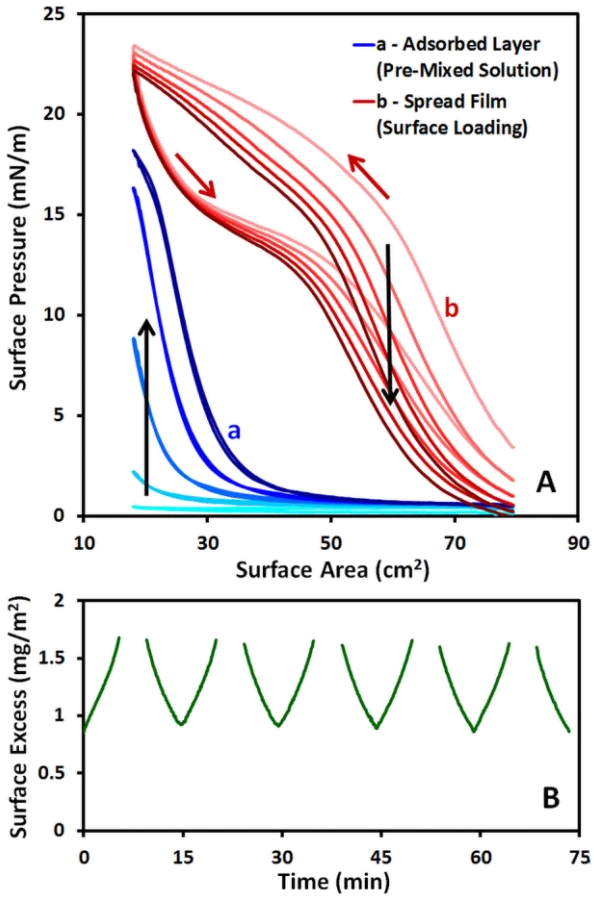

Figure 20 - (A) Surface pressure/area isotherms of 5 compression/expansion cycles on a Langmuir trough for 10 droplets of 0.1 mg/cm^3 DF-HSA in SPB both for (a) adsorption from a pre-mixed solution and (b) a spread film; the diagonal red arrows indicate the direction of compression/expansion in the latter case; the vertical black arrows indicate the progression of the data, shaded from light to dark over the cycles. (B) Corresponding time-resolved surface excess measured using ellipsometry. The compression rate was set to 8.2 mm/min and kept constant over the measurement.

The surface pressure vs. area isotherms of the spread films start at 3 mN/m, and the value increases up to 23 mN/m during the first compression. Upon expansion, the behavior changes and three different surface pressure regimes can be identified. At first, the surface pressure relaxes quickly. Then, it reaches a pseudo-plateau and, in the end, it relaxes to lower values

than those during the compression of the interface, i.e. at the same surface area. After, a limiting cycle is reached, with the maxima in surface pressure decreasing only slightly. Surface pressure measurements alone were not sufficient to resolve the nature of the hysteresis observed during the cyclic compression and expansion of the interface. Moreover, since a decrease in surface pressure is observed from one cycle to the following, there was the possibility that there was a gradual loss of material upon compression from the interface to the bulk. To examine whether or not desorption of the protein molecules occurs when the surface is compressed, the surface excess of spread DF-HSA films was followed by the means of *in situ* dynamic ellipsometry measurements. The data are displayed in panel B of figure 20. The minima represent the surface excess of the fully expanded trough, while the missing data represent full compression; they were not accessible due to the fact that the laser beam hit the moving barrier. These data show clearly that the decrease in surface pressure at full compression over the consecutive cycles cannot be attributed to any material loss, as the surface excess of the fully expanded through is always at the same value. The large hysteresis observed may be interpreted instead in terms of the coalescence of the protein islands during the compression of the trapped layer and by its pulling apart during the expansion until a limiting behavior with higher stability is reached.

To date, this was the first time that the surface pressure behavior under dynamic conditions was related to morphological features of the interface rather than thermodynamic variables. These results were published in 2015,[127] and experience had been gained in the primary experimental methodologies and techniques ready for work on spread films from aggregates in oppositely-charged P/S mixtures.

3.2 NaPSS/DTAB spread films from neutral aggregates

The scope to control and tune the formation of surface loaded membranes composed of oppositely-charged P/S mixtures by exploiting the Marangoni effect is the core idea of this thesis. In this particular chapter, attention is focused on surface loaded P/S films prepared by spreading neutral NaPSS/DTAB aggregates from aqueous media at the air/water interface. In order to demonstrate the non-equilibrium nature of these films, the effects of the sample history are investigated as well, i.e. by comparing the results of spread films from neutral P/S aggregate mixtures with adsorbed layers formed by bulk adsorption of pre-diluted solutions of the two components with equivalent total final bulk concentration. The investigation has been carried out under both static and dynamic conditions.

Before the surface properties of NaPSS/DTAB spread films from neutral aggregates are described, a brief discussion about the charge neutrality point is needed. Figure 21 contains electrophoretic mobility data and $O.D._{400}$ measurements for the 100 ppm 17-kDa NaPSS/DTAB mixtures with respect to the surfactant concentration. The combination of these two techniques is a useful tool for the characterization of the bulk phase behavior and the extent of surfactant binding at the point of charge neutrality.

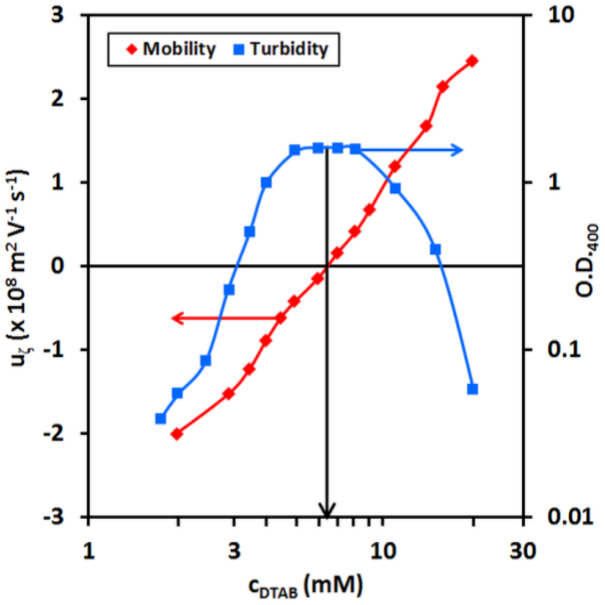

Figure 21 - Electrophoretic mobility data (red diamonds) and $O.D._{400}$ measurements (blue squares) of freshly mixed NaPSS/DTAB samples. Lines joining the data are to guide the eye. The black arrow indicates the point of charge neutrality.

The electrophoretic mobility of the P/S aggregates changes from negative to positive as the surfactant concentration is increased. At charge neutrality (6.0 mM), the electrophoretic mobility of the aggregates is zero, as their motion is not affected by the presence of an electric field. At the same point, the optical density of the P/S dispersion is at its maximum,

indicating the formation of a large number of compact aggregates, containing many polyelectrolyte chains. It has been demonstrated that the surface properties of P/S mixtures are determined by the direct interaction of P/S aggregates with the air/water interface.[92] This interaction can arise from several non–equilibrium mechanisms, such as convection,[110] re-dispersion[91] and sedimentation/creaming,[145] which can result either in depletion of surface active material or enhancement of the surface excesses of the components of a P/S mixture. In addition, it has been observed in a study conducted on a related P/S system that only charged aggregates were detected in the interfacial layer, while neutral aggregates were not detected, indicating that they spread to form a homogenous layer when in contact with the air/water interface.[111] It is worth pointing out that these studies were done on relatively concentrated P/S mixtures, i.e. in concentration ranges comparable to that of the spreading aliquots used for spreading in this thesis. The aim of this chapter is to demonstrate that similar effects can be exploited also in highly diluted P/S systems, since films are prepared by spreading small aliquots of relatively concentrated P/S mixtures onto a large volume of pure subphase by directly contacting the neutral P/S aggregates mixtures with the bare air/water interface.

Neutral P/S aggregate mixtures are not stable due to the lack of colloidal stability caused by the lack of charges on their surface. These aggregates grow in size from a few hundreds of nanometers (500 ± 50 nm) up to one micrometer within 10 minutes, as observed by dynamic light scattering (DLS) measurements. In figure 22, the apparent hydrodynamic diameters of the aggregates are reported as a function of time after mixing the components. Due to high turbidity of the freshly prepared NaPSS/DTAB mixtures, in order to overcome multiple scattering issues, the samples were diluted tenfold with 5.5 mM DTAB solution. This concentration corresponds to the amount of free surfactant present in the mixture, which is a well-defined quantity at the point of charge neutrality since it corresponds to the number of polyelectrolyte monomers in the mixtures (0.5 mM). Since, in this way, the chemical potential of the free surfactant is kept constant in the P/S mixture, the surfactant binding is not affected by the dilution. At the same time, the aggregation rate and the concentration of the aggregates decrease sufficiently to allow the characterization of hydrodynamic size of the NaPSS/DTAB aggregates by DLS. In detail, aliquots of the NaPSS/DTAB mixtures were taken at regular time intervals, diluted and the aggregate size was analyzed.

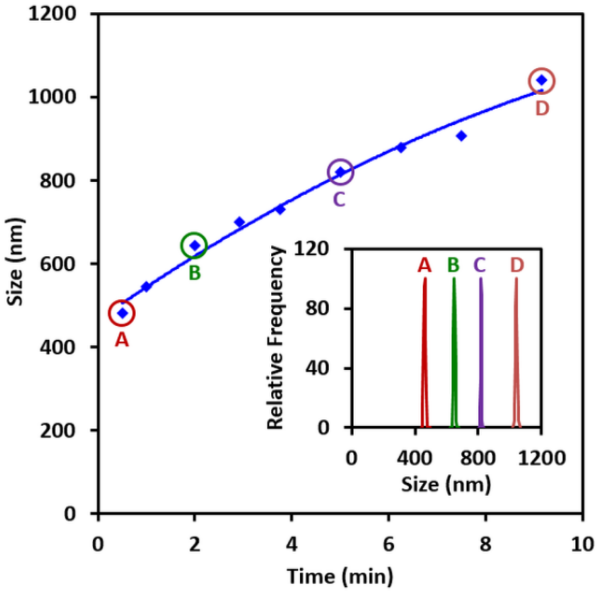

Figure 22 – Average hydrodynamic diameter (size) of NaPSS/DTAB aggregates with respect to the sample age (time) measured by dynamic light scattering measurements; the inset shows the size distributions of 4 samples as labeled in the main panel. The line joining the data is only to guide the eye. Each mixture was diluted with 5.5 mM DTAB solution to reduce multiple scattering, a procedure that did not change the physical state of the aggregates.

To prevent further aggregation and precipitation of the formed NaPSS/DTAB aggregates, the freshly prepared P/S mixtures were used within one minute after mixing.

The possibility of forming loaded NaPSS/DTAB membranes by exploiting the Marangoni spreading and the dissociation of the neutral aggregates was investigated by dynamic ellipsometry measurements at the static air/water interface of liquid contained in a 7-cm diameter Petri dish made of glass. The total volume of the subphase was 25 ml. 100 µl of the freshly mixed P/S mixtures were dispensed onto the interface, drop by drop, with a micropipette. To prevent the droplets falling from a height, the pipette was kept at an angle of 45°, the droplets were collected at the tip of the pipette and spread by letting them gently touch the surface. In figure 23, the time-resolved surface excess of NaPSS/DTAB spread films from neutral aggregate mixtures (A) is compared with that of adsorbed layers formed by bulk adsorption of the pre-diluted components (B) mixed using the 1:1 v/v standard mixing approach developed previously.[113] The final bulk concentrations were identical for the two different methods. In this case, to avoid significant errors that would be introduced through modelling the ellipsometry data, using the approach described in chapter 2.2.4, due to anisotropy in the dielectric profile normal to the interface, the dynamic phase shift measured by ellipsometry was scaled to the a direct measurement of the surface excess measured by NR; see later in figure 24. To emphasize the role of aggregate dissociation, spread films and adsorbed layers were also prepared in absence of aggregates, either by spreading small aliquots NaPSS/DTAB mixtures at a composition of 100 ppm NaPSS and 0.4

mM DTAB (C) or by adsorption from solutions of the pre-diluted components, so that the final bulk concentrations are again matched (D, 0.4 ppm NaPSS and 1.3 µM DTAB). To highlight the importance of the polyelectrolyte, the average surface excess of three independent measurements after spreading 100 µl of 6.0 mM DTAB solutions in absence of NaPSS (E) is reported as well.

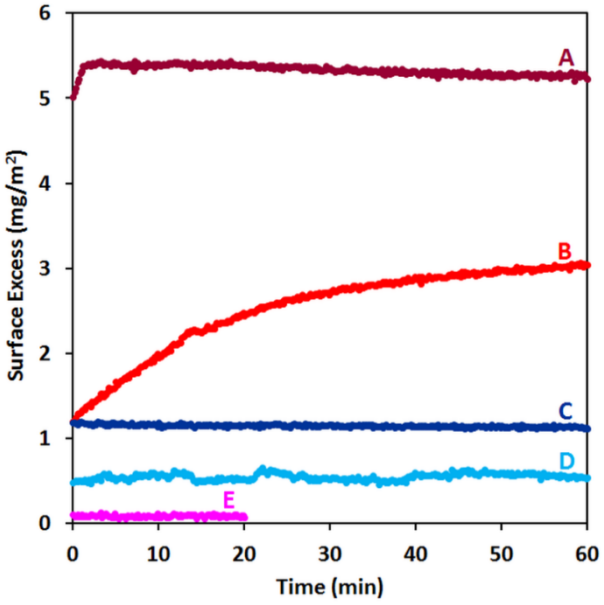

Figure 23 - Ellipsometry measurements of the total surface excess of NaPSS and DTAB. The values are scaled to that of sample A measured directly using NR. Samples A and C are spread films while samples B and D are the respective adsorbed layers with equivalent amounts of the components; the spread films were prepared using 100 µL aliquots of 100 ppm, 17-kDa NaPSS with (A) 6 mM and (C) 0.4 mM DTAB dispensed on 25 mL of pure water in a static trough; sample E is the average of 3 repetitions of A in the absence of NaPSS.

These data revealed some interesting points. First, a substantially higher surface excess is obtained by spreading (A and C) in a very short time than by adsorption from the bulk of the two components (B and D), which is evidence that the film formation is initiated by fast Marangoni spreading. In fact, the surface tension of the freshly mixed NaPSS/DTAB aliquots of sample A and C is roughly the same, around 44 mN/m.[93] Equilibration with the bulk is not accessible on the experimental time scale, i.e. a kinetic barrier resulting from the entropic contribution of counter-ions released in the bulk, prevents the dissolution of the film. This underlines the non-equilibrium nature of P/S films prepared by spreading since the surface excess of the equivalent adsorbed layer increases slowly and never reaches that of spread films. Further pieces of evidence are given in the next chapter, where long-time ellipsometry measurements are reported. Second, the surface excess is boosted when aggregates are present in the spreading aliquot. Indeed, the initial surface excess of sample A is 4–5 times higher than that of sample C. This difference cannot be attributed to the additional surfactant in sample A (6 mM) compared to sample C (0.4 mM), as the surface excess of a film spread

from 6 mM DTAB solution, like in sample A but in the absence of polyelectrolyte (E), is minimal. Nor can it be attributed to the total concentration of polyelectrolyte since it is equivalent in both sample A and sample C. This means that the Marangoni effect of the individual components alone is not sufficient to rationalize the film formation. Instead, it must be the fast dissociation of P/S aggregates upon contact with the subphase that enhances the surface excess. As only a very small amount of materials is used to form substantial interfacial films, this process may be appealing in terms of industrial applications where very thin films of polyelectrolyte are involved. The benefits of spreading P/S mixtures could be significant as this approach is 1) quick, because film formation occurs on the sub-second time scale; 2) efficient and cost-effective, as only a very small amount of surface active material is required to form a trapped P/S film; 3) eco-sustainable, as the only solvent used in all the steps of the preparation (synthesis excluded) is water.

In a next step, the investigation of the surface properties of NaPSS/DTAB films spread from neutral aggregate mixtures was performed under dynamic conditions, both in terms of surface pressure and surface excess of the two components. For this purpose, the surface pressure vs. area isotherms were recorded during 5 consecutive compression/expansion cycles of the air/water interface, while the surface excess was derived by *in situ* NR measurements using the low-*q* analysis approach. The two sets of data are reported respectively in panels a and b of figure 24. Note that this was the first time that the method had been applied to resolve the interfacial composition of a mixture during a dynamic measurement.

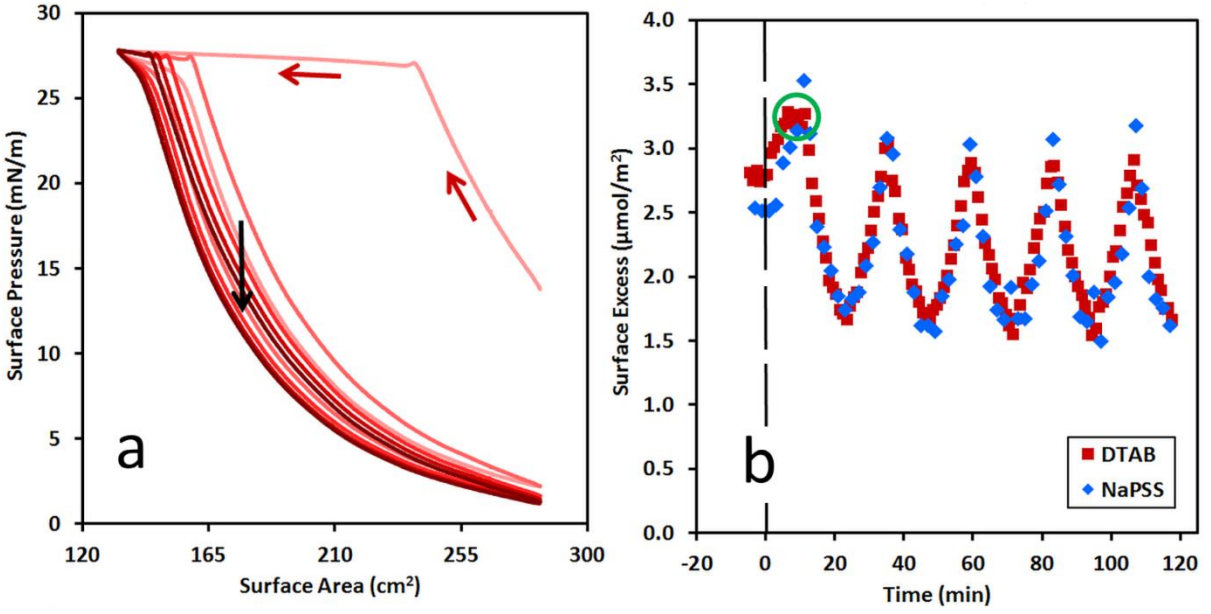

Figure 24 – a) Surface pressure vs. area isotherms of 5 compression/expansioncycles of NaPSS/DTAB films spread from neutral aggregates. The cycles are displayed progressively darker in shading. The black arrow indicates the general progression of the time, while the red arrows represent the progression of time in a cycle; b) stoichiometry of NaPSS/DTAB spread films derived *in situ*. The dashed line indicates the start of the compression. Full compression and expansion are marked respectively by maxima and minima.

The surface pressure of the films (panel a) starts at around 15 mN/m, and it increases steeply to 28 mN/m during the first cycle. It is worth noting that this surface pressure coincides with that of the spreading aliquot,[93] which is far more concentrated (250 times) than the final total bulk concentration of the systems with the spread films. During the compression, as expected, the surface excess of both surfactant and polyelectrolyte increases. Eventually, the two values reach a limit, and the onset of the plateau coincides with that of the surface pressure (indicated by the green circle in panel b). Upon expansion, high hysteresis is observed only during the first cycle, after which the system relaxes to lower surface pressures than that at the start of the first compression. Thanks to the application of NR, this feature can be attributed to the squeezing out of material during the first compression. In fact, the positions of the following maxima of the surface excesses also shift to lower values than the first, indicating that some material was lost to the bulk. For the consecutive cycles, a limiting behavior was reached and the film behaved like perfectly insoluble monolayer. This was the first time that the surface excess of an organic mixture was resolved *in situ* during a Langmuir experiment.

The loss of material that occurred upon compression was also observed in real space by performing BAM imaging of the air/water interface under dynamic conditions (figure 25). The background was subtracted and automatic focusing was disabled, due to the highly dynamic nature of the interface. The same gamma-correction was applied to all the images in order to emphasize the morphological feature.

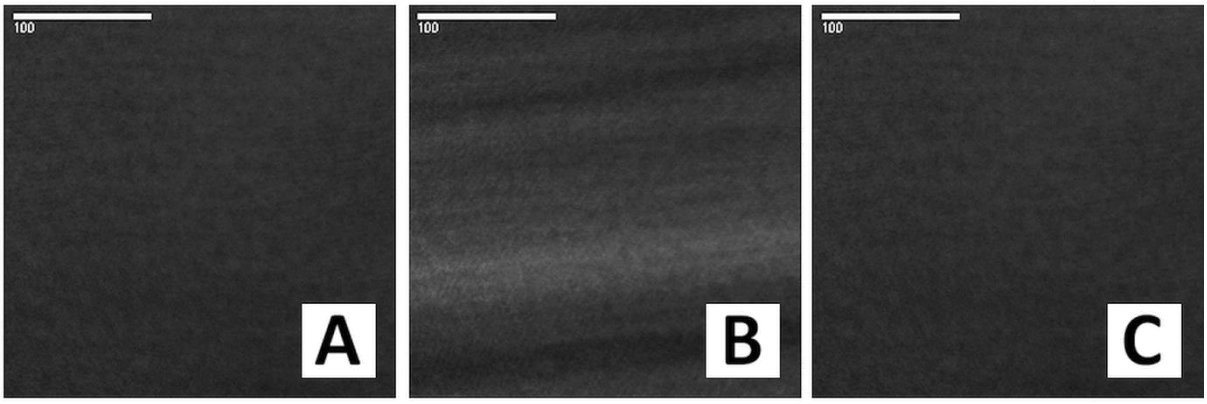

Figure 25 - BAM images of NaPSS/DTAB films spread from neutral aggregates during the compression at surface areas of (A) 260 cm^2, (B) 160 cm^2 and (C) upon expansion at a surface area of 210 cm^2. The scale bars are 100 micrometers.

These images show that a change in the morphology of the film occurs when the material is squeezed out from the interface. At low compression ratio (A), no lateral inhomogeneity are displayed and the intensity of the reflected beam is constant (grey in this image). When the interface is fully compressed (B), linear ripples with increasing intensity (light-grey bands)

appear, which are alternated to dark bands. During this phase, the monolayer buckles and material is lost to the bulk of the aqueous subphase. These ripples disappear during the expansion, as the surface pressure relaxes, and an optically homogenous film is left (C).

These data from the applied techniques together show that non-equilibrium P/S films can be easily formed by exploiting the Marangoni spreading and aggregate dissociation of highly surface active NaPSS/DTAB mixtures, upon contact with the air/water interface. The presence of aggregates in the spreading aliquot is crucial, as their dynamic dissociation upon contact with the interface is needed to boost the surface excess of both components. In particular, it is important noting that, in this system, more than one-third of the polyelectrolyte present in the spreading aliquot has been confined to the interface, and this is a surprising result because of two reasons. The first is because the polyelectrolyte alone is not surface active and it is only encapsulated in liquid crystalline aggregates, the dissociation of which at the interface allows it to become trapped. The second, and more relevant reason, is that these experiments proved that non-equilibrium effects play a major role in the determination of the surface properties of P/S mixtures even in very dilute conditions, depending on the sample handling. Lastly, films spread from NaPSS/DTAB neutral aggregates are trapped in a metastable state, which can persist for a very long time after spreading, and the films are durable and stable even when the surface is mechanically perturbed. Even so, to develop this methodology for technological applications, further work on different systems with respect to a range of variable was clearly required. The results described in this chapter were published in 2016,[102] and the work paved the way for an investigation on the effects of the aggregate charge/structure on the physical properties of PSS/DTAB.

3.3 Effects of aggregate charge/structure on the properties of NaPSS/DTAB films at the air/water interface under static and dynamic conditions.

The effects of the aggregate charge/structure on the formation and the properties of NaPSS/DTAB spread films are the center of attention in this chapter. This work allows the establishment of a relation between the bulk phase behavior of oppositely-charged P/S mixtures and the resulting spread films at the bare air/water interface. Aggregates with different charge/structure were prepared by rapidly mixing equal volumes of 200 ppm NaPSS stock solution and DTAB solution over a broad range of concentrations, i.e. by keeping the concentration of the polyelectrolyte fixed, while varying the amount of surfactant. The protocols used for the production of the spread films and corresponding adsorbed layers were the same as those described in chapter 2.1.2 and used in the investigation of films spread from neutral NaPSS/DTAB aggregates in chapter 3.2.

The surfactant concentration range was chosen in such a way to explore the whole spectrum of bulk phase behavior of NaPSS/DTAB mixtures. Each bulk DTAB concentration was selected in order to be representative of a different physical state of the 100 ppm NaPSS/DTAB system. For this purpose, time-dependent $O.D_{400}$ measurements as well as electrophoretic mobility data were used. These experiments were performed by varying the concentration of surfactant in the spreading aliquots over the range 0.4–25 mM. The optical density data are reported in figure 26 for the freshly mixed NaPSS/DTAB mixtures as well as for the 1-month settled samples. In the latter case, the optical density measurements were performed on the supernatant. The latter data are quite useful to identify the regions in the phase diagram where kinetically-trapped aggregates are present. The range of concentrations in which precipitation occurs, i.e. the equilibrium two-phase region, is shaded in yellow. The point of charge neutrality is marked by a vertical dashed line. Note that the electrophoretic mobility data for the 100 ppm NaPSS/DTAB mixtures have been shown previously in figure 21.

Close to charge neutrality (samples D, E, F in figure 26), the optical density of freshly mixed NaPSS/DTAB mixtures is high due to the formation of macroscopic P/S aggregates in which many complexes are stuck together due to a lack of charge at their surface, and hence lack of electrostatic stabilization. The colloidal stability of the aggregates is compromised and the system evolves toward the equilibrium two-phase regime (phase separation). When these samples are left to settle for one month, the optical density of the supernatant decreases drastically until the precipitate is fully settled (yellow area in figure 26). The optical density

of freshly mixed samples decreases either at lower or higher bulk surfactant concentrations than the boundaries of the yellow area, i.e. away from the equilibrium two-phase region. In these regions, the species formed upon mixing have colloidal stability thanks to the excess of either polyelectrolyte segments, on the left of the equilibrium two-phase region (negatively charged), or the excess of surfactant (right side, positively charged), which inhibits aggregation. Consequently, the turbidity of the P/S mixtures is decreased. However, one month after mixing, the turbidity of NaPSS/DTAB mixtures prepared in this range of compositions, is still quite high due to the slow coagulation rate of these samples, which is directly connected to the electrostatic stability of the aggregates, provided by the excess of either of polyelectrolyte segments or surfactant molecules (sample B, C and G, H).

At very low concentrations of surfactant (sample A), the turbidity is minimal, indicating that only individual molecular complexes of micelle-like surfactant architectures wrapped by individual polyelectrolyte chains are formed in this region. These structures are in equilibrium with the free surfactant molecules in solution, therefore here the NaPSS/DTAB mixtures are equilibrium one-phase systems.

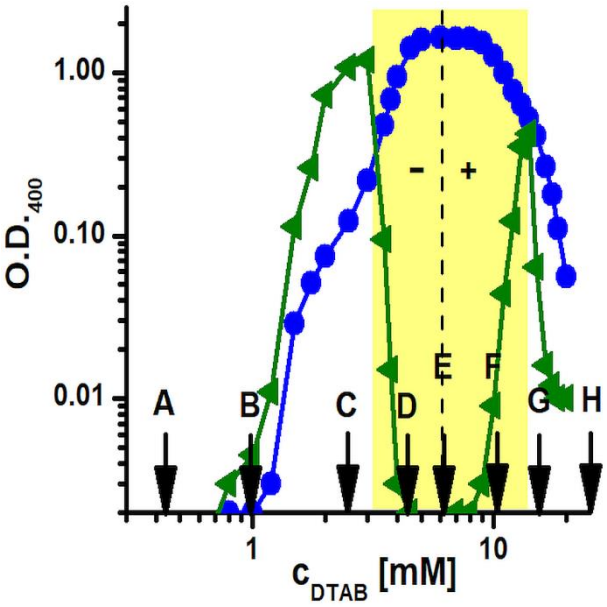

Figure 26 – O.D.$_{400}$ of 100 ppm, 17 kDa NaPSS/DTAB mixtures vs. the total DTAB concentration for freshly mixed samples (blue circles) and aged for one month (green triangles). The equilibrium two-phase region is shaded in yellow. The vertical dashed line identifies the bulk composition of charge neutrality. The letters A to H correspond to the bulk compositions of mixtures used to form spread films.

This investigation showed that for the 100 ppm 17 kDa NaPSS/DTAB mixtures, aggregates are produced over a broad range of surfactant concentration. By combining this information with the generally accepted physical picture about the bulk phase behavior of P/S systems,[79,90-92] it was possible to select eight bulk compositions for preparing spread

NaPSS/DTAB films at the air/water interface, so that each sample was representative of a different physical state of the particular P/S system.

In order to minimize the size of the aggregates formed, each spreading aliquot was used within one minute after mixing, as in the previous investigation on the properties of NaPSS/DTAB spread films from neutral aggregates the sizes of the aggregates were found to be approximately 500 ± 50 nm (figure 22). Here, it was assumed that the sizes of charged aggregates are smaller because of slower or inhibited aggregation. It is important to bear in mind that both the charge and the structure of the aggregates change as the surfactant concentration is varied. Therefore, it is not possible to distinguish between the two effects and, for this reason, the terminology "charge/structure" is adopted. A summary of the physical characteristics of the eight samples in figure 26 (labeled A–H) is shown in table 2.

Table 2. Summary of the physical characteristics of eight different bulk compositions of NaPSS/DTAB mixtures.

Label	[DTAB] / mM	Characteristics
A	0.43	Equilibrium one-phase region; negligible amount of aggregates; moderate in size; swollen in structure; high negative charge.
B	1.0	Equilibrium one-phase region; small amount of aggregates; moderate in size; swollen in structure; high negative charge.
C	2.5	Equilibrium one-phase region; moderate amount of aggregates; moderate in size; swollen in structure; high negative charge.
D	4.5	Equilibrium two-phase region; large amount of aggregates that lack colloidal stability; becoming larger in size; becoming more compact in structure; low negative charge.
E	6.0	Equilibrium two-phase region; large amount of aggregates that lack colloidal stability; largest in size; compact in structure; charge neutral.
F	10	Equilibrium two-phase region; large amount of aggregates that lack colloidal stability; becoming smaller in size; compact in structure; low positive charge.
G	15	Colloidal aggregate dispersion; large amount of stabilized aggregates; moderate in size; compact in structure; positive charge.
H	25	Colloidal aggregate dispersion; large amount of stabilized aggregates; smallest in size; compact in structure; high positive charge.

Next, the effects of the aggregate charge/structure on film formation as well as the resulting physical properties of NaPSS/DTAB spread films were investigated under static conditions by the means of dynamic ellipsometry measurements. Hereon, the variation of the phase shift with respect to the bare interface is shown instead of the surface excess. The latter quantity can be calculated accurately for homogenous layers. Any inhomogeneity present in the layer

could lead to an erroneous interpretation, even for a single component system.[128,129] Alternatively, one can rely on the calibration of the ellipsometry data with other techniques, as it has been done in chapter 3.2 of this thesis. However, here the investigation is carried out as a function of several experimental variables, namely the bulk surfactant concentration (charge/structure of the aggregates), the sample history and the sample age. Furthermore, the effects of each of them on the dielectric function in the normal direction to the interface are unknown *a priori*. This imposes a limitation on the use of a calibration curve for attaining surface excess in a reliable way. Moreover, the partial coverage of the surface and/or the presence of embedded aggregates in the spread films can affect the measured values either positively or negatively. For all of these reasons, it is preferred to report only the variation of the phase shift, as it still carries information about the relative surface excess anyway. The variations of the phase shift with respect to the bare interface are displayed in figure 27, for both spread films (panel a) and adsorbed layers from solutions with equivalent total final bulk concentrations of the two components, each one pre-diluted separately before mixing (panel b). Data from samples with the same final bulk concentrations, but different sample handlings are displayed with matching colors. Each mixture used for spreading was prepared by rapidly mixing the same volumes of 200 ppm NaPSS stock solution with DTAB solutions at concentrations equal to double of that in figure 26, from A to H. After, a 100 µl aliquot of each freshly mixed P/S mixture was dispensed by dropwise addition onto each bare air/water interface. The ellipsometry measurements were started immediately after spreading.

From the data in figure 27, several observations can be made. First, it is demonstrated that over the whole composition range investigated, films with enhanced surface excess are formed by spreading rather than by adsorption from the bulk of solutions of the two pre-diluted components. In particular, the relative initial surface excess of spread films is 5 to 20 times higher than that of the corresponding adsorbed layers (small inset in panel b of figure 27). Second, it is shown that the surface excess is boosted further when a large number of aggregates are present in the spreading aliquot (sample C to H). It is interesting to note that the relative surface excess is equivalent to that of the interface of a 250-fold concentrated NaPSS/DTAB mixture in the one-phase region, i.e. at the same composition of the aliquot of sample A, represented as a dashed line in the inset of figure 27 a. This value was taken as a reference for a saturated equilibrium adsorbed NaPSS/DTAB layer.

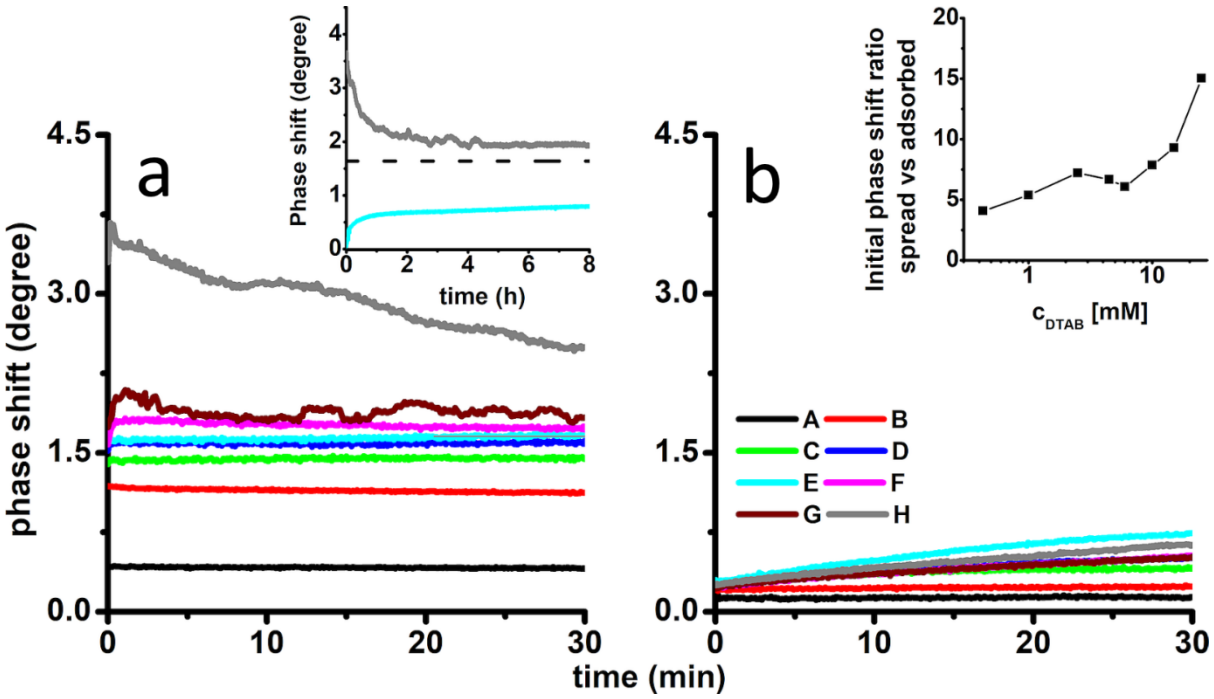

Figure 27 Variation of the phase shift of (a) spread films and (b) adsorbed layers of NaPSS/DTAB on pure water. Longer measurement of the spread film of sample H (grey) and the adsorbed layer of sample E (pale blue) are shown in the small inset to panel a. The reference for the saturated layer is indicated by a dashed line. The inset to panel b contains the ratio of the initial phase shifts of the spread films to the corresponding adsorbed layers.

It may be noted that most of the data in figure 27 b have not reached equilibrium during the 30-minute measurements. For this purpose, the phase shift of the corresponding adsorbed layer of sample E was monitored for 8 hours (light blue curve) and compared to the reference for a saturated layer (dashed line), in the small inset in figure 27 a. This proved that the exploitation of the quick dissociation of aggregates upon contact with interface, in combination with the fast Marangoni spreading, is not simply a very fast and efficient way of producing P/S films with enhanced surface excess at the air/water interface, but it also results in kinetically-trapped films, which are very stable over time.

Through a closer look at the data presented in figure 27, some differences in the signals of films spread from negatively charged/swollen aggregates (sample D) and those of films spread from positively charged/compact aggregates (sample F to H) can be spotted. Specifically, the ellipsometric signals up to sample D were stable in time, while those of sample F to H exhibit temporal fluctuations, which become more and more marked as the charge of the aggregates increases. Such fluctuations may be attributed to large domains of extended structures at the air/water interface, such as multilayer P/S stacking or reservoirs of surface active material, or possibly to intact aggregates embedded in the surface film. Due to the highly mobile nature of the interface, such extended structures would be detected only when they pass through the region of the interface sampled by the laser spot (a few mm^2) and

by passing in and out of this area, they would cause the temporal fluctuations of the ellipsometric signal as it has been observed previously for different P/S systems.[92,113] It can be noted as well that the general trend of the signals of samples F to H indicates a constant decrease in time, which is more marked in sample H. This behavior can be attributed to a continual loss of material from the interface to the bulk, until a more stable state is reached. In order to investigate the kinetics of relaxation of the surface excess, 8-hour ellipsometry measurements of sample H were performed. This sample was chosen as it did not relax fully over 30-minute measurements. These data are represented by the grey line in the small inset of figure 27 a. A stable signal is attained almost five hours after spreading, with the phase shift decreasing continually and with visible fluctuations until then. Surprisingly, the variation of the phase shifts of films spread from highly positive charged/compact aggregates exceeds that of an equilibrium saturated layer (dashed line in the same inset), indicating that, effectively, the surface excess can be boosted even more when positively charged/compact aggregates are present in the spreading aliquot, or that aggregates embedded in the films contribute to the signal.

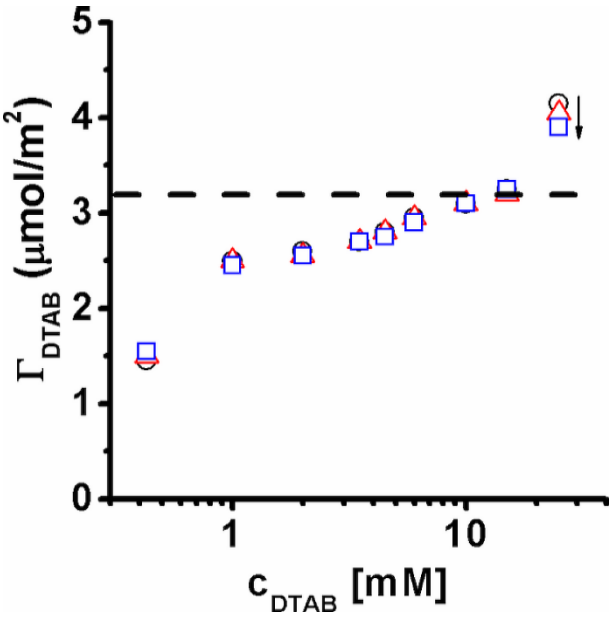

Figure 28 - Surface excess of DTAB in spread films prepared from NaPSS/DTAB mixtures on pure ACMW measured using NR for three different surface ages: 6 min (open black circles), 8 min (open red triangles), and 10 min (open blue squares). The monolayer coverage is represented by the horizontal dashed line. The small black arrow indicates the general flow of time.

Lastly, the accurate quantification of the DTAB surface excess was attained by kinetic NR measurements, which are displayed in figure 28 for three different surface ages. These samples were measured on FIGARO using a larger Langmuir trough which contained 125 ml of subphase, in this case ACMW to tune the isotopic contrast to the needs of the experiment.

Therefore, the spreading aliquots were rescaled by volume up to 500 μl in order to keep constant the final bulk concentrations.

To resolve the composition of the spread films, only two contrasts, i.e. hydrogenous polyelectrolyte + deuterated surfactant in ACMW (h-NaPSS and d-DTAB) and hydrogenous NaPSS + contrast matched surfactant (h-NaPSS and cm-DTAB) in ACMW were needed. The contribution to the scattering of the first contrast comes from both components, while it depends only on the h-NaPSS content since the cm-DTAB as well as the ACMW are made invisible to neutrons. Due to the higher scattering of the first contrast than that of the second, one-minute kinetics scans were sufficient to collect quantitative data on the surfactant, while two-minute scans were needed to resolve the polyelectrolyte contribution. The surface excess of the surfactant was derived by solving simultaneously Eqs. 43 and 44.

NR data are in good agreement with those attained from ellipsometry and besides providing a direct measurement of the surface excess of the surfactant, they carry two important confirmations. The first is that the monolayer coverage is exceeded only when compact aggregates with high positive charge are spread. Second, the material is lost from the interface with time. The surface excess of the surfactant decreases continually, as indicated by the black arrow in figure 28. Furthermore, these data are evidence that film formation is optimal when a large number of aggregates are present in the spreading aliquots.

In order to investigate further the influence of the charge/structure of the aggregates on the properties of spread P/S films, and to see if there are other differences in terms of aggregates spreading and dissociation, 5 stepwise additions, each one of 100 μl and equally spaced in time of 5 minutes, were performed for spread films from aggregates with different charge/structure, specifically samples D, F, G and H. The investigation was carried out once more at the static air/water interface by the means of dynamic ellipsometry measurements. The data are shown in figure 29. The value of the phase shift of the bare interface is zero.

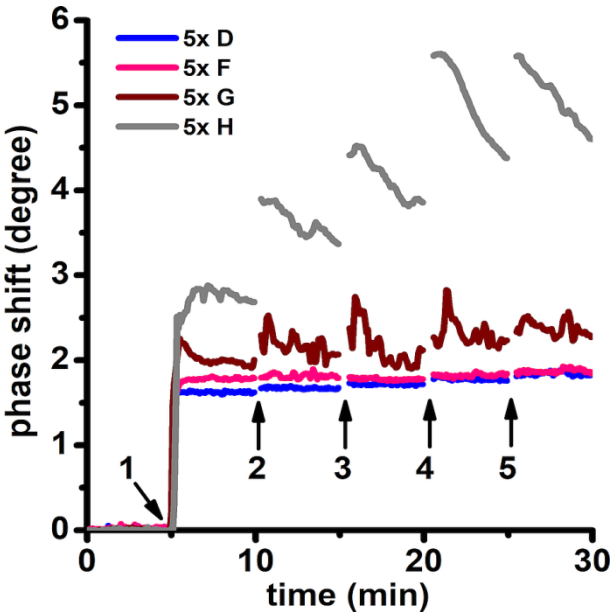

Figure 29 - Ellipsometric phase shift of five additions of aliquots containing aqueous aggregates with different charge/structure on pure water. Each addition is marked with an arrow and a number.

This experiment showed that 5 additions of P/S aliquots containing aggregates with either low negative charge (sample D) or low positive charge (F) do not cause a significant increase of the ellipsometric signal, which always remains close to the reference value for a saturated monolayer. The situation changes dramatically when compact aggregates with high positive charge are used (samples G and H). The successive additions of these mixtures cause the successive loading of the interface with big fluctuations of the ellipsometric signals. It may be inferred that small compact aggregates with high positive charge embedded in the monolayer trigger the formation of extended structures of surface active material.

To see if it was possible to visualize these extended structures in the real space, BAM images of sample H were recorded for 5 different surface ages (figure 30).

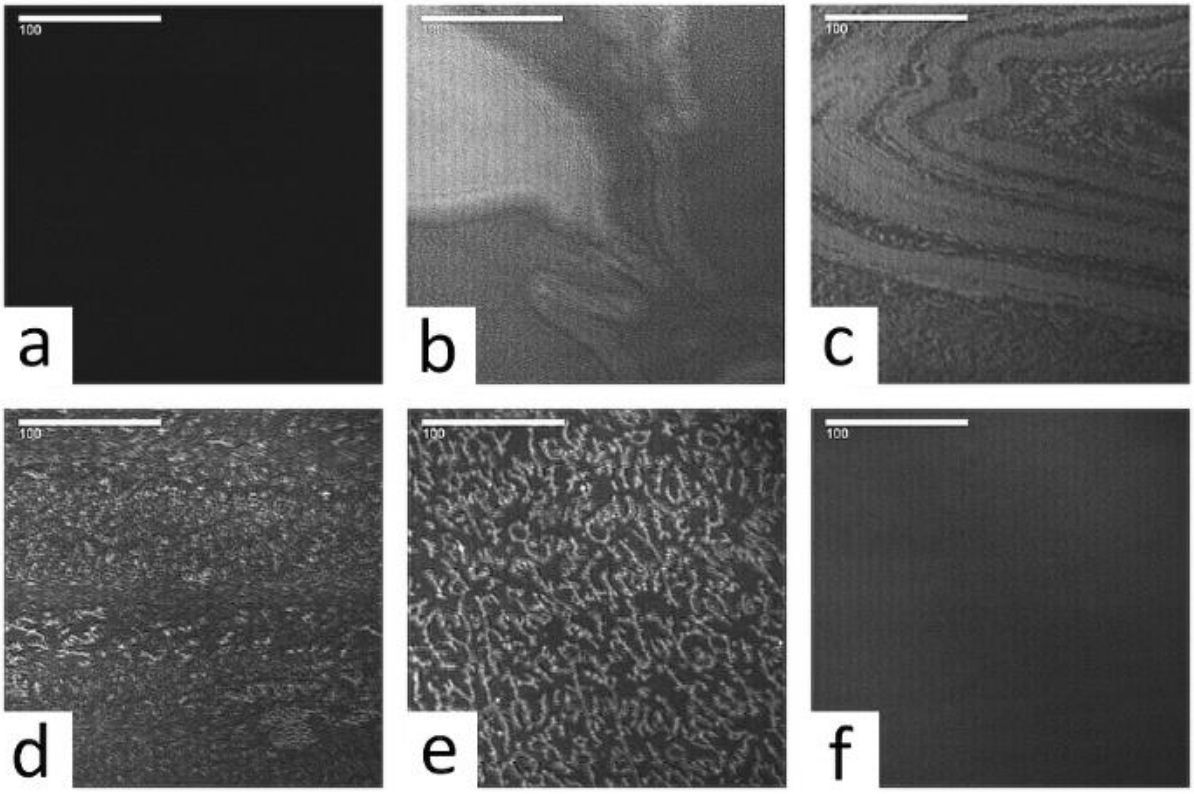

Figure 30 - BAM images of (a) a bare air water/interface, and (b–f) a spread film prepared by spreading a 100 μL of sample H. The sample ages for the films are (b) 5 min, (c) 15 min, (d) 1 h, (e) 2 h and (f) 15 h. The scale bars are 100 μm.

These experiments were carried out by using only the p-component of the polarized laser beam. In this way, background subtraction was not needed. Moreover, since the bare interface does not reflect this component, an optically homogeneous layer will be visible through the variation of the signal intensity. The bare interface is shown in panel a as reference. Immediately after spreading, the intensity of the reflected beam was too high to visualize any inhomogeneity. Five minutes later (panel b), bright domains with round contours start appearing. These domains are surrounded by an optically homogenous P/S layer, visible in grey in the images. The high brightness of these domains indicates that those regions contain more material than the gaps. The round shapes can be attributed to the nature of the spreading process. The material is spread radially by Marangoni flow from the location where the droplets touch the subphase. As the addition proceeds drop by drop, the process creates consecutive waves of material that result in the irregular round shape of the domains of extended structures. As time passes and the material is lost from the interface to the bulk, the intensity of the reflection decreases and the shapes of the domains vary. In particular, smaller worm-like domains start to appear after 15 minutes (panel c), and a few hours later (panel d and e) the round domains are not visible anymore. A homogeneous layer, within the micrometer resolution of the technique, is formed 15 hours after spreading (panel f). It is

worth pointing out that similar extended structures in P/S systems had already been observed in concentrated mixtures of carboxymethyl-cellulose with cationic surfactants.[146] However, the study presented in this thesis demonstrates that extended structures can persist even in very dilute conditions, depending on the sample history.

In chapter 3.2, the mechanical properties of NaPSS/DTAB spread films from neutral aggregates were investigated and it was found that they behave as perfectly insoluble membranes, despite the high solubility of the two components in aqueous media at the same low final bulk concentrations. What remained to investigate were the effects that the aggregate charge/structure would have and if the formation of extended structures can be induced by compressing the interface. Thus, 5 consecutive compression/expansion cycles of the interface were performed for films spread from sample D and F. It is worth remembering that these two samples represent two different aggregation states, negatively charged/swollen and positively charged/compact aggregates, respectively. Sample F was chosen over sample G and sample H as its phase shift was almost stable after spreading at the static air/water interface on experimentally accessible time scales. In addition, small fluctuations of the signal were detected when 5 consecutive aliquots were spread at the interface, indicating that extended structures are formed also for this sample. During the 5 cycles of the interface, the surface pressure was monitored continuously and the surface excess of the two components was derived from *in situ* NR kinetic scans, thanks to the low-q analysis approach. The data are shown in figure 31. Maxima and minima in the surface excess (panel a and panel c) mark full compression and full expansion, respectively, of the samples spread from negatively charged aggregates (sample D, panel a) and positively charged aggregates (sample F, panel c). Surface pressure data and the DTAB surface excess during the first compression are plotted together in panels b and d. The small insets to panels a and c contain the surface pressure data of the whole 5 cycles.

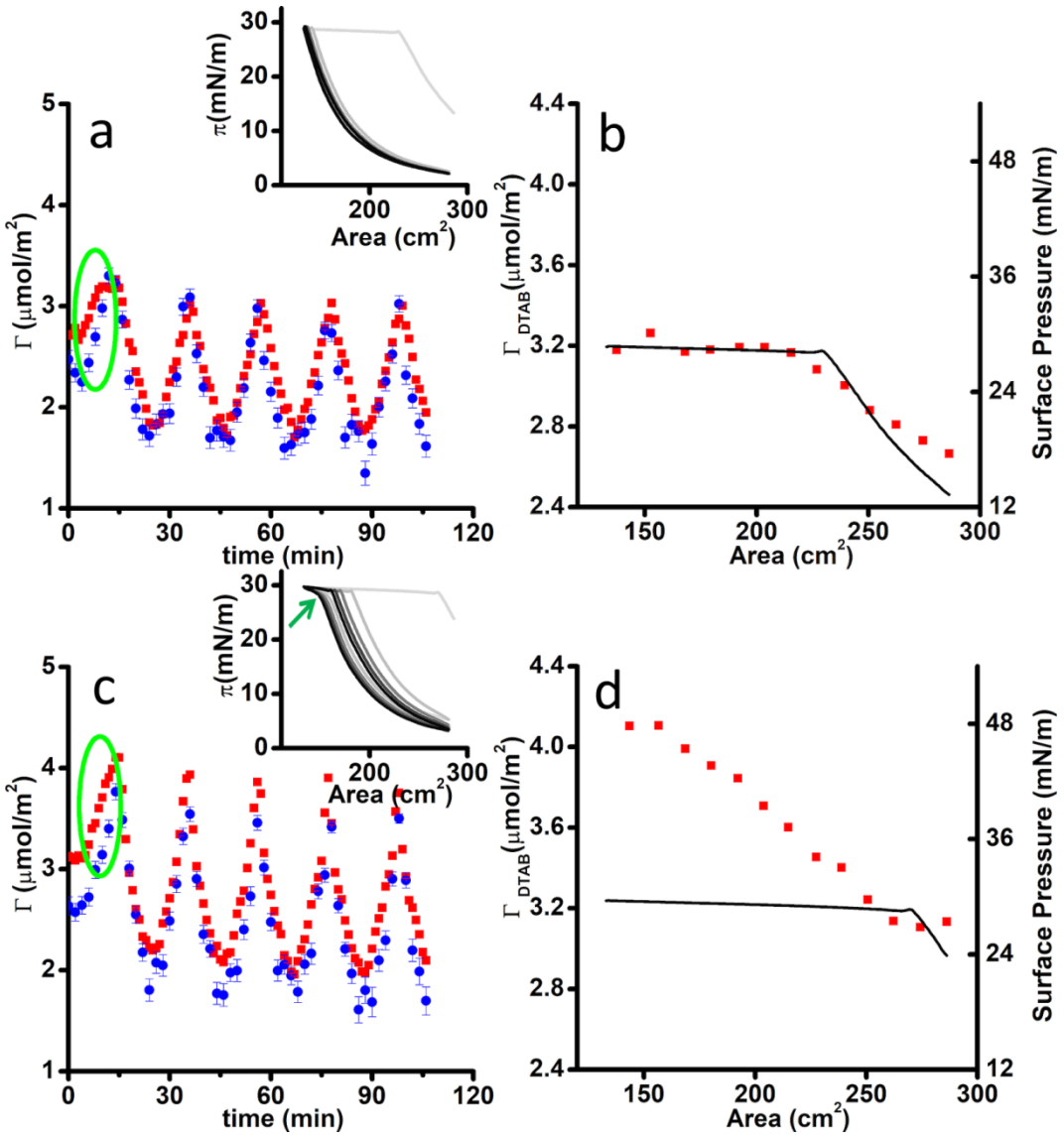

Figure 31 - Surface excesses of NaPSS (blue circles) and DTAB (red squares) during 5 compression/expansion cycles of a film spread on ACMW from aggregates of (a) sample D and (c) sample F. The surface pressure data are shown in the insets. The surfactant surface excess (red squares) and surface pressure (black line) during the first compression are shown in panel b and d, respectively.

The surface pressure behavior of films spread from negatively charged/swollen aggregates (sample D) is very similar to that of spread films from neutral aggregates (chapter 3.2) with the surface pressure reaching its plateau value at around 29 mN/m as well as a plateau in surface excess at around 3.2 μmol/m^2 (figure 31 b). These data are consistent with the presence of a monolayer of surfactant molecules bound to polyelectrolyte segments in a 1:1 molar ratio. Another common feature of figure 31 a and the data attained for spread films of neutral aggregates is that the excess of material is squeezed out during the first compression, and consequently the maxima in the surface excess plot are shifted to lower values. Upon expansion, both surface pressure and surface excess relax to a lower value than those

achieved upon compression. From the second cycle, a limiting behavior is reached and the films behave like an insoluble monolayer.

Films spread from positively charged/compact aggregates (sample F) behave in a different way, both in terms of their surface mechanical properties and surface excess. During the compression of the interface, they also reach a plateau in surface pressure at around 29 mN/m, but this time the surface excess keeps increasing even when the surface pressure has leveled off at its plateau value (figure 31 d). Moreover, the surface excess values of these films, immediately after spreading, are comparable to that of sample D at full compression, indicating that more material is delivered at the interface when positively charged/compact aggregates are used for the film preparation. These features can be explained in terms of the formation of extended structures of both components, in contrast to the formation of polyelectrolyte loops beneath a surfactant layer, which is unfavorable because of the low ionic strength of the system. Upon expansion, a significant delay in the relaxation of the surface pressure is observed (green arrow in the small inset to panel c). This hysteresis can be attributed to the fast resupply of surface active material from the extended structures, which in this sense behave as reservoirs of material. Over the remaining cycles, only a minimal decrease in surface excess is observed, while the hysteresis upon expansion persists, indicating that the formation of the extended structures continually occurs during the successive compressions of the interface. The stoichiometry of the interface is consistent with the one-to-one molar charge ratio, as observed for film spread from negatively charged and neutral aggregates. However, a small deviation from this ratio is observed at full expansion. It may be inferred here that this deviation is caused by the presence of embedded aggregates with high surfactant content in the surface layer.

Once more, the formation of the extended structures was observed in real space by the means of BAM. These images are shown in figure 32 for six different surface areas, upon compression. The investigation was carried out on spread films from sample F. In this case higher compression of the surface, i.e. lower value of the total surface, was achieved by using a longer Langmuir trough.

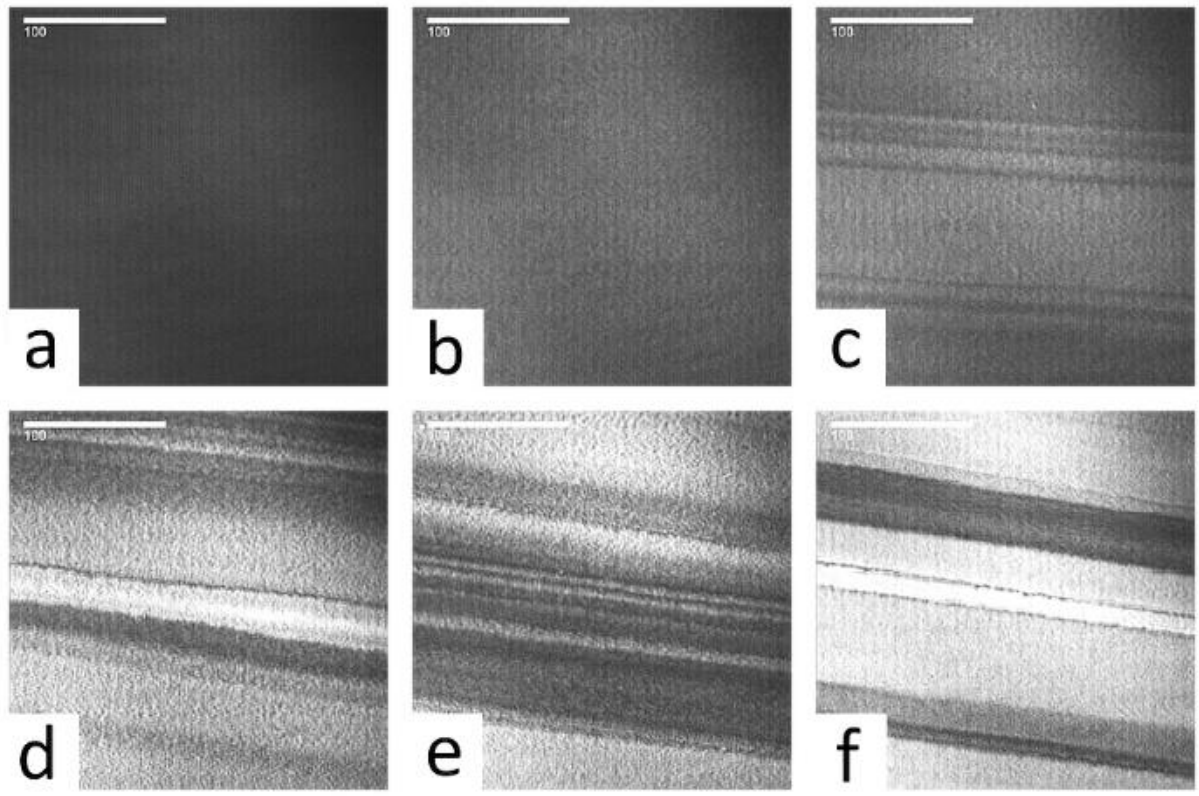

Figure 32 - Brewster angle microscopy images of a NaPSS/DTAB film spread from aggregates of sample F with surface areas of: (a) 700 cm^2, (b) 400 cm^2, (c) 250 cm^2, (d) 180 cm^2, (e) 100 cm^2 and (f) 85 cm^2.

The BAM images show that a homogeneous layer is formed upon spreading, or at least no optical inhomogeneity was detected in the surface layer immediately after spreading (a). However, the intensity of the reflected beam was higher than that of the bare interface, consistent with the presence of a homogenous monolayer. Upon compression, the intensity of the reflection increases in a consistent way with the formation of a denser layer (b). The extended structures start to be visible as alternate bright and dark bands, perpendicular to the direction of compression, at values of the surface area between that of panel b and c, which is close to the compression ratio used in the NR experiments. Further compression resulted in a higher intensity of the reflected beam from the extended structures (c to f). Similar morphologies have been reported already for multilayer and/or extended structure formation in different systems at the air/water interface.[147,148] Since the composition of both components in films spread from aggregates with different charge/structure under dynamic conditions are similar to some extent, and the total bulk concentrations of the systems are highly dilute (250-fold), it is reasonable inferring that the formation of extended structures, in which the amount of the two components exceeds that of a full monolayer, is activated only when compact/positively charged aggregates are embedded in the surface films.

To summarize, in this chapter the investigation of film formation in spread films from NaPSS/DTAB aggregate dispersions has been extended to the effects of the aggregate charge/structure. It has been shown that spread films from NaPSS/DTAB aggregates dispersions are out of equilibrium, regardless of the charge/structure of the aggregates in the spreading aliquots. Indeed, the relative surface excess of films prepared by spreading is always above that of adsorbed layers from solutions with equivalent final bulk concentrations. However, the charge/structure of the aggregates has a strong impact on both the surface excesses of the two components as well as on the mechanical properties and lateral morphology of the resulting spread films. In particular, it has been demonstrated that the spreading of negatively charged/swollen NaPSS/DTAB aggregates results in the formation of a homogeneous monolayer at the air/water interface, whose surface excess never exceeds that of a saturated monolayer, either under static conditions by successive additions or under dynamic conditions by surface compression. The picture changes when positively charged/compact aggregates are used, as they have been shown to nucleate the formation of extended structures that ultimately act as reservoirs of surface active material, as confirmed by a range of surface sensitive techniques, performed simultaneously, under both static and dynamic conditions. Thus, it is possible to control and tune the formation of extended P/S structures from the charge/structures of the aggregates used for film preparation. Such control over the formation of extended structures was not demonstrated, until now. Lastly, it has been demonstrated that polyelectrolyte segments and surfactant molecules bind at the air/water interface in the spread films prepared on pure water in a 1:1 molar charge ratio.

These results were published along with those in chapter 3.4 in 2018,[103] and the work provided the basis for a parallel study on spread films prepared on a subphase with elevated ionic strength.

3.4 Effects of subphase ionic strength on the properties of NaPSS/DTAB films at the air/water interface under static and dynamic conditions.

In this chapter, attention is turned to an investigation of the effects of the subphase ionic strength on the properties of spread NaPSS/DTAB films. In this case, aggregate dispersions were dropped onto a 100 mM NaCl aqueous subphase. The protocols used for the preparation of the films as well as the experimental techniques used in this chapter are the same as in chapter 3.2 and 3.3, with the only difference being the ionic strength of the subphase. No inert salt was added to the NaPSS and DTAB stock solutions used to prepare the aggregate dispersions. Once more, the results are presented with respect to the sample history. This investigation was motivated by the fact that the ionic strength is a critical variable regulating the electrostatic interaction between polyelectrolyte and surfactant, both in the bulk[22,80] and at the surface of their mixtures,[94] which may ultimately allow tuning the non-equilibrium vs. equilibrium properties of spread P/S films.

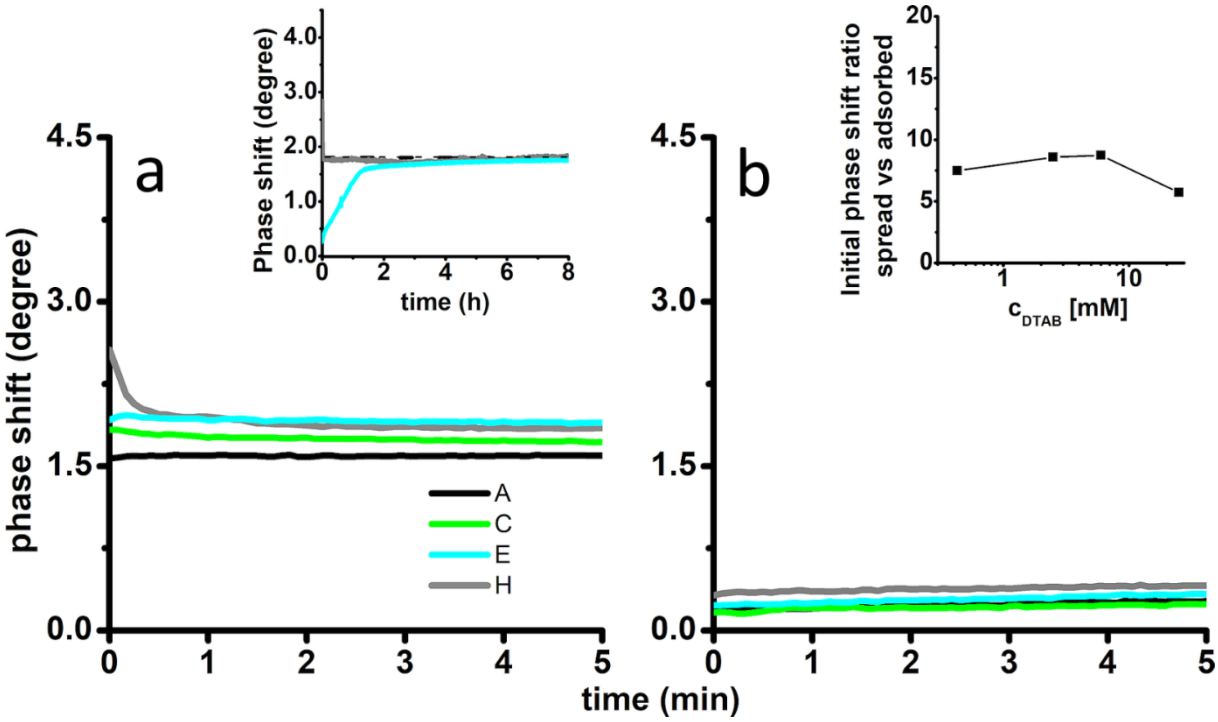

Figure 33 - Variation of the phase shift of (a) spread films and (b) adsorbed layers of NaPSS/DTAB on 100 mM NaCl aqueous. Longer measurement of the spread film of sample H (grey) and the adsorbed layer of sample E (pale blue) are shown in the small inset to panel a. The reference for the saturated layer is indicated by a dashed line. The inset to panel b contains the ratio of the initial phase shifts of the spread films to the corresponding adsorbed layers.

The variations of the phase shift for spread films prepared from NaPSS/DTAB aggregates with different charge/structure as well as that of adsorbed layers from pre-diluted solutions with equivalent final bulk concentrations are displayed with matching colors, in figure 33a and figure 33b respectively. The sample labels refer to those of figure 27 and table 2.

These data suggest that spread films all exhibit a very similar surface excess, indicating that at this high ionic strength the aggregates dissociate to produce very similar films, regardless of their charge/structure. No temporal fluctuations of the signal are observed, which is indicative of the formation of a homogenous monolayer, in which neither extended structures nor embedded aggregates are present (within the detection limits of the technique). The only exception is represented by the films spread from sample H, for which the phase shift decreases abruptly a few seconds after spreading. This behavior can be attributed to the rapid loss of material to the bulk solution. It is important to point out that the same sample H showed a smoother temporal dependency of the phase shift when prepared on pure water. In that case, it took five hours for the phase shift to become stable (see earlier in figure 27)

The relative surface excesses of the corresponding adsorbed layers (figure 33b) are minimal on a short timescale. However, longer ellipsometry measurements (inset to figure 33a) showed that, when enough time has passed, both spread films and adsorbed layers have the same amount of material, i.e. they exhibit the same phase shift, corresponding to that of a saturated NaPSS/DTAB layer in 0.1 M NaCl (dashed line in the same inset). This means that high ionic strength favors the thermodynamic equilibrium between the interface and the bulk of the system, thus the non-equilibrium features of spread films are switched off. Nevertheless, the equilibrium is still reached faster upon spreading rather than adsorption from the bulk, due to the localization of surface active material at the interface following its spreading by Marangoni flow. The ratio of the initial phase shift for the spread films, with respect to the adsorbed layers (inset to figure 33b), shows that the relative surface excess achieved by spreading is 5 to 11 times higher than upon adsorption. This represents a big potential advantage of the spreading protocol if the methodology is further developed in the future for technological applications.

Confirmation of the above description was given by the application of the low-q analysis approach for NR kinetics scans at the static air/water interface, performed on FIGARO. The data are reported in figure 34 for three different surface ages with respect to the bulk surfactant concentration in each spreading aliquot. The data analysis was carried out in the same way as described in chapter 3.3. These data show clearly that the surface excess values of DTAB in the spread films are very close to each other over a broad range of surfactant concentration in the spreading aliquots. In particular, only a small increase in surface excess is observed with increasing bulk surfactant concentration in the spreading aliquot. The resulting films are also stable over time, as the surface excess remained almost constant for

all of the three different sample ages. These measurements suggest that extended structures at the interface are absent even at the highest bulk surfactant concentration, as the DTAB surface excess is always below the saturated monolayer coverage.

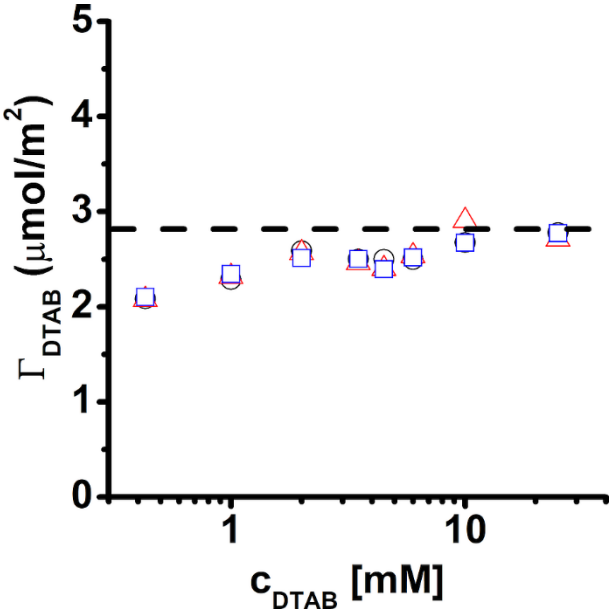

Figure 34 – Surface excess of DTAB of spread films prepared from NaPSS/DTAB mixtures on 100 mM ACMW measured using NR for three different surface ages: 6 min (open black circles), 8 min (open red triangles), and 10 min (open blue squares). The reference for the saturated monolayer is represented by the horizontal dashed line.

The last part of the investigation on NaPSS/DTAB films spread on 100 mM NaCl aqueous subphase is focused on their physical properties under dynamic conditions. Thus, the same 5 compression/expansion cycles as described above were performed in a Langmuir trough. The surface pressure was monitored continuously with a Wilhelmy plate, while *in situ* NR kinetic scans, performed on FIGARO, were used to resolve the interfacial composition for three films spread from aggregates with different charge/structure, namely negatively charged/swollen aggregates (sample D), neutral/compact aggregates (sample E), positively charged/compact aggregates (sample F). The data are shown in figure 35. The surface excesses of the two components for the films spread from sample D, E and F are respectively in panel a, panel c and panel e of the same figure. The small insets to those panels contain the respective surface pressure data, in which each cycle is shaded from light-grey to black, respectively. Plots of the DTAB surface excess (red squares) and surface pressure data (black line) with respect to the trough area, during the first compression of the interface, are shown in panel b, panel d and panel f of figure 35.

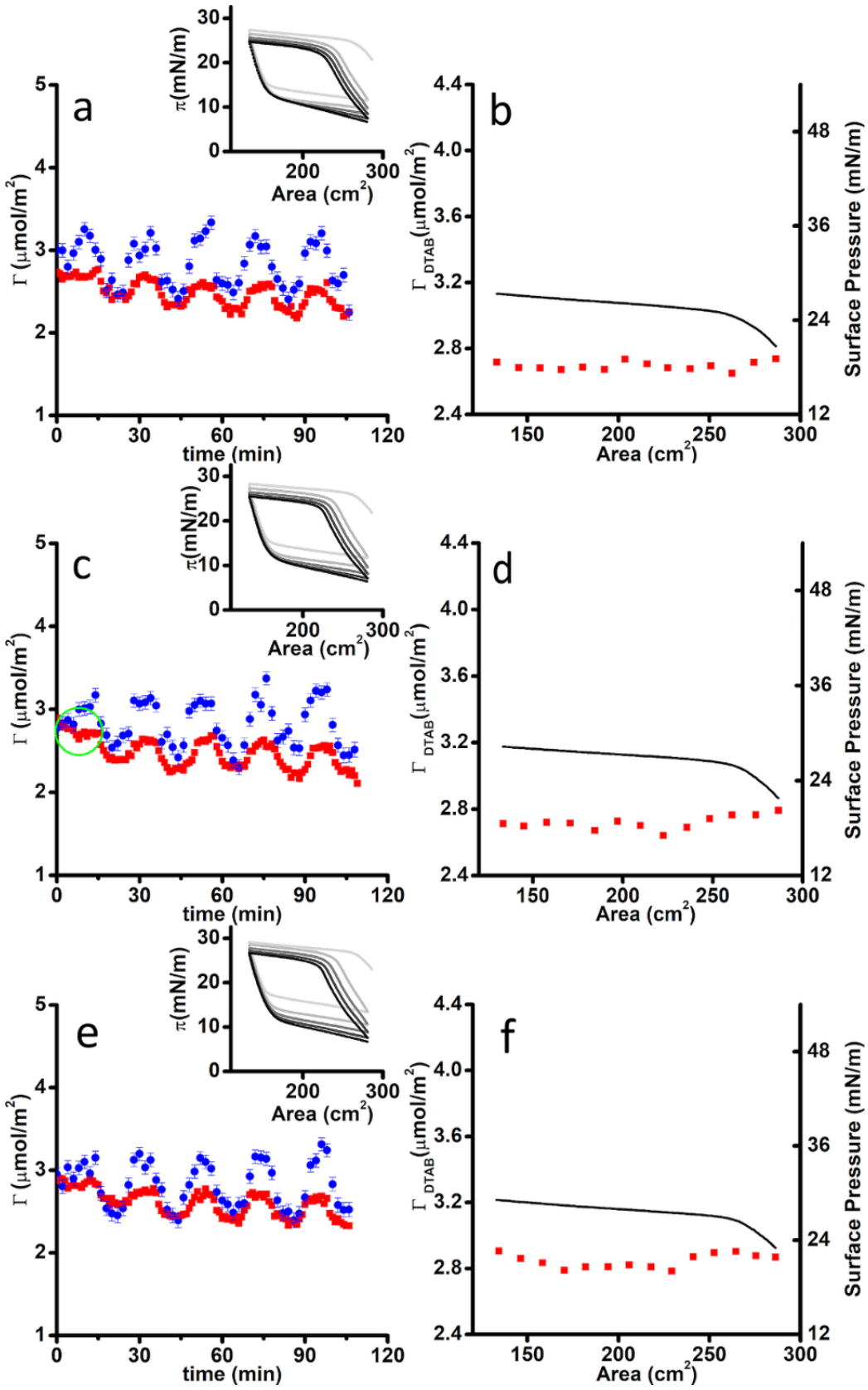

Figure 35 - Surface excesses of NaPSS (blue circles) and DTAB (red squares) during 5 compression/expansion cycles of a film spread on 100 mM NaCl ACMW from aggregates of (a) sample D, (c) sample E and (e) sample F. The surface pressure data are shown in the insets. The surfactant surface excess (red squares) and surface pressure (black line) during the first compression are shown respectively in panel b, d and f.

The similarity between the three different sets of data is striking, both in terms of mechanical properties and surface excesses of the two components. Indeed, the surface pressure plots as well as those relative to the surface excess look effectively the same regardless of the composition of the aggregates used for spreading. This is strong evidence that the high ionic strength of the subphase promotes thermodynamic equilibrium. In detail, all of the spread films reach a plateau in surface pressure around 29 mN/m already at low compression ratio of the interface and, upon further compression, the excess of surfactant is lost to the bulk of the system, as the DTAB surface excess becomes constant as well. Deviation from the 1:1 molar charge binding ratio, with a greater amount of polyelectrolyte than surfactant at the interface is also observed for the three samples, and this difference is more evident at high compression of the interface. This behavior can be explained by taking into account the formation of polyelectrolyte loops as the surface is compressed, which causes an effective increase of the density of polyelectrolyte segments at the interface, therefore an increase in the surface excess of NaPSS. In fact, at high ionic strength, the release of counterions to the bulk of the system, to which the origin of the kinetic barrier trapping the P/S layer is attributed, is less favorable. In this case, the counterions can replace the DTAB molecules in the layer, which has a twofold consequence on the properties of P/S films. On the one hand, the counterions in the surface layer act as an electrostatic shield, thus reducing the interaction between the polyelectrolyte and the surfactant molecules. On the other hand, the presence of counterions reduces the difference in osmotic pressure between the surface layer and the bulk solution and, consequently, the polyelectrolyte segments can get closer to each other and form loops. However, since also the surface excess of the polyelectrolyte also reaches a plateau, it can be concluded that some of it is lost to the bulk upon compression as well.

During the expansion, some of the material is re-adsorbed at the interface, while the surface pressure drops dramatically, indicating that although adsorption of surface active material from the subsurface region occurs, the process is diffusion-limited, causing the large hysteresis in the surface pressure between compression and expansion. In addition, this proves that extended structures of NaPSS/DTAB, acting as reservoirs of surface active material, are neither present at the interface, nor are formed upon compression. Otherwise, the same fast resupply mechanism observed in chapter 3.3 for films spread from compact and positively charged aggregates (sample F) would be expected to occur and a delay in the relaxation of the surface pressure would have been observed.

For the following cycles, the behavior does not show significant variations in the shape of both surface pressure and surface excess isotherms. Only a small decrease in the surface pressure values at full compression is observed, which is caused by the gradual loss of material, as the maxima in the DTAB surface excess shift to lower values as the experiment proceeds.

To summarize, it has been demonstrated that the subphase ionic strength is a crucial parameter in determining the physical properties of NaPSS/DTAB spread films at the air/water interface. In particular, it was shown that the high ionic strength promotes thermodynamic equilibrium between the surface and the bulk of the mixtures. Nevertheless, equilibrium is reached faster upon spreading, showing that the Marangoni spreading of P/S aggregates is still a very efficient approach for producing films containing polyelectrolytes at the air/water interface, even though the surface loading mechanism is not activated. In addition, it was shown that, due to the less favorable counterion release into the bulk of the system, formation of polyelectrolyte loops, when the surface are is compressed, is preferred to the formation of extended structures of both components under dynamic conditions. Therefore, it can be concluded that there is scope to tune the physical properties of P/S spread films, switching from the formation of reservoirs of both components to formation of polyelectrolyte loops by modifying the charge/structure of the aggregates, the subphase ionic strength, and the compression rate of the films.

These results were published along with those of chapter 3.3 in 2018,[103] and together the work laid the foundations for a comparison behavior of spread NaPSS/DTAB films with those formed from other P/S mixtures.

3.5 Comparison with other P/S systems

There are two questions that are particularly important to answer in order to generalize the spread films methodology to different P/S systems: what is the impact of the molecular architecture of the polyelectrolyte backbone on the properties of P/S spread films? Is it possible to tune equilibrium vs. non-equilibrium properties of P/S spread films by adjusting the pH of the subphase? For this purpose, in this part of the thesis, the results attained for spread NaPSS/DTAB films (chapters 3.2–3.4) are compared with films spread from neutral aggregates in two new systems, Pdadmac/SDS and hyperbranched PEI/SDS. Pdadmac is a linear strong polyelectrolyte, like NaPSS, but with the opposite charge (polycation). Pdadmac/SDS aggregates have much lower water content than NaPSS/DTAB aggregates, which makes them more compact. PEI is amphoteric, i.e. the charge density of the polyelectrolyte backbone, and consequently the binding of surfactant molecules, can be tuned by varying the pH of its solutions. The chosen surfactant was SDS for two reasons: 1) it is the most used surfactant in industry worldwide and 2) its tails are the same as those of DTAB, therefore the effects of the surfactant can be excluded from the investigation. All the attention is focused on spread films from neutral P/S aggregate mixtures. Charge neutrality was chosen as the reference because a large number of aggregates are present, and trapped films with enhanced surface excess are formed only when a lot of aggregates are present in the spreading aliquot, as it was demonstrated in chapters 3.2 and chapter 3.3. The effects of the sample history are also discussed, in order to validate the mechanism of film formation as well as to confirm the general non-equilibrium nature of P/S spread films.

It is important to bear in mind that this investigation about the physical properties of Pdadmac/SDS and PEI/SDS spread films from neutral aggregate is only at a preliminary stage. In particular, NR measurements on these systems could not be realized during this Ph.D. project because of an unexpected long shutdown of the reactor at ILL between April 2017 and March 2018. Therefore, the FIGARO instrument, which is essential to perform the low-q analysis in order to derive information about the surface stoichiometry, was unavailable during this entire period.

3.5.1 Pdadmac/SDS spread films from neutral aggregates

Mixtures of neutral Pdadmac/SDS aggregates were prepared as described in chapter 2.1.2. The composition of charge neutrality for 100 ppm Pdadmac/SDS mixtures is reached at a bulk SDS concentration of 0.82 mM.[92,149] This concentration is very close to the composition of stoichiometric charge mixing (0.62 mM), in contrast to neutral aggregates in NaPSS/DTAB mixtures, for which a large amount of free surfactant (5.5 mM) in solution is required to neutralize the aggregates formed upon mixing. To minimize the coagulation of the aggregates, as above the Pdadmac/SDS mixtures were spread one minute after mixing. Spread films and adsorbed layers were prepared as previously described, respectively by dropwise additions onto the water surface or adsorption from the bulk of P/S solutions prepared by mixing equal volumes of the pre-diluted components. The investigation has been carried out both under static and dynamic conditions, by the means of ellipsometry and surface pressure vs. area isotherms.

Static condition

The effects of the sample history (spread vs. adsorbed) and the subphase ionic strength (pure water and 0.1 M NaCl) onto the properties of Pdadmac/SDS films are compared to the case of NaPSS/DTAB spread films from neutral aggregates. An estimation of the relative surface excess is given, once more, by ellipsometry measurements. Figure 36 summarizes the results for the Pdamac/SDS spread films from neutral aggregates (panel a) and NaPSS/DTAB (panel b). The curves for spread films and adsorbed layers with the same ionic strength of the subphase are displayed with matching colors. It is important to bear in mind that the comparison between these two systems is only qualitative since the quantification of the surface stoichiometry of Pdadmac/SDS spread films from neutral aggregates by NR was not performed.

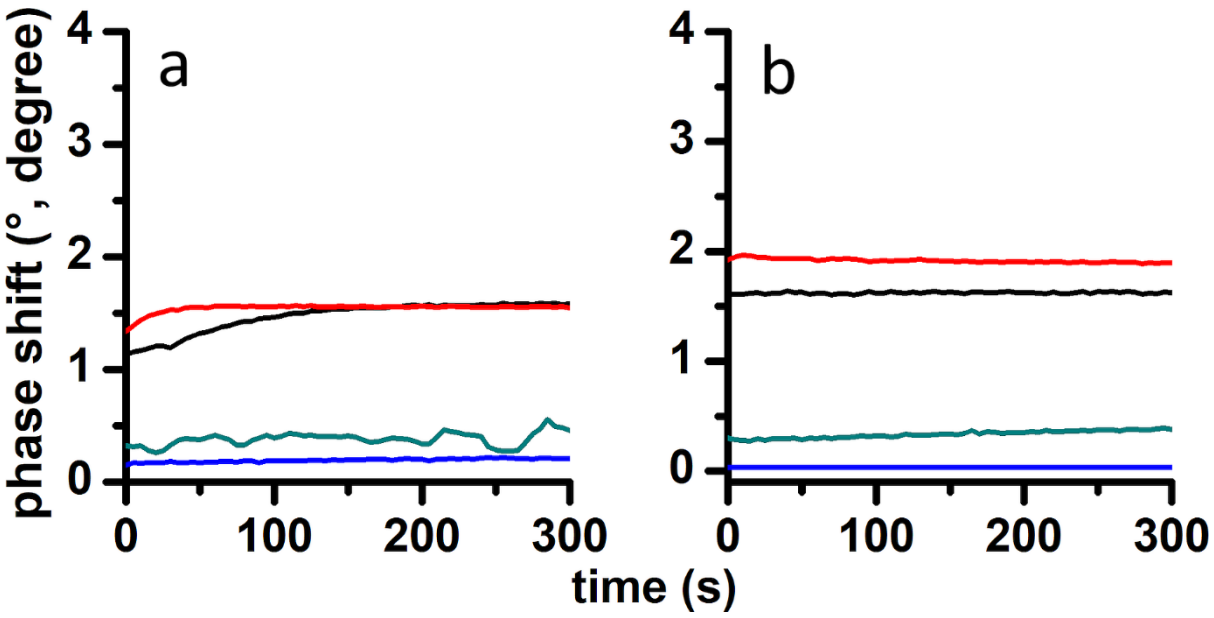

Figure 36 – (a) Variation of the phase shift of Pdadmac/SDS spread films from neutral aggregates in pure water (black curve) and on 100 mM NaCl (red curves). The corresponding adsorbed layers from solutions with an equivalent final bulk concentration in pure water (blue curve) and in 100 mM NaCl (turquoise). (b) Variation of the phase shift for NaPSS/DTAB films. Sample with the same sample history and ionic strength are displayed with matching colors.

These data show that there is some similarity between the two systems. In pure water, spreading neutral aggregates of Pdadmac/SDS results in the formation a trapped film, whose phase shift is 7–9 times higher than adsorbed layers from pre-diluted solutions with equivalent final bulk concentrations, similarly to the case of NaPSS/DTAB films. It is worth noting that the relative surface excess of Pdadmac/SDS spread films 5 minutes after spreading is in agreement with the data available in the literature for this system.[92]

An important difference between the data for spread films on pure water between figure 36a and figure 36b is that in the case of films spread from neutral NaPSS/DTAB aggregates, the phase shift was stable over time immediately after spreading, but for films spread from Pdadmac/SDS aggregates, the phase shift increases over the first few minutes. A similar behavior was observed for films spread from compact/highly charged NaPSS/DTAB aggregates (see chapter 3.3). The explanation may be that neutral aggregates of Pdadmac/SDS are more stable than NaPSS/DTAB aggregates when in contact with the air/water interface. Increased stability may be attributed to a more compact structure of neutral Pdadmac/SDS aggregates than those of NaPSS/DTAB, because of their lower water content. If so, the slightly slower approach to a stable state of dynamic phase shift for Pdamac/SDS spread films on pure water may be explained by the presence of some compact aggregates embedded in the film, which dissociate relatively slowly to give a stable monolayer over the course of few minutes.

The addition of an inert salt to the subphase results in the achievement of the final monolayer quicker than for Pdadmac/SDS films spread on pure water, which can be interpreted in terms of the relative instability of the aggregates, embedded initially in the spread films, as the higher concentration of counterions promotes their dissociation. A similar effect was observed in the fast decrease of the relative surface excess of NaPSS/DTAB spread films from compact/positively charged aggregates on 0.1 M NaCl (see chapter 3.4).

Dynamic condition

An investigation of the surface properties of Pdadmac/SDS spread films from neutral aggregates on pure water was carried out during 5 consecutive compression/expansion cycles of the interface. The data are shown in figure 37. Panel a refers to Padadmac/SDS spread films from neutral aggregates and panel b to those spread from NaPSS/DTAB neutral aggregates (repeated for ease of comparison with figure 24 a). The cycles are shaded in dark from black to light-grey as the experiments proceed. The x-axis ranges differ due to the fact that two different Langmuir troughs were used.

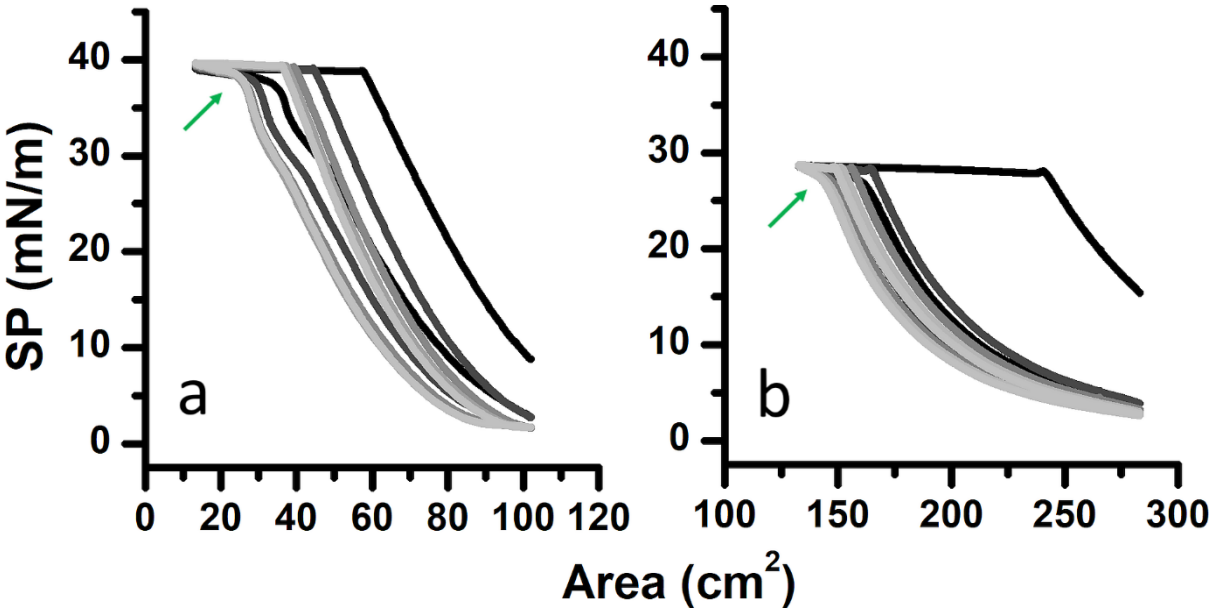

Figure 37 – Surface pressure vs. area isotherms during five consecutive compression/expansion cycles of the interface for (a) Pdadmac/SDS and (b) NaPSS/DTAB spread films from neutral aggregates.

There is a striking difference in the maximum surface pressure of the films (39 mN/m for Pdadmac/SDS vs. 29 mN/m for NaPSS/DTAB), indicating that full monolayers of Pdadmac/SDS lower the free energy of the interface more effectively than those of NaPSS/DTAB films. It is worth noting that the surface pressure values for these two P/S spread films correspond to those reported in literature for full monolayers formed by bulk adsorption from concentrated P/S mixtures, i.e. at compositions matching those of the respective spreading aliquots.[92-94] This demonstrates once more the high efficiency of the

spreading protocol over bulk adsorption both in terms of time required for film formation as well as potential savings in the economic cost of the process, since films produced by spreading require only a minimal amount of starting material. However, the shapes of the isotherms are very similar, which indicates that similar phenomena are exhibited for these two P/S systems. The main difference is that the surface pressure of Pdadmac/SDS spread films reaches a plateau at a higher compression ratio than those of NaPSS/DTAB. It can also be observed that the delay in the relaxation of the surface pressure during the expansion of NaPSS/DTAB spread films decreases steadily as the cycles proceed, while it remains marked for Pdadmac/SDS films even upon successive cycles (green arrows). A similar behavior was observed for spread films from compact and positively charged NaPSS/DTAB aggregates, for which it was concluded that compact P/S particles can remain embedded in the monolayer, acting as nucleation germs for the formation of reservoirs of surface active material. The delay in the relaxation was attributed to the fast resupply of material from the subsurface regions and this was fully supported by BAM images as well as by the analysis of the surface composition derived from NR data analysis (chapter 3.3). It was only through the simultaneous application of all of these surface sensitive techniques that the mechanism of reservoir formation was confirmed. Unfortunately, the present investigation of the dynamic properties of Pdadmac/SDS spread films from neutral aggregates lacks complementary information so far. Therefore, to make such a conclusion would be premature. In particular, measurements of the surface excesses of the two components using NR are missing and these measurements proved to be decisive in the quantification of the interfacial composition when the amount of material exceeded the monolayer coverage. These measurements, as well as the real space investigation of the surface morphology through BAM, are planned for the near future in an extension of this Ph.D. project.

To summarize, a comparison between the Pdadmac/SDS and the NaPSS/DTAB systems has shown that kinetically-trapped, stable P/S films with enhanced surface excess can be readily formed by spreading on pure water neutral aggregates composed of oppositely-charged linear strong P/S mixtures, whether the polyelectrolyte is a polyanion or a polycation. Under static conditions, it has been shown that stable NaPSS/DTAB films are formed immediately after spreading, while a steady increase of the relative surface excess is observed for Pdadmac/SDS spread films over the first two minutes after spreading. This difference may be attributed to the higher compactness of the neutral Pdadmac/SDS aggregates compared to neutral NaPSS/DTAB aggregates, which makes the former aggregates dissociate slower upon

contact with the air/water interface. The influence of the ionic strength on film formation under static conditions has been investigated as well. This investigation showed that spread films of Pdadmac/SDS are formed quicker than in pure water. Less information may be concluded at this stage about the non-equilibrium vs. equilibrium nature of these films, as long measurements of the relative surface excess by ellipsometry are missing.

Under dynamic conditions, both systems exhibit similar behavior, indicating that similar phenomena are occurring when the interface is mechanically perturbed by continuous compression/expansion cycles. Nevertheless, some important differences have been observed. In particular, Pdadmac/SDS spread films are more compressible than the equivalent NaPSS/DTAB films. Moreover, Pdadmac/SDS spread films exhibit higher values of surface pressure at full compression than that of NaPSS/DTAB films, which can be related to the different abilities of the full monolayers to lower the free energy of the interface, rather than aspects specifically related to the spreading of material from aggregates. Another important difference is observed upon expansion, where Pdadmac/SDS films exhibit a more marked delay in the relaxation of the surface pressure. Nevertheless, NR data and BAM images, which are planned for the near future, are necessary to provide a more comprehensive characterization of this system.

3.5.2 Hyperbranched PEI/SDS spread films from neutral aggregates: effects of the pH and molecular architecture

In the last part of the experimental chapters of the thesis, attention is turned on the effects of both molecular architecture and ionization degree of the polyelectrolyte backbone on the properties of P/S spread films from neutral hyperbranched PEI/SDS aggregates. The mixing protocols, as well as the concentration of the polyelectrolyte in the spreading aliquot were the same as for NaPSS/DTAB and Pdadmac/SDS systems. In this case, there was the rapid mixing of 200 ppm polyelectrolyte stock solution in pure water with an equivalent volume of a 1.90 mM aqueous solution of SDS to prepare neutral aggregates of 100 ppm PEI and 0.95 mM SDS.[110] The pH of the PEI stock solution was around 10 and it was freshly prepared before every experiment in order to minimize the adsorption of CO_2, which causes the lowering of the pH. The freshly prepared P/S mixtures were then spread onto an aqueous subphase at pH 4 and 10, prepared by diluting 0.1 M stock solutions of HCl and NaOH respectively. None of the stock solutions of PEI and SDS used in these experiments contained either HCl or NaOH. As the charge density of PEI varies with the pH, any difference in the samples can be related to the protonation state of the polyelectrolyte at the surface in the resulting spread film, which is highly protonated at low pH values and only partially at high pH. In particular, the two pH values in this investigation were chosen because 1) pH 10 matches the pH of the PEI stock solution and 2) the ionic strength for both pH 4 and 10 is equal (0.1 mM).

Another important difference between the PEI/SDS systems and the previously discussed case is the molecular architecture of the polyelectrolyte. While NaPSS and Pdadmac are linear polyelectrolytes, the data presented in this chapter are relative to hyperbranched PEI. The interfacial properties of the surface of NaPSS/DTAB and Pdadmac/SDS spread films showed rather similar behavior, which was attributed to the formation of kinetically-trapped films, at low ionic strength. In the former case, extended structures can be formed either by consecutive spreading or by compressing the interface. At high ionic strength, the thermodynamic equilibrium was favored and no extended structures were observed. To see if this physical picture can be extended also to the case of oppositely-charged hyperbranched P/S spread films, a preliminary investigation on the surface properties of PEI/SDS films is reported with respect to the sample history and the subphase ionic strength, both under static and dynamic conditions.

Static condition

pH 4

For the PEI/SDS system, it has been demonstrated that the pH has a major influence on the stability of PEI/SDS aggregates in bulk[22] as well as on their interaction at the air/water interface.[110,121] In particular, it was observed that PEI/SDS aggregates can persist intact at the air/water interface when the pH of their solution was low, while they were not detected at high pH.[121] As the presence of aggregates at the interface is essential to determine the properties of P/S films, which ultimately depends on the pH of the subphase, it remained open to investigate if such an effect can be also exploited to form trapped layers on an extremely dilute (P/S-free) subphase.

Long dynamic ellipsometry measurements were used once more to investigate the possibility of forming kinetically-trapped P/S films at the air/water interface. Data for the PEI/SDS system are shown in figure 38a. The variation of the phase shift was monitored over 15 hours for two different sample histories, i.e. spreading small aliquots of neutral PEI/SDS aggregate mixtures (black curve) vs. bulk adsorption from pre-diluted solutions of the two components (red curve).

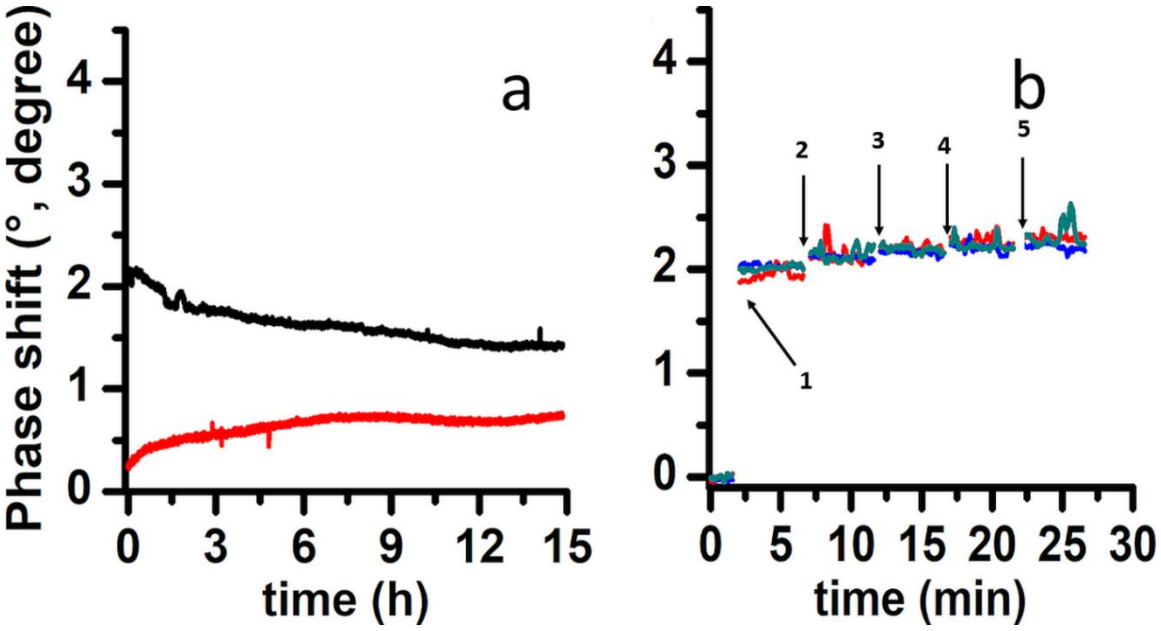

Figure 38 – (a) Variation of the phase shift of a PEI/SDS spread film (black) and adsorbed layers (red) on pH 4 aqueous subphase over an extended time. (b) Variation of the phase shift of 5 consecutive additions PEI/SDS aliquots on pH 4 aqueous subphase. Each color corresponds to independent measurements.

As it was observed for the two previous P/S systems, the Marangoni spreading of P/S aggregate mixtures allows one to prepare a surface loaded films with enhanced surface excess, which are not in equilibrium with the bulk on experimentally accessible time scales. However, some differences with both the NaPSS/DTAB and the Pdadmac/SDS systems are

noticeable. In particular, PEI/SDS spread films show a long stabilization time, during which the dynamic phase shift decreases slowly over 12 hours. This behavior is indicative of gradual loss of material from the interface to the bulk of the system until a more stable state is reached. In addition, temporal fluctuations of the signal during the first 3 hours are observed, which can be attributed to the presence of extended P/S structure and/or embedded aggregates in the films.

Next, 5 consecutive additions, using the same stepwise approach described in chapter 3.3, were performed in order to investigate further the aggregate dissociation at the interface as well as to see if it is possible to boost further the relative surface excess measured by ellipsometry. These data are reported in figure 38b for three independent measurements and they show that the step-wise approach causes only a slight increase of the phase shift and does not affect the amplitude of the oscillation significantly. Such behavior can be attributed to the fast spreading and dissociation of aggregates to form a homogeneous layer at this pH,[110] although the small temporal fluctuations may be caused by the presence of compact aggregates in the spread layer or to the transient formation of extended structures that quickly are lost to the bulk.

pH 10

The investigation was then extended to PEI/SDS films formed either by spreading or adsorption, on a subphase with high pH, by using the same experimental protocols. Long dynamic ellipsometry measurements are reported in figure 39a for PEI/SDS films spread from neutral aggregates (black and red curves) and PEI/SDS adsorbed layers from pre-diluted solutions of the two components with equivalent final bulk concentrations (blue curve). The red and the black curve in figure 39a represent to two independent measurements of the variation of the phase shift after spreading. The reason to report both the curves is to highlight the reproducibility of the relative surface excess behavior with respect to time.

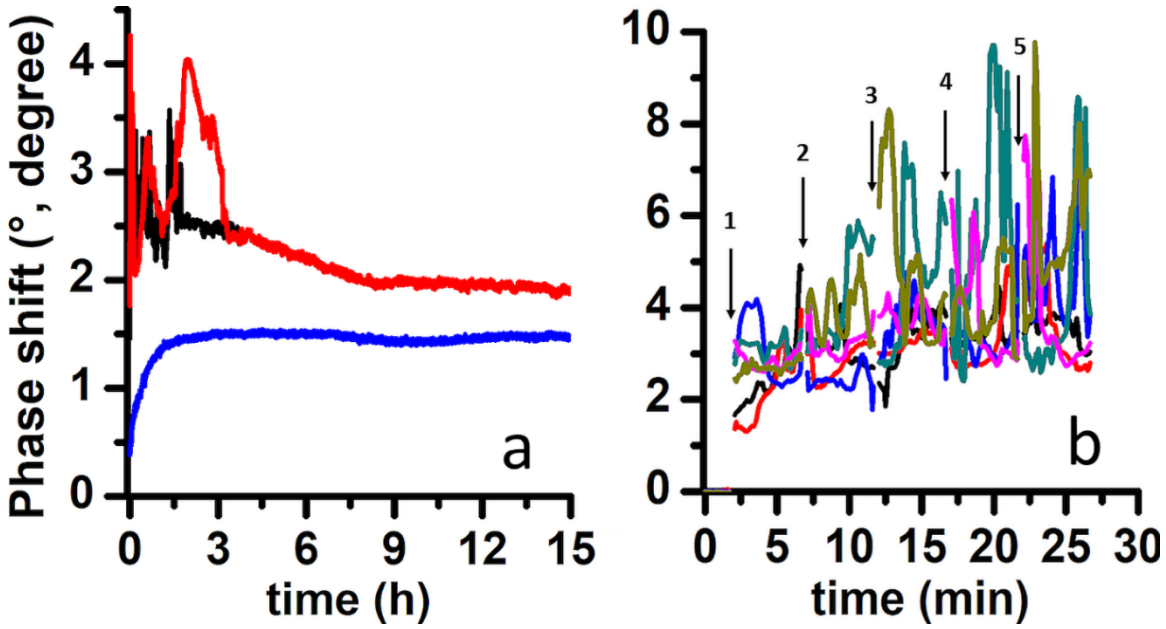

Figure 39 - (a) Variation of the phase shift of PEI/SDS spread films (black and red) and an adsorbed layer (blue) on pH 10 aqueous subphase over an extended time. (b) Variation of the phase shift of 5 consecutive additions PEI/SDS aliquots on pH 10 aqueous subphase. Each color corresponds to independent measurements.

These data show that there are some changes in the nature of films spread on a subphase with pH 10. On the one hand, the long dynamic phase shift of the spread films (red curve and black in panel a of figure 39) always exceeds the signal of the adsorbed layers from pre-diluted solutions, confirming once again that P/S spread films prepared on a subphase at low ionic strength are not in equilibrium with the bulk of the system; on the other hand some differences are observed for both spread films and adsorbed layers. For spread films at pH 10, big temporal fluctuations of the signal are observed over the first 4 hours after spreading. After this time, the signal starts decreasing and becomes stable after around 8 hours. These observations suggest that either extended structures in the surface layer are present or that a large amount of aggregate remains intact upon spreading at pH 10. This result is coherent with the data published by Tonigold and co-workers,[113] in which fluctuations of the ellipsometric signal of PEI/SDS mixtures at pH 10 were interpreted in terms of intact aggregates embedded in the surface layer.

When 5 aliquots of P/S aggregate dispersions are consecutively added (stepwise protocol in chapter 3.3) onto the surface, more and more material can be delivered at the interface as shown in figure 39 b, where five independent measurements are reported and displayed with different colors. It can be seen that not only the number but also the amplitude of the fluctuations of the phase shift is increased after each addition. Thus, the pH of the subphase affects the stability of neutral PEI/SDS aggregates: they are more stable at pH 10 were the protonation state of the polyelectrolyte is less affected. The formation of extended structures

at high pH for 750-kDa hyperbranched PEI/SDS mixtures has been already reported by Penfold and co-workers for the static air/water interface.[150,151] Also, Tonigold *et al.* showed that PEI/SDS aggregates can remain trapped at the air/water interface when the pH of their mixtures is high.[113] It is important noting that the study in ref. 113 was carried out on the surface of concentrated PEI/SDS mixtures, i.e. at a concentration close or equivalent that of the spreading aliquots used for the preparation of spread films in this thesis. It would be perhaps surprising if neutral PEI/SDS aggregates were to at the interface persist many hours even when the system has been highly diluted. However, it is not possible to distinguish the formation of extended structure and the presence of aggregates in the spread film, as useful complementary information from BAM and NR are missing to date. These measurements are, however, planned for the near future in a continuation of this Ph.D. work.

The adsorption of PEI/SDS is also affected. At pH 10 the adsorption becomes faster and, apparently, more material is present at the interface after that the system has reached equilibrium than in the corresponding measurements at pH 4. This can be attributed to the protonation state of the polyelectrolyte at the two different pH values, as at pH 10 PEI is more hydrophobic due to the decreased electric charge on its backbone.

Dynamic condition

The dynamic properties of PEI/SDS films spread from neutral aggregates were investigated by the means of 5 consecutive compression/expansion cycles of the interface. These measurements proved to be very useful in order to understand the mechanical properties of NaPSS/DTAB and Pdadmac/SDS spread films at the air/water interface. The surface pressure vs. area isotherms of films spread from neutral PEI/SDS aggregates on pH 4 and 10 subphases are reported in figure 40, respectively in panel a and in panel b. These results reveal interesting differences in the mechanical properties with respect to the subphase pH, indicating that the strength of the interaction in the resulting spread films can be used effectively to tune their mechanical properties.

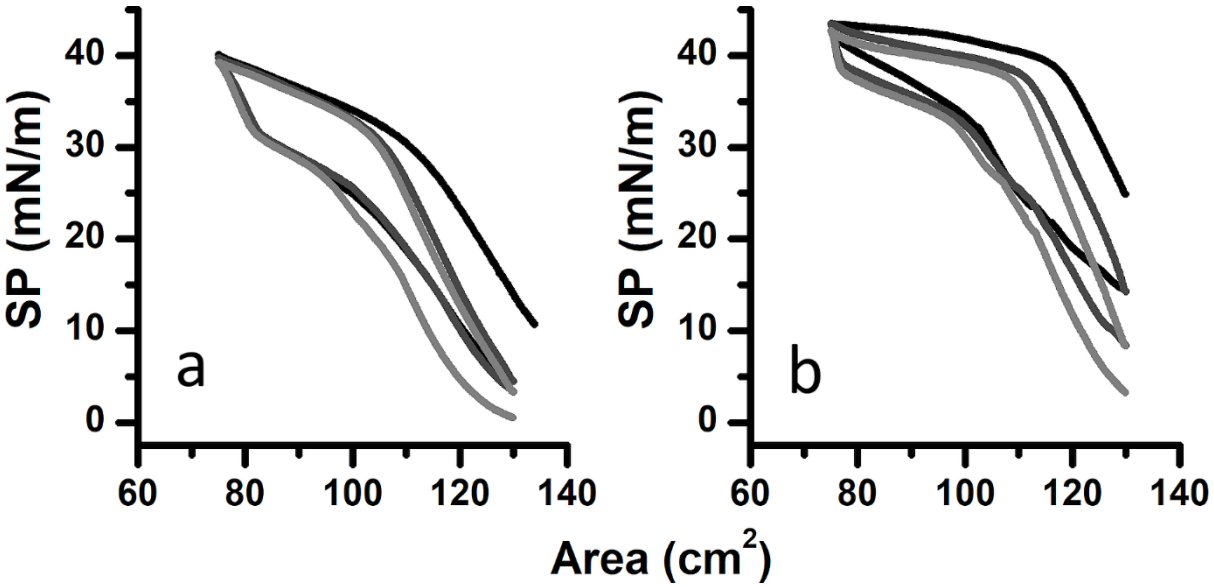

Figure 40 – Surface pressure vs. area isotherms of PEI/SDS spread films from neutral aggregates on (a) pH 4 and (b) pH 10 aqueous subphase. The cycles are shaded from black to light-grey as the experiment proceeds.

First, the surface pressure value at full compression for films spread on pH 10 (panel b) is around 44 mN/m, while that of films spread on pH 4 (panel a) aqueous subphase is around 40 mN/m. These values correspond to those of saturated P/S layers of concentrated solutions.[150,151] Secondly, the shapes of the two isotherms in figure 40, upon compression and expansion, are rather different. These differences demonstrate that the P/S interactions in the spread films are affected by the degree of protonation of the polyelectrolyte. In particular, the P/S films spread on pH 4 aqueous subphase (panel a) exhibit higher compressibility and they reach only a pseudo-plateau upon compression, in which the surface pressure further increases gradually from 30 mN/m to 40 mN/m. During the expansion of the interface, the surface pressure decreases, first steeply, but then it reaches a second pseudo-plateau, before decreasing to 5 mN/m. Hysteresis is observed between compression and expansion and a limiting behavior is reached already during the second compression. A similar behavior was described in the preliminary experiment about the properties of DF-HSA spread films (chapter 3.1). In that case, the hysteresis was attributed to the strong lateral interactions between protein molecules at the air/water interface, while the limiting cycle was attributed the mechanical annealing of the protein layer into a more stable morphology. For the PEI/SDS spread films on a subphase at pH 4, the increased electrostatic attraction between polyelectrolyte segments and surfactant molecules at the interface, due to the higher charge density of the polyelectrolyte at low pH, may also result in increased lateral interactions in the surface layer. However, the investigation of the morphology of the interface through BAM as well as a direct measurement of the surface excess measured by NR are still missing.

When neutral PEI/SDS aggregates are spread on a subphase at pH 10, the surface pressure of the resulting films increases until a plateau (44 mN/m) is reached during the compression of the interface. Upon expansion, the surface pressure initially decreases monotonically down to a value of 15 mN/m. During the second compression of the interface, the surface pressure goes back to its plateau value, though at a higher compression of the interface. The situation changes during the second expansion, where the relaxation of the surface pressure exhibits three different slopes. The surface pressure first relaxes abruptly going from 43 mN/m to 37 mN/m, then it reaches a second pseudo-plateau, and lastly a steeper drop is observed during the expansion. On the one hand the re-adsorption of material from any extended structure formed by compressing the interface may explain this behavior upon expansion; on the other hand it cannot easily explain why the shape of the isotherms changes from the first to the second expansion. A possible explanation may be that the stability of any extended structures reduces with time. However, even their presence has yet to be confirmed by NR measurements. A limiting behavior is reached during the third cycle, which is indicative of the formation of a stable layer.

Lastly, the surface pressure vs. area behavior of PEI/SDS spread films on aqueous subphase at pH 4 or pH 10 is very different to those of strong linear P/S spread films. It is known that the dynamic surface properties at the air/water interface of linear P/S films are influenced by the rigidity of the polyelectrolyte backbone.[86,87] In these studies, although some differences in the surface activity of different P/S systems were pointed out, which were correlated to foam film stability, the overall shapes of the isotherm for linear polyelectrolyte showed marked similarity, indicating that the same phenomena were occurring at the interface, regardless of the rigidity of the polyelectrolyte backbone. The same trend has been observed and described at the beginning of the present chapter of this thesis as well, where the results attained for the NaPSS/DTAB spread films were compared to those of Pdadmac/SDS. Therefore, the different shape of the isotherms for spread films of neutral aggregates of the hyperbranched PEI/SDS system appear to be related to the different molecular architectures involved rather than simply to the different electrostatic interaction.

In this chapter, it has been shown that the pH of the subphase on which weak P/S films are spread is a crucial parameter in determining the properties of the resulting films. Under static conditions, the relative surface excess of films spread on subphase at high pH showed big temporal fluctuations, which can be attributed either to the presence of intact aggregate embedded in the spread layer or to the formation of extended structures formed by dropwise

addition of material on the surface. At low pH, this behavior was not observed and, apparently, only a P/S monolayer can be achieved. Under dynamic conditions, it has been shown that the pH of the subphase can be effectively used to tune the interaction in the P/S spread films. Moreover, this study has demonstrated once again that spread P/S films spread from neutral aggregates have a non-equilibrium nature regardless of the nature of the components used for film preparation, even though the surface mechanical properties depend on the molecular architecture of the polyelectrolyte backbone.

Further work is required before the nature of spread filoms prepared from P/S aggregates may be generalized to different systems. Indeed, a comprehensive investigation about the properties of P/S spread films in this thesis has been completed only for the NaPSS/DTAB systems to date. A thorough characterization of the effects of the aggregates charge/structure as well as the ionic strength of the subphase was carried out by the application of several surface sensitive techniques and it was only through the simultaneous combination of all of these techniques that the mechanism of film formation as well as the presence of extended structures was revealed. The preliminary results on Pdadmac/SDS and hyperbranched PEI/SDS systems described in this chapter represent a promising start in the process to generalize the physical properties of spread P/S films to different types of system. Work on films prepared from aggregates with different charge/structure using various techniques, including NR, are foreseen. While it was not possible to apply NR to the Pdadmac/SDS and PEI/SDS systems during this Ph.D. project, awards amounting to a value of > 100.000 € have been made in the project and two NR experiments are planned for later in 2018 to continue this work.

Chapter 4: Conclusions and outlooks

The aim of this Ph.D. thesis was to shed light on the preparation of macromolecular films with enhanced surface excess at the air/water interface by exploiting non-equilibrium effects. For this purpose, a systematic investigation of the sample history of films created in a range of systems was carried out. In detail, two different sample handling protocols were adopted for the preparation of the films at the air/water interface: spreading aqueous mixtures containing water-soluble macromolecules vs. adsorption from the bulk of pre-diluted solutions with equivalent final bulk concentrations. The final total bulk concentration of the samples with different histories was kept constant so that the chemical potential of the species in the system was not varied by the sample handling. To avoid the interference of any trapped material at the interface, the surface of all of the pre-diluted systems was cleaned by aspiration. The surface properties have been studied both at the static air/water interface, in a Petri dish made of glass, and during consecutive compression/expansion cycles in a Langmuir trough. It is through the combination of several surface sensitive techniques, in cases performed simultaneously, that the non-equilibrium nature of spread films of macromolecules has been revealed. In particular, *in situ* NR, ellipsometry and BAM measurements in combination of surface pressure monitoring have proved to be essential tools for this work.

The focus of the preliminary investigation (chapter 3.1) was a study of the mechanism of film formation, the durability and the morphology of spread films of DF-HSA. This work provided new insight on an old problem in interfacial science. It was demonstrated that spread films of DF-HSA can be trapped at the air/water interface only when the concentration of protein in the spreading aliquot is sufficiently high, i.e. when its surface tension is low enough to activate Marangoni flows. When this condition is achieved, the proteins molecules spread from the bulk of the droplets to the air/water interface on the sub-second time scale, allowing the fast formation of a spread film. These films exhibit boosted surface excess and enhanced surface properties compared with those formed by diffusion-driven bulk adsorption. The surface loaded protein films remain stable on experimentally accessible time scales under static conditions. This proved that a kinetic barrier preventing the thermodynamic equilibration between the surface and the bulk of the systems is prevalent. This kinetic barrier comes as a result of the attractive lateral interactions between adjacent macromolecules at the interface. Moreover, it has been proven that DF-HSA films are very resistant and durable. They are shown to be impervious to mechanical perturbation of the

interface, as the surface excess monitored by *in situ* ellipsometry measurements did not vary over consecutive compression/expansion cycles of surface. At the same time, the surface pressure vs. area isotherms showed marked hysteresis and the images obtained by BAM evidenced the lateral inhomogeneity in the film. This behavior is not related to thermodynamic equilibration of the surface, but to the mechanical annealing of the interface to a more durable morphology. This work provided essential experience in the methodologies and experimental techniques that were to be used subsequently.

The core of the thesis concerned the mechanism of film formation and the properties of P/S films spread from self-assembled oppositely-charged P/S aggregates in aqueous media onto a pure aqueous subphase. In this case, the polyelectrolyte alone is not surface active and it is its encapsulation into a liquid crystalline matrix with oppositely-charged surfactants that allows its exploitation. Such a film formation methodology may have reduced cost, improved activity and a more eco-friendly nature since all the steps involved in the preparation of P/S spread films by exploiting aggregates dissociation are free of organic solvents. Once more, the comparison of different sample histories was crucial to resolve the equilibrium vs. non-equilibrium features of the films formed at the air/water interface. In this direction, the first study focused on forming trapped NaPSS/DTAB films by spreading from neutral aggregates mixtures (chapter 3.2). It was demonstrated that film formation occurs by the quick spreading by Marangoni flow combined with the fast dissociation of the P/S aggregates in the spreading aliquot upon contact with air/water interface. A kinetic barrier prevents the dissolution of the excess of material, as confirmed by ellipsometry measurements. The main contribution to this activation barrier is the entropic gain of counterion release as soon as the aggregates are put in contact with the pure water subphase (mixing entropy). In addition, one has to take in account the fact that macromolecule desorption has to occur at once; as long as a segment (or monomer) remains attached to a surface, the whole molecule is still adsorbed. The probability that the sudden desorption of all segments occurs simultaneously decreases with increasing number of polymer segments.

The durability of NaPSS/DTAB films spread from neutral aggregate dispersions was characterized by surface pressure vs. area isotherms, and the surface excesses of both components were derived by *in situ* NR measurements. It was found that a plateau in surface pressure is reached at a value of 28 mN/m, corresponding to the surface pressure of saturated NaPSS/DTAB films in a concentrated mixture, i.e. with the same concentration of the spreading aliquot. Upon further compression, the excess of material with respect to a full

monolayer was expelled from the film. Upon expansion, the hysteresis of the surface pressure with a delay in relaxation was observed. From the first compression to the second, a big decrease in the extent of the plateau was observed, while the diminution was much smaller for the following cycles. It was only through the simultaneous application of NR during surface pressure measurements that it was possible to rationalize such behavior. In particular, a minimal loss of both components was observed between the first and second cycles, which is the clear evidence that the decrease in the extent of the plateau is related to the loss of surface active material. However, from the second cycle to following ones, the surface excess of both components remained constant: both the maxima (full compression) and minima (full expansion) of the plots of the surface excess vs. area did not vary. This result demonstrated the elastic and insoluble nature of the formed film.

This was also the first time that the surface excesses of the polyelectrolyte and surfactant were derived in such a mixture during mechanical perturbations of the interface. This result was achieved thanks to the significant instrumental improvements achieved in NR during the last 10 years, particularly with the commissioning of the FIGARO reflectometer at ILL, and the development of the novel low-q approach, which allows one to follow the evolution of a process on time scales ranging from one second to some minutes. As a consequence, it has been resolved that polyelectrolyte monomers and surfactant molecules bind at the interface in a 1:1 molar charge ratio, regardless of the compression state of the formed films as long as the ionic strength of the subphase is kept low. This result is in support of assumptions made in this field 20 years ago by Langevin and co-workers, which until now lacked clear experimental evidence.

In the next steps, the effects of the charge/structure of NaPSS/DTAB aggregates (chapter 3.3) as well as the ionic strength of the subphase (chapter 3.4) were investigated, again both under static and dynamic conditions. In the former case, the terminology “charge/structure” is used as both parameters change with varying bulk composition. It has been found that the formation of extended structures with reservoirs of surface active material is triggered by the presence of compact/positively charged P/S aggregates that remain embedded in the spread film, while the swollen/negatively charged aggregates are not able to activate the same mechanism.It has been shown that the higher the charge of the aggregates, the higher is the surface excess, and the slower is the relaxation of the surface pressure thanks to the fast resupply of surface active materials from extended P/S structures. Therefore, the charge/structure of the aggregates has a big impact on the formation of extended P/S

structures. Similar consideration of reservoir dynamics can be made for lung surfactants, in which protein molecules nucleate the formation of reservoirs of material upon compression and the fast resupply of material to the interface upon expansion of the alveoli, although there are important differences between the systems as well. Nevertheless, the data shown in this Ph.D. thesis demonstrates clearly that it possible to tune the formation of extended structures (in terms of amount of material and morphology) through a fine control of several experimental variables, namely the charge/structure of the aggregates, the sample history, the surface area, and the subphase ionic strength. This was the first time that such a control over extended structures at the air/water interface was achieved.

The ionic strength of the aqueous subphase was also shown to play an important role in the balance between kinetic vs. thermodynamic control of the properties of spread NaPSS/DTAB films. One the one hand, the addition of inert salt into the bulk promotes (slow) equilibration between the bulk and the interface. In fact, both spread films from concentrated P/S mixtures and adsorbed layers from pre-diluted P/S solutions reach the same surface excess. Nevertheless, the spreading approach was more efficient (i.e. quicker) to reach equilibrium, since it took two hours for the dilute P/S system to reach equilibrium by diffusion and adsorption of bulk complexes at the air/water interface, while it was visually immediate for the spread films.

The composition of the interface is strongly affected by the subphase ionic strength, and the differences become clear as the surface is compressed. At full compression the polyelectrolyte surface excess is always significantly above that of the surfactant, indicating that the relative amount of polyelectrolyte at the interface is gradually increasing as the surface is compressed. This feature is explained in terms of formation of polyelectrolyte loops at high ionic strength. With added salt in the system, the release of counterions into the bulk of the solution becomes less favorable and the counterions can now replace the surfactant molecules in the spread film when they are squeezed out of the film. This effect decreases both the electrostatic repulsion between polymer segments and the difference in osmotic pressure between the inside of the macromolecule coil and the medium, allowing the polyelectrolyte chain to form loops.

In order to turn the spreading approach into a viable technological technique, the mechanism of formation of P/S films was tested with two other systems, involving neutral aggregates of Pdadmac/SDS and hyperbranched PEI/SDS, in an initial preparatory study using ellipsometry and surface pressure vs. area isotherms (chapter 3.5). The object of the investigation was

extended to the influence of the molecular structure and the charge density on the polyelectrolyte backbone, the latter achieved by varying the pH of the subphase on which the mixtures of neutral PEI/SDS aggregates were spread. This was the first time that the influences of these parameters have been investigated for spread P/S films. It has been found again that the criterion to form surface loaded P/S films by spreading is the low ionic strength of the subphase. Moreover, the behavior of the surface properties of NaPSS/DTAB and Pdadmac/SDS films exhibit strong similarities, both under static and dynamic conditions, while different mechanical behavior was observed for PEI/SDS spread films. From these data, it was inferred that the mechanical properties of the interface are controlled by the molecular architecture of the polyelectrolyte as well as its charge density. However, NR data for these two systems are missing, so more work is required in order to generalize the behavior of spread P/S to different kinds of system. Indeed, the formation of extended structures or reservoirs of surface active material reservoirs has been confirmed only for the NaPSS/DTAB systems. A general picture that takes into account the effects of the polyelectrolyte charge density, as well as its molecular architecture, will be accessible only with NR and BAM experiments on the Pdadmac/SDS and hyperbranched PEI/SDS spread films. This extension of the Ph.D. project is already planned for later in 2018 with 2 allocations of NR beam time already awarded.

As concerns longer-term extensions of this Ph.D. project, several direction for future research are possible. It was pointed out that the formation of extended structures in spread films of NaPSS/DTAB has some analogy to the reservoir formation in lung surfactants, which are mixtures of lipids and proteins, noting, however, the big difference in biocompatibility between the synthetic P/S systems investigated to date and that of lung surfactant. Therefore, a natural course of this project will move toward understanding the behavior of spread films of known biocompatible P/S systems, such as DNA[152], hyaluronic acid derivatives[153] and dialkylammonium bromide (DAB), like dioctadecyldimethylammonium bromide (DODAB),[152,154] for instance.

A second posiible extension of this project involves the Marangoni spreading oppositely-charged inorganic nanoparticle/surfactant systems (NP/S), in order to investigate the possibility of forming/controlling the formation of extended structures at the air/water interface. Nanoparticles and surfactants are essential building blocks in modern colloid science and their interaction has attracted attention during the last decades.[62,64] Stable nanoparticle dispersions are, generally, attained by electric stabilization, i.e. by charging up

their surface. Thus, they are macroions, like polyelectrolytes. The interest in investigating NP/S mixtures is multifold. On the one hand, they are promising candidates in biomedical science because, according to their design and composition, can be used both for diagnostic purpose as well as therapeutic (*theranostic*).[155] On the other hand, it is relatively easy to tune the size/shape/charge of inorganic NPs by modifying the synthetic pathway, and this gives the great advantage of design NPs with pre-designed characteristics.

A third possible extension of this project is the investigation of the properties of spread films from natural lung surfactant at the air/water interface in order to bridge the gap from the behavior of synthetic P/S and NP/S systems to these biologically relevant systems. Lung surfactants are mixtures of phospholipids, like dipalmitoylphosphatidylcholine (DPPC), and proteins. The role of the protein is to activate the storage of surface active material in the sub-surface region upon compression and to release it back in the monolayer upon expansion. It is because of the extremely low surface tension of lung surfactant[159] that the continuous compression/expansion of the alveoli can occur, preventing the rupture of their membranes and allowing us to breathe. The deficiency of lung surfactant is very common in prematurely born babies, but it can affect any individual regardless of ages. Lack of lung surfactants causes severe respiratory distress syndrome (SRDS),[160] which can bring to death. The treatment for lung surfactant deficiency consists in the inhalation of lung surfactant extracted from animal origin and, to our knowledge, the use of synthetic lung surfactants has not been fully achieved yet. In this direction, the findings about the controlled reservoir formation in P/S spread films and the information attained from the future studies on biocompatible P/S systems with synthetic origin and NP/S may lead to a contribution in this field, by helping in the rational design of novel P/S systems for novel drug formulations.

Bibliography

1. Bain, C. D., Claesson, P. M., Langevin, D., Mészáros, R., Nylander, T., Stubenrauch, C., Titmuss, S., von Klitzing, R. Complexes of Surfactants with Oppositely-charged Polymers at Surfaces and in Bulk, *Adv. Colloid Interface Sci*, **2010**, 155, 32–49.
2. Guzmán, E., Llamas, S., Maestro, A., Fernández-Peña, L., Akanno, A., Miller, R., Ortega, F., Rubio, R. G. Polymer–Surfactant Systems in Bulk and at Fluid Interfaces, *Adv. Colloid Interface Sci.*, **2016**, 233, 38–64.
3. Llamas, S., Guzmán, E., Ortega, F., Baghdadli, N., Cazeneuve, C., Ramón, G., Rubio, R. G., Luengo, G. S., Adsorption of Polyelectrolytes and Polyelectrolytes-Surfactant Mixtures at Surfaces: a Physico-chemical Approach to a Cosmetic Challenge, *Adv. Colloid Interface Sci.* **2015**, 222, 461–487.
4. Radoiu, M. T., Martin, D. I., Calinescu, I., Iovu, H. Preparation of polyelectrolytes for wastewater treatment, *J. Hazard Mater.*,106B, **2004**, 27–37.
5. Shen, L.-C., Nguyen, X.-T., Hankins, N. P. Removal of Heavy Metal Ions from Dilute Aqueous Solutions by Polymer–Surfactant Aggregates: a Novel Effluent Treatment, *Process. Sep. Purif. Technol.*, **2015**, 152, 101–107.
6. Abdallah, B.G., Ros, A., Microfluidic Devices for Biomedical Applications, chapter 2: Surface coatings for microfluidic-based biomedical devices, *Woodhead Pub.*, **2013**, 63–69.
7. Szczepanowicz, K., Bazylinska, U., Pietkiewicz, J., Szyk-Warszynska, L., Wilk, K. A., Warszynski, P. Biocompatible Long-Sustained Release Oil-Core Polyelectrolyte Nanocarriers: from controlling Physical State and Stability to Biological Impact, *Adv. Colloid Interface Sci.*, **2015**, 222, 678–691.
8. Moran, M. C., Alonso, T., Lima, F. S., Vinardell, M. P., Miguel, M. G., Lindman, B. Counter-Ion Effect on Surfactant–DNA Gel Particles as Controlled DNA Delivery Systems, *Soft Matter*, **2012**, 8, 3200–3211.
9. Nakahara, H., Lee, S., Sugihara, G., Chang, C.-H., Shibata, O. Langmuir Monolayer of Artificial Pulmonary Surfactant Mixtures with an Amphiphilic Peptide at the Air/Water Interface: Comparison of New Preparations with Surfacten (Surfactant TA), *Langmuir*, **2008**, 24, 3370–3379.
10. Chavanpatil, M. D., Khdair, A., Patil, Y., Handa, H., Mao, G., Panyam, J., Polymer-surfactant Nanoparticles for Sustained Release of Water-soluble Drugs, *J. Pharm. Sci*., **2007**, 96, 3379–3389.
11. Danesh, C. D., Starkweather, N. S., Zhang, S. In Situ Study of Dynamic Conformational Transitions of a Water-Soluble Poly(3-Hexylthiophene) Derivative by Surfactant Complexation, *J. Phys. Chem. B*, **2012**, 116, 12887–12894.
12. Hermans, J. J., Overbeek, J. TH. G. The dimensions of charged long chain molecules in solutions containing electrolytes, *Recl. Trav. Chim. Pays-Bas*, **1948**, 67, 761–776.
13. Kuhn, W., Kunzle, O., Katchalsky, A., Dénouement de molécules en chahes polyvalentes par des charges électriques en solution, *Bull. Soc. Chim. Belg.*, **1948**, 57, 421–431.
14. Kuhn, W., Hargitay, B., Reversible dilation and contraction by changing the state of ionization of high-polymer acids networks, *Nature*, **1950**, 165, 514–516.
15. Hayter, J., Janninck, G., Brochard-Wyart, F., De Gennes, P. G., Correlations and dynamics of polyelectrolyte solutions, *J. Physique - LETTRES*, **1980**, 41, 451–454.
16. Barratt, J. L., Joanny, J. F., Polymeric systems, chapter 1: Theory of polyelectrolyte solutions, *Adv. Chem. Phys.*, **1995**.
17. Sinn, C. G. Dimova, R., Antonietti, M., Isothermal Titration Calorimetry of the Polyelectrolyte/Water Interaction and Binding of Ca2+: Effects Determining the Quality of Polymeric Scale Inhibitors, *Macromolecules*, **2004**, 37, 3444–3450.

18. Dobrynin, A. V., Colby, H. R., Rubinstein, M., Scaling theory of polyelectrolytes solutions, *Macromolecules*, **1995,** 28, 1859–1871.
19. Manning, G. S., Limiting Laws and Counterion Condensation in Polyelectrolyte Solutions I. Colligative Properties, *J. Chem. Phys*., **1969,** 51, 924–933.
20. De Gennes, P. G., Pincus, P., Velasco, R. M., F. Brochard, Remarks on polyelectrolyte conformations, *J. Phys. France*, **1976**, 1461–1473.
21. Orofino, T.A., Flory, P. J., The second virial coefficient for polyelectrolytes, theory and experiment, J. *Phys. Chem.*, **1959**, 63, 283–290.
22. Mezei, A., Mészáros, R., Varga, I., Gylányi, T. Effect of Mixing on the Formation of Complexes of Hyperbranched Cationic Polyelectrolytes and Anionic Surfactants. *Langmuir*, **2007**, 23, 4237–4247.
23. Kaji, K. Urakawa, H., Kanaya, T., Kitamaru R., Phase diagram of polyelectrolyte solutions, *J. Phys. France*, **1988**, 49, 993–1000.
24. Sedlák, M., Amis, E. J., Concentration and molecular weight regime diagram of saltfree polyelectrolyte solutions as studied by light scattering, *J. Chem. Phys*., **1992**, 96, 826–834.
25. Schweins, R., Hollmann, J., Huber, K. J., Dilute solution behaviour of sodium polyacrylate chains in aqueous NaCl solutions, *Polymer*, **2003**, 44, 7131–7141.
26. Noda, I., Tsuge, T., NagasawaM., The Intrinsic Viscosity of Polyelectrolytes, *The .Journal of Physical Chemistry*, **1970**, 74, 710–719
27. Barrat, J. L., Joanny, J. F., Theory of polyelectrolyte solutions, *Adv. Chem. Phys.: Polymeric systems*, **1995**, chapter 1.
28. Odijk, T., Polyelectrolytes near the Rod Limit, *J. Polym. Sci.: Polymer Physics Edition*, **1977**, 15, 477–483.
29. Sedlák, M., The ionic strength dependence of the structure and dynamics of polyelectrolyte solutions as seen by light scattering: the slow mode dilemma, *J. Chem. Phys.*, **1996**, 105, 10123–10133.
30. Lages, S., Lindner, P. Sinha, P. Kiriy, A. Stamm, M., Huber, K., Formation of Ca^{2+}-induced intermediate necklace structures of polyacrylate chains, *Macromolecules*, **2009**, 42, 4288–4299.
31. Dubois, E., Boue, F., Conformation of Poly(styrenesulfonate) Polyions in the Presence of Multivalent Ions: Small-Angle Neutron Scattering Experiments, *Macromolecules*, **2001**, 34, 3684–3697.
32. Théodoly, O., Ober, R., Williams, C. E., Adsorption of hydrophobic polyelectrolytes at the air/water interface: Conformational effect and history dependence, *Eur. Phys. J. E.*, **2001**, 51–58.
33. Ahrens, H., Förster, S. Helm, C. A., Polyelectrolyte Brushes Grafted at the Air/Water Interface, *Macromolecules*, **1997,** 30, 8447–8452
34. Tripp, B. C.,Magda, J. J., Andrade, J. D., Adsorption of globular proteins at the air/water interface as measured via dynamic surface tension: concentration dependence, mass-transfer considerations, and adsorption kinetics, *J. Colloid Interface Sci.*, **1995**, 173, 16–27.
35. Beverung, C. J., Radke, C.J., Blanch, H.W., Protein adsorption at the oil/water interface: characterization of adsorption kinetics by dynamic interfacial tension measurements, *Biophys. Chem.*, **1999**, 81, 59–80.
36. Szilvay, G. R., Paananen, A., Laurikainen, K., Vuorimaa, E., Lemmetyinen, H., Peltonen, J., Linder, M B., Self-Assembled Hydrophobin Protein Films at the Air-Water Interface: Structural Analysis and Molecular Engineering, *Biochemistry*, **2007**, 46, 2345–2354.
37. Frommer, M. A., Miller, I. R., Adsorption of DNA at the air-water interface, *J. Phys. Chem.*, **1968**, 72, 2862–2866.
38. Okubo, T., Surface Tension of Synthetic Polyelectrolyte Solutions at the Air-Water Interface, *J. Colloid Interface Sci.*, **1988**, 125, 386–398.

39. Razumovsky, L., Damodaran, S., Surface Activity-Compressibility Relationship of Proteins at the Air-Water Interface, *Langmuir*, **1999**, 15, 1392–1399.
40. Damodaran, S., Interfaces, protein films, and foams, *Adv. Food Nutr. Res.*, **1990**, 34, 1–79.
41. Lu, J. R., Su, T. J., Penfold, J., Adsorption of Serum Albumins at the Air/Water Interface, *Langmuir*, **1999**, 15, 6975–6983.
42. Steinhardt, J., Krijn, J., Leidy J. G., Differences between Bovine and Human Serum Albumins: Binding Isotherms, Optical Rotatory Dispersion, Viscosity, Hydrogen Ion Titration, and Fluorescence Effects, *Biochemistry*, **1971**, 22, 4005–4015.
43. Noskov B. A., Mikhailovskaya, A. A., Lin, S.-Y., Loglio G., Miller R., Bovine Serum Albumin Unfolding at the Air/Water Interface as Studied by Dilational Surface Rheology, *Langmuir*, **2010**, 26, 17225–17231.
44. Luis G. Cascão Pereira, L. G., Olivier Théodoly, O., Blanch, H. W., Radke, C. J., *Langmuir*, **2003,** 19, 2349–2356.
45. Carter, D. C., He, X. M., Munson, S. H., Twigg, P. D., Gernert, K. M., Broom, M. B., Miller, T. Y. 3-Dimensional structure of humanserum albumin, *Science*, **1989**, 244, 1195−1198.
46. Noskov, B. A. Protein conformational transitions at the liquid − gas interface as studied by dilational surface rheology, *Adv. Colloid Interface Sci.*, **2014**, 206, 222 − 238.
47. Martin, A. H., Meinders, M. B. J., Bos, M. A., Cohen Stuart, M. A., van Vliet, T. Conformational aspects of proteins at the air/water interface studied by infrared reflection-absorption spectroscopy, *Langmuir*, **2003**, 19, 2922 − 2928.
48. Damodaran, S. Protein stabilization of emulsions and foams, *J. Food Sci*., **2005**, 70, R54 − R56.
49. Lad, M. D., Birembaut, F., Matthew, J. M., Frazier, R. A., Green, R. J. The adsorbed conformation of globular proteins at the air/water interface, *Phys. Chem. Chem. Phys*., **2006**, 8, 2179 − 2186.
50. Ang, J. C., Henderson, M. J., Campbell, R. A., Lin, J. M., Yaron, P. N., Nelson, A., Faunce, T., White, J. W. Human serum albumin binding to silica nanoparticles − effect of protein fatty acid ligand, *Phys. Chem. Chem. Phys*., **2014**, 16, 10157 − 10168.
51. Gorter, E., Grendel, F. On the spreading of proteins., *Trans. Faraday Soc.*, **1926**, 22, 477 − 483.
52. Hughes, E., Rideal, E. K. On protein monolayers. Proc. R. Soc. London, Ser. A 1932, 137, 62–77.
53. Dunér, G., Kim, M., Tilton, R. D., Garoff, S., Przybycien, T. M. Effect of polyelectrolyte–surfactant complexation on Marangoni transport at a liquid–liquid interface, *J. Colloid Interface Sci.*, **2016**, 467, 105–114.
54. Wilke, N., Lipid Monolayers at the Air–Water Interface: A Tool for Understanding Electrostatic Interactions and Rheology in Biomembranes, *Adv Planar Lipid Bilayers Liposomes*, **2014**, 20, 51–81.
55. Belička, M., Gerelli, Y., Kučerka, N., Fragneto, G., The component groups structure of DPPC bilayers obtained by specular neutron reflectometry, *Soft Matter*, **2015**, 11, 6275–6283.
56. Fragneto, G., Alexandre, S. Valleton, J-M., Rondelez, F., Competition for space between a protein and lipid monolayers, *Colloids Surf. B*, **2013**, 103, 416–421.

57. MacRitchie, F., Ter-Minassian-Saraga, L. Concentrated protein monolayers: Desorption studies with radiolabelled bovine serum albumin, *Colloids Surf*., **1984**, 10, 53−64.
58. Perriman, A. W., McGillivray, D. J., White, J. W. Reactions of isolated mono-molecular protein films, *Soft Matter*, **2008**, 4, 2192 − 2198.
59. Eaglesham, A., Herrington, T. M., Penfold, J. A neutron reflectivity study of a spread monolayer of bovine serum albumin, *Colloids Surf*., **1992**, 65, 9 − 16.
60. Rodríguez Niño, M. R., Rodríguez Patino J. M., Effect of the Aqueous Phase Composition on the Adsorption of Bovine Serum Albumin to the Air-Water Interface, *Ind. Eng. Chem. Res.* **2002,** 41, 1489–1495.
61. Fainerman, V. B., Miller, R. Proteins at Liquid Interfaces, Mobius, D, Miller, R, *Eds. Elsevier:* Amsterdam, **1998**, 51.
62. Hunter, R. J., Foundations of colloid science, second edition, *Oxford University Press*, **2001**.
63. Myers, D., Surfaces, interfaces and colloids, second edition, *John Wiley & Sons, Inc*, **1999**.
64. Berti, D., Palazzo G., Colloidal foundations of nanoscience, *Elsevier*, **2014**.
65. Tanford, C., Micelle shape and size, *J. Phys. Chem.*, **1972**, 76, 3020–3024.
66. Tanford, C. The Hydrophobic Effect, *Wiley-Interscience*: New York, **1973**.
67. Israelachivili, J. N., Mitchel, J., Ninham, B. W., *J. Chem. Soc., Faraday Trans. 2: Molecular and Chemical Physics*, **1976**, 72, 1525–1568.
68. Goddard, E. D., Polymer and surfactant interaction part I. Uncharged water soluble polymers and uncharged surfactant, *Colloids and Surf.*, **1986**, 19, 255–300.
69. Mészáros, R., Gilányi, T., Varga, I., Effect of Polymer Molecular Weight on the Polymer/Surfactant Interaction, *J. Phys. Chem. B*, **2005,** 109, 13538–13544.
70. Shirahama, K., Tsujii, K., Takagi, T., Free-boundary Electrophoresis of Sodium Dodecyl SulfateProtein Polypeptide Complexes with Special Reference to SDS-Polyacrylamide Gel Electrophoresis, *J. Biochem*, **1974**, 75, 309–319.
71. Gilányi, T., Mészáros, R., Varga, I., Determination of binding isotherms of ionic surfactants in polymer gels, *Prog. Colloid Polym Sci.*, **2001**, 117, 141–144.
72. Gilányi T.,On the counterion dissociation of colloid electrolytes, *J. Colloid Interface Sci.*, **1988**, 125, 641–648.
73. Naderi, A., Claesson, P. M., Bergstrom, M., Dedinaite, A. Trapped Non-equilibrium States in Aqueous Solutions of Oppositely-charged Polyelectrolyte and Surfactants: Effects of Mixing Protocol and Salt Concentration, *Colloids Surf. A*, **2005**, 253, 83–93.
74. Mezei, A., Pojják, K., Mészáros, R. Non-equilibrium Features of the Association between Poly(vinylamine) and Sodium Dodecyl Sulfate: The Validity of the Colloid Dispersion Concept, *J. Phys. Chem. B*, **2008**, 112, 9693–9699.
75. Goddard, E. D. Polymer—surfactant Interaction Part II. Polymer and Surfactant of Opposite Charge, *Colloids Surf.*, **1986**, 19, 301–329.
76. Kogej, K. Association and Structure Formation in Oppositely-charged Polyelectrolyte–surfactant Mixtures, *Adv. Colloid Interface Sci*., **2010**, 158, 68–83.
77. Hansson, P., Lindman, B. Surfactant-Polymer Interactions, *Curr. Opin. Colloid Interface Sci.*, **1996**, 1, 604–613.
78. Bergfeldt, K., Piculell, L., Linse, P. Segregation and Association in Mixed Polymer Solutions from Flory-Huggins Model Calculations, *J. Phys. Chem.*, **1996**, 100, 3680–3687.
79. Mészáros, R., Thompson, L., Bos, M., Varga, I., Gilányi, T. Interaction of Sodium Dodecyl Sulfate with Polyethyleneimine: Surfactant-Induced Polymer Solution Colloid Dispersion Transition, *Langmuir*, **2003**, 19, 609–615.

80. Ábrahám, A., Mezei, A., Mészáros, R. The effect of salt on the association between linear cationic polyelectrolytes and sodium dodecyl sulfate, *Soft Matter*, **2009**, 5, 3718–3726.
81. Pojják, K., Bertalanits, E., Mészáros, R. Effect of Salt on the Equilibrium and Non-equilibrium Features of Polyelectrolyte/Surfactant Association, *Langmuir*, **2011**, 27, 9139–9147.
82. Goddard, E. D., Phillips, T. S., Hannan, R. B., Water soluble polymer-surfactant interaction - part I., *J. Soc. Cosmet. Chem.*, **1975**, 26, 461−475.
83. Goddard, E. D., Hannan, R. B., Cationic polymer/anionic surfactant interactions., *J. Colloid Interface Sci*., **1976**, 55, 73−79.
84. Buckingham, J. H., Lucassen, J., Hollway, F., Surface properties of mixed solutions of poly-l-lysine and sodium dodecyl sulfate: I. equilibrium surface properties, *J. Colloid Interface Sci.*, **1978**, 67, 423−431.
85. Bergeron, V., Langevin, D., Asnacios, A. Thin-film forces in foam films containing anionic polyelectrolyte and charged surfactants, *Langmuir*, **1996**, 12, 1550−1556.
86. Stubenrauch, C., Albouy, P.-A., v. Klitzing, R., Langevin, D. Polymer/surfactant complexes at the water/air interface: a surface tension and x-ray reflectivity study, *Langmuir*, **2000**, 16, 3206−3213.
87. Ritacco, H., Albouy, P.-A., Bhattacharyya, A., Langevin, D. Influence of the polymer backbone rigidity on polyelectrolytesurfactant complexes at the air/water interface, *Phys. Chem. Chem. Phys*, **2000**, 2, 5243−5251.
88. Asnacios, A., Langevin, D., Argillier, J.-F. Complexation of Cationic Surfactant and Anionic Polymer at the Air- Water Interface, *Macromolecules*, **1996**, 29, 7412–7417.
89. Goddard, E. D. Polymer/Surfactant Interaction: Interfacial Aspects, *J. Colloid Interface Sci.*, **2002**, 256, 228–235.
90. Taylor, D. J. F., Thomas, R. K., Penfold, J. Polymer/Surfactant Interactions at the Air/Water Interface, *Adv. Colloid Interface Sci.*, **2007**, 132, 69–110.
91. Campbell, R. A., Angus-Smyth, A., Yanez Arteta, M., Tonigold, K., Nylander, T., Varga, I. A New Perspective on the Surface Tension Cliff Edge observed in Oppositely-charged Polyelectrolyte/ Surfactant Mixtures, *J. Phys. Chem. Lett.*, **2010**, 1, 3021–3026.
92. Campbell, R. A., Yanez Arteta, M., Angus-Smyth, A., Nylander, T., Noskov, B. A., Varga, I. Direct Impact of Non-equilibrium Aggregates on the Structure and Morphology of Pdadmac/SDS Layers at the Air/Water Interface, *Langmuir*, **2014**, 30, 8664–8674.
93. Varga, I., Campbell, R. A. General Physical Description of the Behavior of Oppositely-charged Polyelectrolyte/Surfactant Mixtures at the Air/Water Interface, *Langmuir*, **2017**, 33, 5915–5924.
94. Ábrahám, Á., Kardos, A., Mezei, A., Campbell, R. A., Varga, I. Effects of Ionic Strength on the Surface Tension and Non-equilibrium Interfacial Characteristics of Poly(sodium styrene sulfonate)/ Dodecyltrimethylammonium Bromide Mixtures, *Langmuir*, **2014**, 30, 4970–4979.
95. Schulze-Zachau, F., Braunschweig, B. Structure of Polystyrenesulfonate/Surfactant Mixtures at Air-Water Interfaces and Their Role as Building Blocks for Macroscopic Foam, *Langmuir*, **2017**, 33, 3499–3508.
96. Livia Simion, E., Stîngă, G., Iovescu, A., Băran, A., Anghel, D-F. Ageing of Fluorescent and Smart Naphthalene labeled Poly(acrylic acid)/Cationic Surfactant Complex, *Colloids Surf. A*, **2017**, 527, 81–88.
97. Taylor, D. J. F., Thomas, R. K., Penfold, J. The adsorption of oppositely-charged polyelectrolyte/surfactant mixtures: neutron reflection from dodecyl trimethylammonium bromide and sodium poly(styrene sulfonate) at the air/water interface, *Langmuir*, **2002**, 18, 4748−4757.

98. Taylor, D. J. F., Thomas, R. K., Hines, J. D., Humphreys, K., Penfold, J. The adsorption of oppositely-charged polyelectrolyte/ surfactant mixtures at the air/water interface: neutron reflection from dodecyl trimethylammonium bromide/sodium poly(styrene sulfonate) and sodium dodecyl sulfate/poly(vinyl pyridinium chloride), *Langmuir*, **2002**, 18, 9783−9791.
99. Staples, E., Tucker, I., Penfold, J., Warren, N., Thomas, R. K., Organization of polymer-surfactant mixtures at the air-water interface: poly(dimethyldiallylammonium chloride), sodium dodecyl sulfate, and hexaethylene glycol monododecyl ether, *Langmuir*, **2002**, 18, 5139−5146.
100. Staples, E., Tucker, I., Penfold, J., Warren, N., Thomas, R. K., Organization of polymer−surfactant mixtures at the air−water interface: sodium dodecyl sulfate and poly(dimethyldiallylammonium chloride), *Langmuir*, **2002**, 18, 5147−5153.
101. Ábraham, Á., Campbell, R. A., Varga, I., New Method to Predict the Surface Tension of Complex Synthetic and Biological Polyelectrolyte/Surfactant Mixtures, *Langmuir*, **2013**, 29, 11554 − 11559.
102. Campbell, R. A., Tummino, A., Noskov, B. A., Varga, I., Polyelectrolyte/Surfactant Films Spread from Neutral Aggregates, *Soft Matter*, **2016**, 12, 5304–5312.
103. Tummino, A., Toscano, J., Sebastiani, F., Noskov, B. A., Varga, I., Campbell, R. A., Effects of Aggregate Charge and Subphase Ionic Strength on the Properties of Spread Polyelectrolyte/Surfactant Films at the Air/Water Interface under Static and Dynamic Conditions, *Langmuir*, **2018**, 34, 2312−2323.
104. Braun, L., Uhlig, M., von Klitzing, R., Campbell R. A., Polymers and Surfactants at Fluid Interfaces Studied with Specular Neutron Reflectometry, *Adv. Colloid Interface Sci.*, 2017, 247, 130–148.
105. Jain, N. J., Albouy, P.-A., Langevin, D. Study of Adsorbed Monolayers of a Cationic Surfactant and an Anionic Polyelectrolyte at the Air–Water Interface, *Langmuir*, **2003**, 19, 5680–5690.
106. Monteux, C., Williams, C. E., Meunier, J., Anthony, O., Bergeron, V. Adsorption of Oppositely-charged Polyelectrolyte/Surfactant Complexes at the Air/Water Interface: Formation of Interfacial Gels, *Langmuir*, **2004**, 20, 57–64.
107. Noskov, B. A., Loglio, G., Miller, R. Dilational Viscoelasticity of Polyelectolyte/Surfactant Adsorption Films at the Air/Water Interface: Dodecyltrimethylammonium Bromide and Sodium Poly(styrenesulfonate), *J. Phys. Chem. B*, **2004**, 108, 18615–18622.
108. Lee, Y.-L., Dudek, A., Ke, T.-N., Hsiao, F.-W., Chang, C.-H., Mixed Polyelectrolyte−Surfactant Langmuir Monolayers at the Air/Water Interface, *Macromolecules*, **2008**, 41, 5845–5853.
109. Gao, Y., Duc, L. T., Ali, A., Liang, B., Liang, J.-T., Dhar, P. Interface-Induced Disassembly of a Self-Assembled Two-Component Nanoparticle System, *Langmuir*, **2013**, 29, 3654–3661.
110. Angus-Smyth, A., Bain, C. D., Varga, I., Campbell, R. A. Effects of Bulk Aggregation on PEI–SDS Monolayers at the Dynamic Air–liquid Interface: Depletion Due to Precipitation versus Enrichment by a Convection/Spreading Mechanism, *Soft Matter*, **2013**, 9, 6103–6617.
111. Yanez Arteta, M., Campbell, R. A., Watkins, E. B., Obiols-Rabasa, M., Schillén, K., Nylander, T. Interactions of Small Dendrimers with Sodium Dodecyl Sulfate at the Air–Water Interface, *J. Phys. Chem. B*, **2014**, 118, 11835–11848.
112. Tong, L. J., Bao, M. T., Li, Y. M., Gong, H.Y. Interfacial Dynamic and Dilational Rheology of Polyelectrolyte/Surfactant Two-component Nanoparticle Systems at Air–Water Interface, *Appl. Surf. Sci,*. **2014**, 316, 147–154.

113. Tonigold, K., Varga, I., Nylander, T., Campbell, R. A. Effects of aggregates on mixed adsorption layers of poly(ethylene imine) and sodium dodecyl sulfate at the air/liquid interface, *Langmuir*, **2009**, 25, 4036 − 4046.
114. Ip, S. W., Toguri, J. M., The equivalency of surface tension, surface energy and surface free energy, *J. Mater. Sci.*, **1994**, 29, 688–692.
115. Dorsey, E., *Scientific Papers of the Bureau of Standards*, **1926**, 21, S540–S595.
116. Harkins, W. D., Jorda, H. F., A method for the determination of surface and interfacial tension from the maximum pull of a ring, *J. Am. Chem. Soc*., **1930**, 52, 1751–1772.
117. Barik, T. K., Roy Chaudhuri, R., Roy, A. Kar S., Probing liquid surface waves, liquid properties and liquid films with light diffraction, *Am. J. Phys.*, **2005**, 73, 725–729.
118. Nikolić, D., Nešić, L., Determination of surface tension coefficient of liquids by diffraction of light on capillary waves, *Eur. J. Phys.*, **2012**, 33**,** 1677–1685.
119. Lunkenheimer., K,. Winsel, K., Fruhner., H, Fang, J., Wantke, K. D., Siegler, K., Dynamic surface tension and surface area elasticity of adsorbed pulmonary surfactant layers, *Colloids Surf.A: Physicochem. Eng. Aspects*, **1996**, 114, 199–210.
120. Noskov, B. A., Dilational surface rheology of polymer and polymer/surfactant solutions, *Curr. Opin. Colloid Interface Sci.*, **2010**, 15, 229–236.
121. De Feijter, J. A., Benjamins, J. and Veer, F. A., Ellipsometry as a tool to study the adsorption behavior of synthetic and biopolymers at the air–water interface, *Biopolymers*, **1978**, 17, 1759–1772.
122.Lu, J. R, Thomas, R. K., Penfold, J., Surfactant layers at the air/water interface: structure and composition, *Adv. Colloid Interface Sci.*, **2000**, 84, 2000, 143–304.
123. Battal, T., Shearman, G. C., Valkovska, D., Bain, C. D., Darton, R. C., Eastoe, J., Determination of the Dynamic Surface Excess of a Homologous Series of Cationic Surfactants by Ellipsometry, *Langmuir*, **2003,** 19, 1244–1248.
124. Péron, N., Campbell, R. A., Nylander, T., Vareikis, A., Makuska, R., Gilányi, T., Mészáros, R., Competitive Adsorption of Neutral Comb Polymers and Sodium Dodecyl Sulfate at the Air/Water Interface, *J. Phys. Chem. B*, **2008,** 112, 7410–7419.
125. Fauser, H., von Klitzing, R., Campbell R. A., Surface Adsorption of Oppositely-charged C_{14}TAB-PAMPS Mixtures at the Air/Water Interface and the Impact on Foam Film Stability, *J. Phys. Chem. B*, **2015**, 119, 348−358.
126. Campbell, R. A., Edler, K. J., Growth-collapse mechanism of PEI-CTAB films at the air–water interface, *Soft Matter*, **2011**, 7, 11125–11132.
127. Campbell, R. A., Ang, J. C., Sebastiani, F., Tummino, A., White, J. W., Spread Films of Human Serum Albumin at the Air–Water Interface: Optimization, Morphology, and Durability, *Langmuir*, **2015**, 31, 13535–13542.
128. Tyrode, E., Johnson, C. M., Rutland, M. W., Day, J. P. R., Bain, C. D. A Study of the Adsorption of Ammonium Perfluorononanoate at the Air−Liquid Interface by Vibrational Sum-Frequency Spectroscopy, *J. Phys. Chem. C*, **2007**, 111, 316–329.
129. Li, P. X., Thomas, R. K., Penfold, J. Limitations in the Use of Surface Tension and the Gibbs Equation To Determine Surface Excesses of Cationic Surfactants, *Langmuir*, **2014**, 30, 6739–6747.
130. Cubitt, R. Fragneto, G., Scattering, chapter 2.8.3 - Neutron reflection: principles and examples of applications, **2002**, 1198–1208, *Academic Press London*.
131. Demkowicz, M. J., Majewski, J., Probing Interfaces in Metals Using Neutron Reflectometry, *Metals*, **2016**, 6, 20–36.
132. Wood, M. H., Welbourn, R. J. L., Zarbakhsh, A., Gutfreund, P., Clarke, S. M. Polarized Neutron Reflectometry of Nickel Corrosion Inhibitors, *Langmuir*, **2015**, 31, 7062−7072.
133. Glover, S. E., Saerbeck, T., Kuerbanjiang, B., Ghasemi, A., Kepaptsoglou, D., Ramasse, Q. M., Yamada, S., Hamaya, K., Hase, T. P. A., Lazarov, V. K., Bell, G. R., Magnetic and

structural depth profiles of Heusler alloy $Co_2FeAl_{0.5}Si_{0.5}$ epitaxial films on Si(111), *J. Phys.: Condens. Matter*, **2018**, 30, 1–7.
134. Sebastiani, F., Campbell, R. A., Rastogi, K., Pfrang, C., Nighttime oxidation of surfactants at the air–water interface: effects of chain length, head group and saturation, *Atmos. Chem. Phys*., **2018**, 18, 3249–3268.
135. Nelson, A., Co-refinement of multiple-contrast neutron/X-ray reflectivity data using MOTOFIT, *J. Appl. Cryst.*, **2006**, 39, 273–276.
136. Gerelli, Y., Aurore: new software for neutron reflectivity data analysis, *J. Appl. Cryst.*, **2016,** 49, 330–339.
137. Campbell, R. A., Wacklin, H. P., Sutton, I., Cubitt, R., Fragneto, G., FIGARO: The new horizontal neutron reflectometer at the ILL, *Eur. Phys. J. Plus*, **2011**, 126, 107.
138. Pfrang, C., Sebastiani, F., Lucas, C. O. M., King, M. D., Hoare, I. D., Chang, D., Campbell, R. A.: Ozonolysis of methyl oleate monolayers at the air–water interface: oxidation kinetics, reaction products and atmospheric implications, *Phys. Chem. Chem. Phys.*, **2014**, 16, 13220–13228.
139. Ciumac, D., Campbell, R. A., Xu, H., Clifton, L. A., Hughes, A. V., Webster, J. R. P., Lu, J., Implications of Lipid Monolayer Charge Characteristics on their Selective Interactions with a Short Antimicrobial Peptide, *Colloids Surf. B*, **2017**, 150, 308–316.
140. Ciumac, D., Campbell, R. A., Clifton, L. A., Xu, H., Fragneto, G., Lu, J. R., Influence of Acyl Chain Saturation on the Membrane Binding Activity of a Short Antimicrobial Peptide, *ACS Omega*, **2017**, 2, 7482–7492.
141. Niga, P., Hansson-Mille, P. M., Swerin, A. Claesson, P. M., Schoelkopf, J., Gane, P. A. C., Bergendal, E., Tummino, A., Campbell, R. A., Johnson, C. M., Interactions between Model Cell Membranes and the Neuroactive Drug Propofol, *J. Colloid Interface Sci.*, **2018**, 526, 230–243.
142. Hansen, F. K., Myrvold, R., The Kinetics of Albumin Adsorption to the Air/Water Interface Measured by Automatic Axisymmetric Drop Shape Analysis, *J. Colloid Interface Sci*., **1995**, 176, 408–417.
143. Erickson, J. S., Sundaram ,S., Stebe, K. J., Evidence that the induction time in the surface pressure evolution of lysozyme solutions is caused by a surface phase transition, *Langmuir*, **2000**, 16, 5072–5078.
144. Campbell, R. A., Tummino, A., Varga, I., Milyaeva, O. Y., Krycki, M. M., Lin, S.-Y., Laux, V., Haertlein, M., Forsyth, V. T., Noskov, B. A., Adsorption of Denaturated Lysozyme at the Air–Water Interface: Structure and Morphology, *Langmuir*, **2018**, 34, 5020–5029.
145.Campbell, R. A., Yanez Arteta, M., Angus-Smyth, A., Nylander, T., Varga, I., Multilayers at Interfaces of an Oppositely-charged Polyelectrolyte/Surfactant System Resulting from the Transport of Bulk Aggregates under Gravity, *J. Phys. Chem. B*, **2012**, 116, 7981 − 7990.
146. Trabelsi, S., Langevin, D., Co-adsorption of Carboxymethyl-Cellulose and Cationic Surfactants at the Air–Water Interface, *Langmuir*, **2007**, 23, 1248–1252.
147. Yazhgur, P. A., Noskov, B. A., Liggieri, L., Lin, S.-Y., Loglio, G., Miller, R., Ravera, F., Dynamic Properties of Mixed Nanoparticle/Surfactant Adsorption Layers, *Soft Matter*, **2013**, 9, 3305–3314.
148. Buzin, A. I., Godovsky, Y. K., Makarova, N. N., Fang, J., Wang, X., Knobler, C. M., Stepwise Collapse of Monolayers of Cyclolinear Poly(organosiloxane)s at the Air/Water Interface: A Brewster-Angle Microscopy and Scanning Force Microscopy Study, *J. Phys. Chem. B*, **1999**, 103, 11372–11381.
149. Campbell, R. A., Yanez Arteta, M., Angus-Smyth,A., Nylander, T., Varga I., Effects of Bulk Colloidal Stability on Adsorption Layers of Poly(diallyldimethylammonium Chloride)/Sodium Dodecyl Sulfate at the AirWater Interface Studied by Neutron Reflectometry, *J. Phys. Chem. B*, **2011**, 115, 15202–15213.

150. Penfold, J., Tucker, I., Thomas, R. K, Zhang, J., Adsorption of Polyelectrolyte/ Surfactant Mixtures at the Air-Solution Interface: Poly(ethyleneimine)/Sodium Dodecyl Sulfate, *Langmuir*, **2005**, 21, 10061–10073.
151. Penfold, J., Tucker, I., Thomas, R. K, Taylor, D. J. F., Zhang, J., Zhang, X. L., The Impact of Electrolyte on the Adsorption of Sodium Dodecyl Sulfate/Polyethyleneimine Complexes at the Air-Solution Interface, *Langmuir*, **2007**, 23, 3690–3698.
152. Morán, M. C., Mitjans, M., Martínez, V., Nogueira, D. R., Pilar Vinardell, M., Current directions in DNA gel particles, in *Recent Advances in Pharmaceutical Sciences III*, **2013,** 145–162.
153. Naahidi, S., Jafari, M., Logan, M., Wang, Y., Yuan, Y., Bae, H., Dixon, B., Chen, P., Biocompatibility of hydrogel-based scaffolds for tissue engineering applications, *Biotech. Adv.*, **2017**, 35, 530–544.
154. Norberto Oliveira, A. C., Passos Sárria, M., Moreira, P., Fernandes, J., Castro, L., Lopes, I., Côrte-Real, M., Cavaco-Paulo, A., Cunha Dias Real Oliveir, M. E., Castro Gomes, A., Counter ions and constituents combination affect DODAX : MO nanocarriers toxicity in vitro and in vivo, *Toxicol. Res*., **2016**, 5, 1244–1255.
155. Chen, F., Ehlerding, E. B., Cai, W., Theranostic Nanoparticles, *J Nucl Med*., **2014**, 55, 1919–1922.
156. Shunxi, J., Walz J. Y., Depletion forces and flocculation with surfactants, polymers and particles — particles — Synergistic effects, *Curr. Opin. Colloid Interface Sci.*, **2015**, 20, 39–45.
157. Jones, M. N., The Interaction of Sodium Dodecyl Sulfate with Polyethylene Oxide, *J. Colloid Interface Sci.*, **1967**, 23, 36–42.
158. Dahoo, P. R., Khettab, M., Linares, J., Pougnet, P., 2: Non-Destructive Characterization by Spectroscopic Ellipsometry of Interfaces in Mechatronic Devices, in *Embedded Mechatronic Systems 1*, **2015**, 27–56.
159. Schurch, S., Goerke, J., Clements, J. A., Direct determination of surface tension in the lung, *Proc. Nati. Acad. Sci. USA*, **1976**, 73, 4698–4702.
160. Hallman, M., Lung surfactant in respiratory distress syndrome, *Acta Anaesthesiol Scand Suppl.*, **1991**, 95, 15–20.